Investigation of the effect of Zn impurities and magnetic field on the spin dynamics in underdoped $YBa_2(Cu_{1-y}Zn_y)_3O_x$

Anton Suchaneck

Max-Planck-Institut für Festkörperforschung
Stuttgart 2009

Investigation of the effect of Zn impurities and magnetic field on the spin dynamics in underdoped $YBa_2(Cu_{1-y}Zn_y)_3O_x$

Von der Fakultät Mathematik und Physik der Universität Stuttgart
zur Erlangung der Würde eines Doktors der Naturwissenschaften (Dr. rer. nat.)
genehmigte Abhandlung

vorgelegt von

Anton Suchaneck
aus Leningrad (Russland)

Hauptberichter: Prof. Dr. Bernhard Keimer
Mitberichter: Prof. Dr. Martin Dressel
Tag der mündlichen Prüfung: 20. April 2009

Max-Planck-Institut für Festkörperforschung
Stuttgart 2009

Contents

Zusammenfassung

Eine der wichtigen großen offenen Fragen der Festkörperforschung ist die physikalische Ursache der Hochtemperatursupraleitung. Viele Materialien werden unterhalb einer supraleitenden kritischen Temperatur supraleitend, jedoch nur in Hochtemperatursupraleitern erreicht diese Temperatur bis zu 130 K. Auf der theoretischen Seite kann in den konventionellen Supraleitern die quantenmechanische Bardeen-Cooper-Schrieffer Wellenfunktion viele experimentelle Beobachtungen voraussagen. Grundlegende Eigenschaften wie zum Beispiel Elektronenpaarung hat man auch in Hochtemperatursupraleitern nachgewiesen, jedoch konnte trotz vieler Jahre der theoretischen Forschung noch keine allumfassende Theorie gefunden werden. Deshalb können weitere experimentelle Entdeckungen Aufschluss geben welche theoretischen Ansätze zur Beschreibung der Phänomene am aussichtsreichsten sein könnten.

Die Materialien, welche in dieser Arbeit untersucht wurden, gehören zur Klasse der Kuprate zu denen beispielsweise $YBa_2Cu_3O_x$ und $La_{2-x}Sr_xCuO_4$ zählen. Sie haben einen geschichteten Aufbau mit zweidimensionalen Kupferoxidebenen in denen sich die Supraleitung ausbildet, sobald die Ebenen mit Ladungsträgern dotiert werden. Undotiert sind die Materialien antiferromagnetische Mottisolatoren, sobald man sie jedoch mit Elektronen oder Lochladungsträgern dotiert, verschwindet der Antiferromagnetismus und Supraleitung bildet sich aus. Die jeweiligen kritischen Ladungskonzentrationen scheinen in allen Kupraten quantitativ universell zu sein. Im Dotierungsübergangsbereich zwischen Antiferromagnetismus und Supraleitung findet man bei tiefen Temperaturen die Spinglasphase, welche in $La_{2-x}Sr_xCuO_4$ ausgeprägt, aber wohingegen in $YBa_2Cu_3O_x$ sie nur schwer nachzuweisen ist.

Der Gegenstand dieser Doktorarbeit ist der lochdotierte Kupratsupraleiter $YBa_2Cu_3O_x$, welcher bei $x = 6.93$ seine maximale Übergangstemperatur von 93 K erreicht. Dieser Supraleiter hat pro Kristalleinheitszelle zwei nah beieinander liegende Kupferoxidebenen, welche durch eine starke Austauschwechselwirkung gekoppelt sind. Folglich weisen physikalische Effekte die durch Neutronenstreuung in diesen Ebenen gemessen werden in der Richtung senkrecht zu den Ebenen die sogenannte Bilayermodulation auf.

Die Lochdotierung in $YBa_2Cu_3O_x$ kann durch Annealing in einer genau eingestellten Sauerstoffatmosphäre erfolgen, was zur Folge hat, dass sich Sauerstoffionen zusätzlich kettenförmig eingebauten. Die Ausrichtung der Ketten führt zu einer orthorhombischen Verzerrung der Kristalleinheitszelle, falls der Sauerstoffgehalt $x < 6.35$ ist.

Orthorhombische Kristalle können im Allgemeinen während des Wachstums Zwillingsdomänen ausbilden, was bedeutet dass die unterschiedlich langen *a* und *b* Achsen von Domäne zu Domäne vertauscht sind. Da Neutronenstreuung das Material als Ganzes untersucht, führt die genannte Verzwillingung dazu, dass eine Unterscheidung der beiden Achsen experimentell nicht möglich ist. Um trotzdem eine Unterscheidung zu ermöglichen wurden die Kristalle für diese Doktorarbeit entzwillingt. Dies kann durch uniachsialen Druck bei hohen Temperaturen erfolgen, wodurch die Zwillingsdomänen sich auszurichten beginnen.

Das quasi-zweidimensionale Elektronensystem der Kupratsupraleiter wird wesentlich durch die Coulombkorrelationen zwischen den Elektronen bestimmt, was sich wiederrum in der Energie- und Impulsabhängigkeit der Spinsuszeptibilität widerspiegelt. In dieser Doktorarbeit wird die Spinsuszeptibilität mit elastischen und inelastischen Neutronstreuexperimentem an entzwillingten $YBa_2Cu_3O_x$ Einkristallen mit einer gewählten Zinkdotierung gemessen.

Die Hauptmerkmale des Spinanregungsspektrums von reinem $YBa_2Cu_3O_x$ wurden in Neutronenstreuexperimenten der letzten 20 Jahre dokumentiert und für alle Sauerstoffdotierungen *x* wurden magnetische Anregungen bei oder nah dem antiferromagnetischen Wellenvektor gefunden. Im supraleitenden Zustand sind diese Anregungen bei einer dotierungsabhängigen Resonanzenergie am stärksten. Bei dieser Energie erfährt die Streuintensität eine starke Abschwächung sobald durch Erhöhung der Temperatur der supraleitende Zustand verlassen wird. Unterhalb und überhalb diese Resonanzenergie spaltet sich das Anregungsspektrum zu zwei Maxima in der Impulsabhängigkeit, so dass sich eine sogenannte Sanduhrdispersion im Energie-Impuls-Graphen abzeichnet. Unterhalb einer Grenzenergie, welche Spinlücke genannt wird, ist die Intensität des Spektrum stark reduziert.

Um zusätzliche Informationen über die Physik der Kuprate zu bekommen, kann man Experimente mit kontrollierten Modifikationen an den Proben durchführen. In dieser Arbeit werden sowohl Zinkfremdatome als auch der Einfluss eines angelegten Magnetfeldes betrachtet.

Schon ein verhältnismäßig geringer Anteil von Zinkfremdatome kann die supraleitenden Eigenschaften und das magnetische Anregungsspektrum drastisch verändern. Der gravierendste Einfluss, welcher im Gegensatz zum Verhalten in gewöhnlichen Supraleitern steht, ist die starke Unterdrückung der supraleitenden Übergangstemperatur durch diese nichtmagnetischen Einschlüsse. Zusätzlich zur Unterdrückung der Supraleitung wird die Spinglasphase über einen größeren Dotierungsbereich ausgedehnt. Weiterhin haben NMR Messungen festgestellt, dass sich ein lokaler alternierender magnetischer Moment am Fremdatom und dessen Nachbarn ausbildet. Erste Hinweise darauf, dass sich auch das tiefenergetische magnetische Anregungspektrum in Kupraten verändert kamen von Neutronenstreumessungen an $La_{2-x}Sr_xCu_{1-y}Zn_yO_4$ verschiedener Dotierungen. Es stellte sich heraus, dass Zinkfremdatome quasi-elastische inkommensurate Anregungen induzieren ähnlich dem statischen Signal in $La_{2-x-y}Nd_ySr_xCuO_4$, wo dieser Effekt durch eindimensionale ("Streifen") Ordnung der Spins und der Ladungen erklärt wird. Äquivalente Messungen in $YBa_2(Cu_{1-y}Zn_y)_3O_x$ zeigten jedoch vorerst

nur ein breites kommensurates Signal bei tiefen Energien. Das Anregungsspektrum der zinkfreien Verbindung ist zusätzlich durch die Resonanzmode geprägt, welche durch die Zinkfremdatome mit deren steigender Anzahl zunehmend unterdrückt wird. Es ist aber zu beachten, dass all diese Messungen an $YBa_2(Cu_{1-y}Zn_y)_3O_x$ an verzwillingten Kristallen durchgeführt wurden, so dass eventuelle Anisotropien in den Kupferoxidebenen nicht aufgelöst werden konnten und die genaue Dispersion unklar blieb.

In dieser Doktorarbeit werden die Effekte von Zinkfremdatomen in $YBa_2(Cu_{1-y}Zn_y)_3O_x$ auf die Tiefenergieanregungen und die Resonanzmode umfassend untersucht. Zusätzlich wird Information über den Verlauf Anregungsdispersion und deren *ab*-Ebenenanisotropie gewonnen.

Die erste untersuchte Verbindung ist $YBa_2(Cu_{0.98}Zn_{0.02})_3O_{6.6}$ (T_c = 30K). Dieselbe Verbindung ohne der Zinkfremdatome wurde schon in einer vorhergehenden Arbeit untersucht und eine Resonanzmode bei 38 meV und eine Spinlücke unterhalb 20 meV wurde gefunden. Mittels einer geeigneten Kalibrierungmethode, welche auf dem Vergleich äquivalenter Neutronenmessungen in beiden Proben beruht, können quantitative Aussagen zwischen der zinkdotierten und der zinkfreien Probe gemacht werden. Es zeigt sich, dass die Hochenergieanregungen qualitativ wenig durch die Zinkfremdatome beeinflusst werden, jedoch wird aus der charakterischen Temperaturabhängigkeit der Resonanzmode eine kontinuierlicherer Temperaturübergang. Die Dispersion im supraleitenden Zustand in der zinkdotierten Probe ähnelt der Dispersion der zinkfreien Probe im Normalzustand. Zusätzlich weist jedoch die zinkdotierte Probe inkommensurate Anregungen bei tiefen Energien unterhalb der Spinlücke der zinkfreien Probe auf. Diese Anregungen sind eindimensional, was bedeutet dass sie eine inkommensurate Struktur entlang der a^* Achse besitzen. Die Inkommensurabilität ändert sich mit der Energie kaum und auch eine Temperaturerhöhung über die supraleitende Übergangtemperatur verändert die Anregungen nur unwesentlich.

Diese Tiefenergieanregungen deuten auf die Existenz eines langsam fluktuierenden Zustands hin, der mit der Supraleitung konkurriert. Eine mögliche Erklärung ergibt sich durch die Streifenpinning Idee, derzufolge fluktuierende Spin-Ladungs-Streifen durch die Fremdatome verankert werden, sich damit verlangsamen und zu tiefenergetischen Anregungen werden. Die Neutronenstreumessungen untersuchen nur die Spineigenschaften, jedoch wurden mit STM Messungen auch Anzeichen für Ladungsordnung von Quasiteilchen in $Bi_{2-y}Pb_ySr_2Cu_2O_x$ und $Bi_2Sr_2Ca(Cu_{1-y}Zn_y)_2O_x$ gefunden. Dort fand man eine räumliche Ausdehnung einer Elektronenstrukturveränderung von etwa fünf Kristallgittereinheiten, was mit Schätzungen der Korrelationslänge aus Neutronenstreuexperimenten übereinstimmt. Sowohl STM als auch die Neutronstreumessungen belegen die Eindimensionalität der durch die Fremdatome induzierten Strukturen. Somit haben also verschiedene Messtechniken eine zinkinduzierte statische oder langsam fluktuierende Spin-Ladungs-Struktur nachgewiesen und Theorien welche diese Effekte auf das Tiefenergiespektrum erklären wurden aufgestellt.

Die zweite in dieser Arbeit untersuchte Verbindung ist $YBa_2(Cu_{0.98}Zn_{0.02})_3O_{6.45}$ ($T_c \sim 0$K). In der zinkfreien Verbindung mit gleicher Sauerstoffdotierung gibt es keine klaren Anzeichen einer Resonanzmode, so dass hier das Hochenergiespektrum nicht

untersucht wurde. Die zinkfreie Verbindung $YBa_2Cu_3O_{6.45}$ weist selbst schon Tiefenergieanregungen auf (Spinlücke $< 2\,\mathrm{meV}$), und es konnte keine durch Zink zusätzliche Intensität nachgewiesen werden. Jedoch zeigte sich durch die Zinkdotierung ein zwischenebenen-korreliertes quasi-elastischen Signal auf, dass ähnlich dem in $YBa_2Cu_3O_{6.35}$ (ähnliches T_c) ist. Die gefunden Tiefenergieanregungen sind innerhalb der Ebenen anisotrop mit einer schärferen Breite entlang b^*. Die Intensität nimmt mit steigender Temperatur stark ab.

Dass $YBa_2(Cu_{0.98}Zn_{0.02})_3O_{6.45}$ ($T_c = 0\mathrm{K}$) und $YBa_2Cu_3O_{6.35}$ ($T_c = 10\mathrm{K}$) nicht nur ein gleiches T_c, sondern auch ein ähnliches magnetisches Anregungspektrum haben ist nicht verwunderlich, da schon Magnetisierungsmessungen zeigte, dass die magnetischen Eigenschaften in $YBa_2(Cu_{1-y}Zn_y)_3O_x$ mit gleichem T_c identisch sind, unabhängig von der speziellen Sauerstoffdotierung. Das erklärt sich aus der Beobachtung, dass T_c zu der Superfluiddichte n_s proportional ist und damit eigentlich n_s der bestimmende Faktor ist. Ein einfache Erklärung für die Zwischenebenenkorrelation ist, dass der Störeffekt der Fremdatome die Supraleitung zerstört und die kurzreichweitige antiferromagnetische Ordnung, die in weit unterdotierten Proben zu finden ist, wieder hervorbringt.

Außer den zinkinduzierten Veränderungen am Anregungsspektrum wurde auch der Einfluss eines an $YBa_2Cu_3O_x$ angelegten Magnetfeldes untersucht. Da Kuprate Typ-II Supraleiter sind, wird ein Magnetfeld senkrecht zu den Kupferoxidebenen Vortexe zur Folge haben. Die supraleitende Übergangtemperatur wird reduziert und die Resonanzmode mitsamt der Anregungen nahe bei der Resonanzenergie werden durch das Magnetfeld unterdrückt. Ähnlich zu den zinkinduzierten Quasiteilchenzuständen fanden auch hier STM Messungen einen tiefenergetischen (~ 7 meV) elektronischen Zustand innerhalb der Vortexkerne, welcher nicht in konventionellen Supraleitern auftaucht. Weiterhin wurde eine schachbrettartige Modulierung mit Periodizität von vier Kristallgittereinheiten in und um die Vortexkerne gefunden.

Ergänzend zu den ortsaufgelösten Messungen konnten auch Neutronenstreumessungen magnetfeldverursachte Veränderungen an der magnetischen Ordnung und dem magnetischen Anregungsspektrum feststellen. Im sauerstoffdotierten $La_2CuO_{4+\delta}$ wurde gezeigt, dass ein Magnetfeld die statische Streifenordnung verstärkt und die supraleitende Übergangtemperatur unterdrückt, was den Anschein erweckt, dass beide Phase im Wettbewerb stehen. Für diese Verbindung wies μSR nach, dass beide Phasen räumlich koexistieren. Neutronenmessungen an unterdotiertem $La_{2-x}Sr_xCuO_4$ zeigten, dass ein Magnetfeld ein statischen inkommensurates Signal induziert und dessen Zwischenebenenkorrelationen verstärkt. Eine wesentliche Beobachtung ist, dass diese Induzierung nicht vorhanden ist, falls die statische Ordnung schon durch andere Einflüsse im feldfreien Zustand vorhanden ist, was zum Beispiel bei der Dotierung $p \sim 1/8$ geschieht. Weiter Magnetfeldeffekte bei tiefen Energien sind induzierte Anregungen innerhalb der Spinlücke in $La_{2-x}Sr_xCuO_4$ und die Spinlückenschließung in unterdotiertem $La_{2-x}Sr_xCuO_4$.

In dieser Doktorarbeit wurden Neutronenstreumessungen an stark unterdotiertem $YBa_2Cu_3O_{6.45}$ durchgeführt. Die schon ohne Magnetfeld gefundene statische Ord-

nung wird durch ein angelegtes Magnetfeld nochmals verstärkt. im Gegensatz dazu werden inelastische Anregungen unterdrückt, was um 4 meV am stärksten ersichtlich ist. Die Verstärkung des statischen Signal ist wahrscheinlich mit dem gleichen Effekt in $La_{2-x}Sr_xCuO_4$ gleichzusetzen. Dieser Effekt kann auch zur Erklärung der kürzlich gefunden Quantenoszillationen herangezogen werden. Die dort gefundenen kleinen Elektronen- und Lochtaschen können durch statische Überstrukturen und die damit verbundenen Rekonstruktion der Fermifläche erklärt werden. Die Unterdrückung der inelastischen Anregungen kann mit der Unterdrückung der Resonanz in $YBa_2Cu_3O_{6.6}$ verglichen werden. Obwohl vorher keine konkreten Anzeichen einer Resonanzmode in $YBa_2Cu_3O_{6.45}$ bestanden, könnten hiermit Überbleibsel der Resonanz bei tiefen Energien geschlussfolgert werden, welche genauso durch ein Magnetfeld unterdrückt werden.

Zusammenfassend kann man sagen, dass die Effekte von Zinkfrematomen und einem angelegten Magnetfeld viele Gemeinsamkeiten in ihrer Wirkung auf unterdotiertes $YBa_2Cu_3O_x$ aufweisen. Die supraleitenden Übergangstemperatur wird unterdrückt, Quasiteilchenzustände nahe den Zinkfremdatomen beziehungsweise den Vortexkernen werden induziert, ein elektronische Modulation um die Störstelle entsteht, die Resonanzmode wird unterdrückt, eindimensionale Tiefenergieanregungen innerhalb der Spinlücke treten auf, und eine statische Ordnung mit Zwischenebenenkorrelationen wird verstärkt oder gar induziert.

Die ähnliche Wirkungsweise von Zinkfremdatomen und dem Magnetfeld lässt schlussfolgern, dass der grundlegende Effekt in der Schwächung der Supraleitung und der Induktion einer uniachsialen inkommensuraten magnetischen Ordnung, welche mit der Supraleitung konkurriert, besteht. Die neugewonnen Daten in dieser Arbeit können zur weiteren Entwicklung der mikroskopischen Theorie der Interaktion der zwei Ordnungsphänomene, und deren Wirkung auf die makroskopischen Eigenschaften, beitragen.

Summary

The origin of high temperature superconductivity is one of the major unsolved problems in condensed matter physics. Many materials become superconducting below a superconducting critical temperature, but only in high temperature superconductors these temperature reach as high as 130 K. In conventional superconductors, the Bardeen-Cooper-Schrieffer paired wave function turned out to be capable of explaining many of the experimental results. Basic properties like electron pairing could likewise be detected in high temperature superconductors, however, despite many years of intense theoretical effort, no completely successful theory could be established. Therefore new experimental discoveries are needed in order to provide further clues where theoretical investigations should be heading.

The materials examined in this work belong to the class of cuprate superconductors, which exhibit a layered structure. The common structural motif of cuprate superconductors like $YBa_2Cu_3O_x$ and $La_{2-x}Sr_xCuO_4$ are stacked two-dimensional CuO_2-planes in which superconductivity is thought to develop when they are doped with charge carriers. If charge doping is absent, the parent compounds are known to be antiferromagnetic Mott insulators. With either hole doping or electron doping, the antiferromagnetic state is destroyed and superconductivity emerges in a well-defined doping range universal to all cuprates. At the cross-over from antiferromagnetism to superconductivity, a spin-glass phase is seen at low temperatures, which is more pronounced in $La_{2-x}Sr_xCuO_4$ and rather difficult to detect in $YBa_2Cu_3O_x$. The hole-doped cuprate superconductor $YBa_2Cu_3O_x$ with a maximum superconducting critical temperature of 93 K at $x = 6.93$ is the subject of this thesis. It has two closely spaced CuO_2-planes per unit cell. As a result, the planes are magnetically coupled by a strong superexchange interaction, which manifests itself in a bilayer modulation of the magnetic neutron scattering intensity in the direction perpendicular to the planes over the entire doping range investigated.

The hole-doping of $YBa_2Cu_3O_x$ can be adjusted by heat annealing in an oxygen atmosphere. The additional oxygen ions are accommodated in interstitial sites and form chain structures, which induce an orthorhombic distortion of the crystal structure for $x > 6.35$. Unfortunately, bulk crystals with orthorhombic lattice symmetry are known to form twin domains, in which the *a* and *b* axes in the copper oxide layers are interchanged. As neutron scattering is a bulk measurement, twinning impedes the investigation of the effect of the orthorhombic distortion on the electronic state of

$YBa_2Cu_3O_x$. To discriminate between both directions in the copper planes, the method of detwinning has been applied to the crystals examined in this thesis. This involves subjecting the crystals to uniaxial pressure at elevated temperatures in order to flip twin domain into one orientation only.

The quasi-two-dimensional electron system in the cuprate superconductors is strongly affected by Coulomb correlations between electrons. These correlations manifest themselves directly in the energy- and momentum-dependent spin susceptibility. In this thesis, elastic and inelastic magnetic neutron scattering were employed to probe this quantity in several arrays of untwinned $YBa_2Cu_3O_x$ single crystals with and without a controlled density of Zn impurities.

The main features of the spin excitation spectrum of pure (impurity-free) $YBa_2Cu_3O_x$ have been mapped out with neutron scattering in research efforts over the last 20 years. Magnetic excitations at or close to the antiferromagnetic ordering wave vector have been found at all doping levels. In the superconducting state, their spectral weight exhibits a maximum at a well-defined resonance energy whose energy depends on the doping level. A characteristic feature of this resonance mode is its sharp intensity decrease upon heating above the superconducting transition temperature. At excitation energies above or below the resonance energy, the magnetic excitations disperse to form an incommensurate double-peak structure in momentum. These dispersive excitations display an hour-glass shape in an energy-momentum-graph. The dispersion is cut off at low energies by a spin gap energy below which the intensity is suppressed.

To provide additional information about the spin excitation spectrum, perturbations such as zinc impurities and a magnetic field can be introduced. The influence of both types of perturbation on the magnetic excitation spectrum has been investigated in this thesis.

Even a small of amount of nominally spinless zinc impurities in $YBa_2(Cu_{1-y}Zn_y)_3O_x$ can drastically modify both the superconducting properties and the magnetic excitation spectrum. The most obvious change is a strong suppression of the superconducting transition temperature, which is in contrast to corresponding observations in conventional low-temperature superconductors. With the suppression of superconductivity, the spin-glass phase is extended over a larger doping range. Further impurity-specific changes were found with NMR measurements that provided evidence for a staggered local magnetic moment induced in the vicinity of the impurities reaching up to next-nearest neighbours. An indication for an effect of zinc on the low-energy magnetic excitations in cuprates came from neutron scattering measurements in $La_{2-x}Sr_xCu_{1-y}Zn_yO_4$ with various doping levels. Zinc impurities were shown to induce quasi-elastic incommensurate excitations, similarly to the static signal found in $La_{2-x-y}Nd_ySr_xCuO_4$ that is believed to be indicative of one-dimensional ("stripe") order of spins and charges. In contrast, prior measurements in optimally doped and underdoped $YBa_2(Cu_{1-y}Zn_y)_3O_x$ only detected a broad, commensurate low-energy signal. Moreover, the resonance mode found in the pure compound was reported to be progressively suppressed with increasing zinc substitution. These measurements, however, were performed on crystals with mixed twin-domains, so that the in-plane anisotropy could not be analyzed

and a detailed dispersion mapping could not be performed.

The effect of zinc impurities on the low-energy excitations and the resonance mode in detwinned underdoped $YBa_2(Cu_{1-y}Zn_y)_3O_x$ crystals is thoroughly examined in this thesis, with emphasis on the dispersion behaviour and anisotropies in the *ab*-plane. The first compound under consideration is $YBa_2(Cu_{0.98}Zn_{0.02})_3O_{6.6}$ (T_c = 30K). The zinc-free compound with this doping level had been characterized in prior work, and a resonance mode at 38 meV and a spin gap of 20 meV had been found. A calibration procedure with equivalent scans performed in both samples allows a detailed, quantitative comparison between the magnetic excitations in the zinc-substituted and the zinc-free samples. The high energy excitations are not strongly affected by Zn substitution, but the characteristic temperature dependence of the resonance mode disappears and is replaced by a more gradual evolution. The dispersion in the superconducting state of the zinc-substituted sample looks similar to the normal-state dispersion seen in the pure compound. The zinc-substituted sample also displays additional incommensurate excitations below the spin gap energy of the pure compound. These excitations exhibit a uniaxial anisotropy, i.e. the incommensurability is only see along the a^* direction in the copper oxide planes. These low-energy excitations do not show significant intensity changes upon crossing the superconducting critical temperature, and the incommensurability does not disperse noticeably with energy.

These low-energy scattering results indicate the existence of a slowly fluctuating state that competes with superconductivity. A possible interpretation of the low-energy excitations induced by Zn impurities is the stripe pinning scenario, where fluctuating spin-charge stripes are pinned by impurities and thus slow down to display low-energy magnetic excitations. Whereas the neutron scattering measurements presented here are sensitive to the spin sector, complementary evidence for static charge order around impurities came from STM studies of quasi-particles states in $Bi_{2-y}Pb_ySr_2Cu_2O_x$ and $Bi_2Sr_2Ca(Cu_{1-y}Zn_y)_2O_x$. The spatial in-plane extension of the zinc-induced localization effect was shown to be approximately five lattice spacings, in good agreement with the correlation length inferred from the neutron data. The STM data also show evidence of a one-dimensional structure around the impurities, again similar to the magnetic superstructure indicated by our neutron scattering results. Therefore zinc-induced static or slowly fluctuating spin-charge structures have been confirmed with various techniques, and some theories incorporating impurity effects were successful in explaining the low-energy spectrum modifications.

The second compound examined in this thesis with neutron scattering is $YBa_2(Cu_{0.98}Zn_{0.02})_3O_{6.45}$ ($T_c \sim$ 0K). As there is no very clear resonance feature in the pure compound at this doping level, high energy neutron scattering data were not taken. The pure compound $YBa_2Cu_3O_{6.45}$ already exhibits excitations at very low energies (spin gap < 2 meV), and no additional excitations are induced by zinc impurities. However, inter-plane correlated magnetic order was found by quasi-elastic neutron scattering in the zinc substituted sample, which is similar to what is found in the more strongly underdoped pure compound $YBa_2Cu_3O_{6.35}$ that has a similar T_c. The low-energy excitations are anisotropic in the *ab*-plane, with the signal being sharper along

the b^* direction, and their intensity decreases strongly with increasing temperature.

The observation that $YBa_2(Cu_{0.98}Zn_{0.02})_3O_{6.45}$ (T_c = 0K) and $YBa_2Cu_3O_{6.35}$ (T_c = 10K) have not only a similar T_c, but also a similar magnetic excitation spectrum is not surprising, since already magnetization measurements had shown that the magnetic properties are alike in $YBa_2(Cu_{1-y}Zn_y)_3O_x$ samples with the same T_c irrespectively of the individual oxygen content. This can be understood keeping in mind that T_c is proportional to the superconducting fluid density n_s, so that effectively it is n_s and the magnetic properties that are correlated. A simple picture for the observed inter-plane correlation is that the perturbing effect of the impurities destroys the superconducting state, bringing back short-range antiferromagnetic order that is present in very underdoped samples.

Besides the zinc-induced effects, the influence of a magnetic field on the spin excitation spectrum of pure $YBa_2Cu_3O_x$ was also examined. As cuprates are type-II superconductors, vortices will form when a magnetic field is applied perpendicular to the CuO_2-plane. The superconducting transition temperature is lowered and excitations in $YBa_2Cu_3O_x$ close to the resonance energy as well as the resonance itself are suppressed. Similar to the local zinc-induced quasi-particle states, STM measurements on cuprates had found low-energy ($\sim$ 7 meV) electronic states in the vortex cores, which have not been found in conventional superconductors. Moreover, a checkerboard modulation with a periodicity of approximately four lattice spacings is present in the field and most pronounced around the vortex cores.

Complementary to the spatially resolved techniques, prior neutron scattering measurements also found magnetic field effects on the magnetic order and magnetic excitation spectrum in the cuprates. In superoxygenated $La_2CuO_{4+\delta}$, a magnetic field was observed to enhance the static stripe order and reduce the superconducting transition temperature, which suggests that both phases compete. In that compound μSR measurements concluded that both phases coexist spatially. Neutron scattering on underdoped $La_{2-x}Sr_xCuO_4$ showed that the magnetic field can induce a static incommensurate signal and increase its inter-plane correlation. It is important to note that this magnetic field enhancement is absent if static incommensurate order is already fully saturated in zero field, which is the case at the doping level $p \sim 1/8$. Other low-energy effects of the magnetic field detected with neutron scattering include induced excitations below the spin-gap energy in optimally doped $La_{2-x}Sr_xCuO_4$ and spin-gap-closing in underdoped $La_{2-x}Sr_xCuO_4$.

In this thesis neutron scattering measurements on strongly underdoped $YBa_2Cu_3O_{6.45}$ have been performed. The static order which had been previously shown to be one-dimensional in zero-field, is strongly enhanced by an applied magnetic field. On the other hand the dynamic excitations are suppressed with the strongest suppression around $\sim$ 4 meV. The enhancement of the static signal in $YBa_2Cu_3O_{6.45}$ is likely to have a common origin with the field-induced static order in $La_{2-x}Sr_xCuO_4$. This field induced order is a likely candidate to explain the recent observation of quantum oscillations indicative of small electron and hole pockets in underdoped $YBa_2Cu_3O_x$, since static superstructures are expected to cause a reconstruction of the Fermi surface. The sup-

pression of dynamic excitations could be related to the suppression of the resonance intensity by a magnetic field in $YBa_2Cu_3O_{6.6}$. Although no clear resonance feature was detected in $YBa_2Cu_3O_{6.45}$, weak residues of the resonance effect could still be existent at low energies and respond to an applied magnetic field.

To sum up, there are several common aspects of the effect of zinc impurities and an applied magnetic field on the magnetic excitations in underdoped $YBa_2Cu_3O_x$, including the suppression of the superconducting transition temperature, the quasi-particle states induced near the impurities or vortex cores respectively, the modulated structure induced around the center of the perturbation, the suppression of the resonance feature, the enhancement of one-dimensional in-gap low-energy excitations, and the induction or enhancement of static order with inter-plane correlations. The similarity between the effects of the two perturbations suggests that their primary effect is to weaken superconductivity and enhance a state with uniaxial, incommensurate magnetic order that competes with superconductivity. The data reported in this thesis will be helpful in developing a microscopic theoretical description of the competition between these two ordering phenomena and its effects on the macroscopic physical properties of the cuprates.

Chapter 1

High temperature superconductivity

1.1 Superconductivity

Conventional superconductors A particularly interesting effect in solid matter is superconductivity. Most materials, in particular metals, have a finite conductivity to electric current. As conducting electrons pass through the material, the electrons collide with defects and lose energy to phonons, heating up the materials and hampering the electric current.

However in 1911 Kamerlingh Onnes discovered that in some materials a temperature drop below a so called *critical temperature* T_c makes the electrical resistivity vanish as if electrons do not see the atomic cores anymore. Onnes was testing a theory according to which the electron gas might freeze out at very low temperature, which only at that time became accessible with liquidification of helium. Metals were expected to become insulating, but experiments showed that instead the resistivity decreased with lower temperature. More pure metals, which were most easily achieved with Hg at that time, were found to lose their resistance to electric current completely (at $T_c \approx 4\,\mathrm{K}$ for Hg). A current in a ring would flow unstopped and the material does not acquire extra heat from the electric current (remember that the temperature of the material still has to be held below T_c).

Superconductivity turned out not to be too uncommon as many elemental metals become superconducting when cooled down to low enough temperatures. The best elemental superconductor is Nb with $T_c = 9.3\,\mathrm{K}$. It is also the main component in superconducting materials that are actually used for application nowadays - such as Nb_3Sn used for wires. The technological compounds are able to conduct large currents and withstand large magnetic field, which is a problem for common superconductors otherwise.

These early superconductors were called *conventional superconductors*. The record for the highest critical temperature was held by Nb_3Ge with $T_c \approx 23\,\mathrm{K}$ until 1986. Various applications with superconductors can be thought of, however the costly cooling procedure for liquid helium required for operation allowed actual usability only in cases where alternatives were missing.

Apart from zero resistance, all superconductors share another property which is just as important. In their superconducting state they expel magnetic fields either in the whole material, an effect called the Meissner effect , or at least they let magnetic field penetrate a periodic pattern of special regions called magnetic vortices only. Consequently depending on the material properties, superconductors are distinguished between type I (full expulsion in superconducting state) and type II (full or local expulsion in superconducting state) superconductors respectively. Whenever vortices appear, it is important for technological application that they do not move, as otherwise they dissipate energy and recreate electrical resistivity.

BCS theory of conventional superconductivity In the late 1950s Bardeen, Cooper and Schrieffer developed a successful theory for conventional superconductivity that could predict many of the experimental observations. Their model stated that below a certain transition temperature T_c electrons form states paired in momentum space $\vec{k}/-\vec{k}$ with a macroscopic condensate wave function extending over the entire crystal, so that result in quantized energy levels that are sufficiently high in energy that the conducting electrons cannot absorb energy from lattice vibrations and other low-energy events in the solid. This way they do not scatter or lose energy to heat. Effectively they move freely through the solid analogous to light passing through glass where the photons do not have enough energy to lose it to electronic excitations.

The electron pairing required at least a weak attractive interaction, which later turned out to be provided by a phonon mechanism, that acts attractively due to its time-delayed character.

High temperature superconductors A big surprise came when in 1986 Bednorz and Müller discovered a new class of materials that was superconducting at unexpectedly high temperatures. With their own ideas about oxide superconductivity in mind, they were looking for superconductivity in perovskite structure oxides based on nickel and copper. Considering the reports of metallic conductivity in $La_4BaCu_5O_{13}$, they found that the La-Ba-Cu-O system had a superconducting transition temperature of $T_c \sim 30\,\mathrm{K}$ whereas before this discovery Nb_3Ge with $T_c \approx 23\,\mathrm{K}$ held the record and conventional theory suggested that that was hard to beat. The compound with superconducting properties was identified as $La_{2-x}Ba_xCuO_4$. High pressure increased T_c, and so scientists correctly guessed that compressing the crystal structure chemically would also enhance superconductivity. Superconducting compounds with higher T_c were found to be $T_c(La_{1.8}Sr_{0.2}CuO_4) = 38\,\mathrm{K}$ and $T_c(YBa_2Cu_3O_{6.93}) = 93\,\mathrm{K}$.

In the following years many other high temperatures superconductors were discovered, most of which belong the the same class. These so-called cuprate high temperature superconductors share a two-dimensional CuO_2-plane as their key constituent (table 1.1).

In most cases compounds with a larger number of consecutive CuO_2-planes have higher T_c. The compound $Ca_{0.84}Sr_{0.16}CuO_2$ entirely made up of CuO_2-planes that are

Compound	Highest T_c
$La_{2-x}Sr_xCuO_4$	$T_c(x = 0.17) = 40\,K$
$YBa_2Cu_3O_x$	$T_c(x = 6.93) = 93\,K$
$Bi_2Sr_2Ca_2Cu_3O_{10}$	$T_c = 110\,K$
$HgBa_2CaCu_3O_8$	$T_c = 133\,K$
$HgBa_2Ca_2Cu_3O_8$ 30GPa	$T_c = 164\,K$

Table 1.1: Cuprate high temperature superconductors and their T_c at optimal doping

separated by alkaline-earth layers attracted particular interest. However, this compound is structurally very sensitive to the exact stoichiometry, and doping the CuO_2-planes has not been achieved yet.

In this work the cuprate superconductor $YBa_2Cu_3O_x$ is examined. When prepared with the optimal oxygen stoichiometry $x = 0.93$ its critical temperature is $T_c = 93\,K$, which is already above the temperature of liquid nitrogen.

Today the cuprate compound Hg-Ba-Ca-Cu-O has the highest known critical temperature of $T_c = 133\,K$ [Put93, Sch93]. When $HgBa_2Ca_2Cu_3O_8$ is subjected to a pressure of 30 GPa the critical temperature even goes up to $T_c = 164\,K$ [Chu93, Nun93].

Note that *non-cuprate* superconductors such as $Ba_{1-x}K_xBiO_3$ [Mat88, Cav88] and Rb_3C_{60} [Ros91] have been found with a fairly high transition temperature around $T_c \sim 30\,K$.

1.2 Application of high temperature superconductors

The study of high temperature superconductivity is not solely due to physical interest, but actual application in technology is possible. With an improved understanding of the physics various realizations are thinkable.

Not only elevated temperatures, but also going above a certain threshold of critical current densities J_c or above a critical magnetic field H_c can destroy superconductivity. All these factors have to be considered for successful application and still active research is done to improve the applicability of newly found superconductors.

The electric superconductivity, the Meissner effect and the flux quantization made new device possible or improved existing systems. Most notably the heat-dissipationless conductivity can be employed to create very strong magnets, which are used in medical magnetic resonance imaging or particle accelerators. Another application is the SQUID magnetic field detector which can sense signals from the heart, the brain, fatigued oil pipe lines or bridges.

Plenty of other applications can be thought of for the future, such as efficient generation, transmission (15% of costs from power transmission) and storage of electricity (SMES); detection of very small electromagnetic signals; protection of electrical grids from power surges, sags and outages; the development of fast more compact cellular

communication technology.

Goals that are unrealistic at the moment, but in principle possible in the future, are superconducting trains, nearly perfect energy storage systems and ultrafast computers (with Josephson junctions).

The high temperature aspect of the new superconductors can potentially replace conventional once and thus considerably simplifying the costly, complicating refrigeration procedures needed to drive the material into its superconducting state.

Despite their higher transition temperature, the new ceramic superconductors pose new problems, which have to be overcome for successful applications. Imperfections in the layered crystal structure can strongly lower the amount of electricity that can be carried without resistance. Moreover magnetic field could easily penetrate the material and disturb the superconducting properties. These technological challenges have been tackled with either using thin films or introducing controlled structural defects to hinder magnetic vortices from dissipation power due to their motion. Finally the ceramic character of the new superconductors makes them brittle and difficult to form into wires.

Organizations that produce instruments based on the new superconductors are Du Pont, STI, American Superconductor and many others. Whether superconductors will find their way into many areas of technology, will depend on the cost-benefit factor of this new technology.

1.3 Experimental key properties of high temperature superconductors

Class of cuprate superconductors The class of cuprate superconductors is characterized by a layered perovskite crystal structure. Conducting CuO_2-planes , which are thought as being the place where superconductivity develops, are separated by layers comprised of other elements. The intermediate layers act as charge reservoirs , inducing mobile charge carrier in the CuO_2-planes. The charge carriers can be hole-like or electron-like. The hole-doped superconductors, such as the compound $YBa_2Cu_3O_x$ subject of this work, are more commonly studied.

Difference to conventional superconductors In contrast to conventional superconductors, in high temperature superconductors there is essentially *no isotope effect* on the critical temperature of optimally-doped high temperature superconductors , i.e. upon substitution of atoms by their heavier isotopes no very pronounced changes in the energy scales are detected. The isotope effect is the most effective way to influence the phonon energies, but in contradiction to BCS theory this modification is not transferred to the superconducting properties.

Cuprate superconductors have very a *large penetration depth λ and an extremely short coherence length ξ* (only a few lattice spacings). Consequently copper oxide superconductors are extreme examples of type II superconductors, with a very high

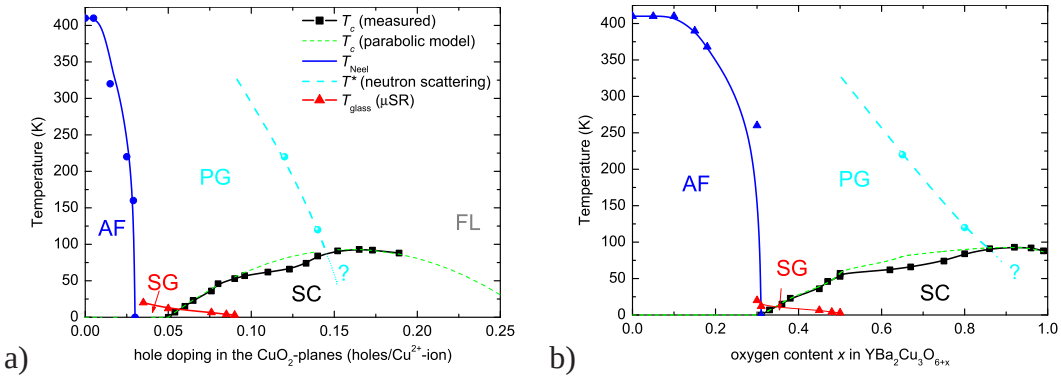

Figure 1.1: Phase diagram of hole doped cuprates as a function of temperature T and: a) hole doping p; b) oxygen content in $YBa_2Cu_3O_x$ (diagram by V. Hinkov)

critical magnetic field H_c.

Most conventional superconductors are treated theoretically with isotropic s-wave symmetry. The symmetry properties of the superconducting energy gap $\Delta(\vec{k})$ can provide indications and constraints for the correct theory. Techniques that are sensitive to $\left|\Delta(\vec{k})\right|$ as well as techniques that are phase-sensitive to $\Delta(\vec{k})$ indicated that the symmetry of high temperature superconductors is *d-wave* (references in [Map98]).

$$\Delta_{SC}(k_x, k_y) = -\Delta_{SC}(k_y, k_x)$$

The superconducting energy gap vanishes in the direction diagonal to the CuO-bond [Tsu00, Dam03]. This has important implications on the thermodynamic properties and the possible microscopic pairing mechanism.

Charge doping into the superconducting dome Superconductivity emerges only when the parent insulating compounds are modified in such a way that the CuO_2-planes aquire new charge carriers. Most effectively this is done with hole doping, i.e. when due to chemical substitution some copper ions in the CuO_2-planes deviate from their valence state Cu^{2+}. A common way to induce this charge transfer is to substitute atoms in the charge reservoir layer which in turn will draw electrons from the CuO_2-planes.

For the compound examined in this work, this is accomplished with oxygen doping of the charge reservoir layer - or chain layer in this case. By varying the oxygen content x in $YBa_2Cu_3O_x$, the compound is driven into the superconducting state with a maximum superconducting $T_c = 93K$ at $YBa_2Cu_3O_{6.93}$.

Phase diagram of cuprates Hole-doped cuprate superconductors can be characterized by their hole content per Cu in the CuO_2-planes p_h . All these superconductors share generic phase diagram (Fig. 1.1). Depending on hole-doping and temperature, the material will be in one of the following states.

The undoped compound $p_h = 0$ is an antiferromagnet, with an ordering temperature T_N of several 100 K. This order is destroyed as the hole doping is increased to $p_h = 0.02$.

Between $p_h \approx 0.05$ and $p_h \approx 0.25$, the material is superconducting at low temperatures, with a maximum T_c at around $p_h \approx 0.16$. Doping levels below optimal are called "underdoped" and doping levels above are called "overdoped" .

The normal state refers to temperatures $T > T_c$. The normal state properties in the *optimally* doped and *underdoped* regime appear to violate the Landau Fermi-liquid paradigm and some researchers share the view that it will be necessary to develop an understanding of the normal state before the superconducting state can be understood. Anomalous normal-state properties first identified in the high temperature superconductors include the electrical resistivity and Hall effect.

Anomalous normal state properties in optimally doped range The electrical resistivity $\varrho_{ab}(T)$ in the *ab*-plane of many of the hole-doped cuprate superconductors near *optimal* doping has a linear temperature dependence in a large temperature range, which is in contradiction to the Fermi liquid approximation of electrons.

$$\varrho_{ab}(T) \sim \varrho_{ab}(0) + \alpha T \qquad (T_c < T < 1000\text{K}, x_{\text{opt}})$$

with $\varrho_{ab}(0) \approx 0$ and the value α similar within different classes of cuprate materials . At the same time, depending on the compound, $\varrho_c(T)$ can be insulating ($\mathrm{d}\varrho/\mathrm{d}T < 0$) or metallic ($\mathrm{d}\varrho/\mathrm{d}T > 0$). The linear $\varrho_{ab} \propto T$ and insulating $\mathrm{d}\varrho_c/\mathrm{d}T < 0$ behaviour would indicate two-dimensional non-Fermi-liquid behaviour. It was suggested that the T-linear resistivity is due to scattering from critical fluctuations in the proximity of a quantum-critical point.

Another transport property is the Hall angle, which is temperature dependent and obeys [Chi91]

$$\cot(\theta_H) \sim AT^2 + B$$

again deviating from Fermi liquid theory.

Fermi liquid normal state properties in overdoped range In the *overdoped* regime, the normal state properties agree well with the predictions of Fermi-liquid theory. The resistivity components ϱ_{ab} and ϱ_c are both metallic in character and the in-plane resistivity ϱ_{ab} exhibits a T^2 behaviour at low temperature, as expected for processes controlled by carrier-carrier scattering [Bat94]. The Hall number is T-independent and approaches the value of the independent electron model. The ARPES experimental data show well-defined quasi-particles and agrees well with the calculated band-structure [Dam03, Zab06, And95].

Pseudogap state in underdoped range The pseudogap is an energy gap-like feature in the charge and spin-excitation spectra in the normal state of *underdoped* cuprates .

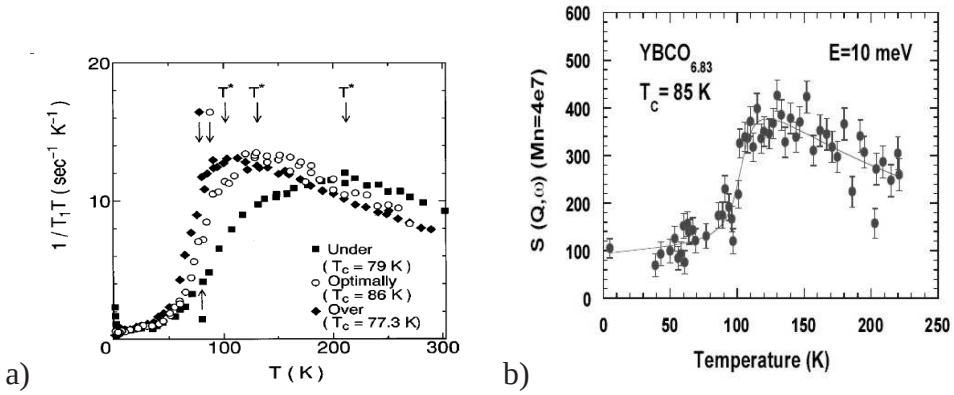

Figure 1.2: Pseudogap effect below the pseudogap temperature seen in: a) nuclear spin-lattice relaxation rate [Ish98]; b) neutron scattering intensity at Q_{AF}

It has been inferred from features in transport, magnetic, and thermal measurements including ϱ_{ab}, $R_H(T)$, thermoelectric power $S(T)$, NMR Knight shift, NMR relaxation rate, magnetic susceptibility $\chi(T)$, neutron scattering, specific heat $C(T)$, infrared absorption and ARPES (see references in [Map98]). In neutron scattering the pseudogap was observed in $YBa_2Cu_3O_x$ only for oxygen doping $x > 6.6$. The suppression at low temperatures of the spin relaxation rate and the neutron scattering intensity is shown in Fig. 1.2.

The pseudogap displays qualitatively the same k directional dependence as the superconducting gap. In terms of k_x and k_y it is larger in the $(k, 0)$ and $(0, k)$ direction and small in the (k, k) and $(k, -k)$ direction.

Different theoretical models have been proposed to explain the pseudogap. It could be a precursor of superconductivity, where Cooper pairs already exist but do not form a coherent condensate (preformed-pairs model [Tra95]; spin-singlet RVB model [Lee06]) . Alternatively it has been suggested that the pseudogap phase is indicative of a phase competing with superconductivity (for example the stripe phase [Tra95, Kiv98]).

1.4 Theories and ideas for high temperature superconductors

Paired electrons Just as the conventional superconductors, the high temperature superconductors seem to be driven by *paired electrons* - the Cooper pairs. In most conventional superconductors the pairing is mediated by a weakly attracting phononic interaction, however this origin would not be able to explain the high critical temperature of high temperature superconductors. The proximity to antiferromagnetism suggests that superconducting pairing might be mediated by *antiferromagnetic fluctuations*. This suggestion is further strengthend by the fact that the order parameter of most cuprate superconductors displays *d-wave symmetry*, which theoretically could be a natural con-

sequence of the antiferromagnetic fluctuation explanation

Role of dimensionality The physics of the high temperature superconductors is believed to be in the two-dimensional CuO_2-planes. In quantum mechanics, 1D-systems display strong correlation effects and often can be solved exactly whereas 3D systems are often well treated with weakly-coupled calculations. However, the intermediate 2D quantum mechanics turns out to be difficult to treat.

One approach consists of taking 1D corner-sharing CuO_4 chains and couple a finite number of these rungs to form ladders. It turned out that theorist could model these ladders very well and ladders with an even number of rungs display a spin gap, and moreover become superconducting when doped electronically. Two-legged ladders had a phenomenology similar to the cuprate superconductors. Ladders with an odd number of legs however did not display unusual behaviour. Two and three leg ladder compounds ($SrCu_2O_3$,$Sr_2Cu_3O_5$) have been synthesized to test the theories and so the spin gap statement was verified, however it turned out impossible to dope these compounds.

Electronic state The valence electrons in the CuO_2-planes are thought to be in copper d-orbitals that hybridize with oxygen o-orbitals, forming a band of allowed energy states that is partially filled by the electrons available. Unlike usual transition oxide compounds, the difference in energy between the oxygen and metal orbitals is very small, resulting in electronic energy bands in which the oxygen orbitals play a major role in the vicinity of the highest occupied electronic states. Consequently, the oxygen is as highly involved in the conductivity as is copper.

When the CuO_2-planes are *undoped*, the valence states of the atoms are Cu^{2+} and O^{2-}. The electronic configuration of O^{2-} is $[Be]2p^6$ whereas of Cu^{2+} it is $[Ca]3d^9$ where one electron is missing for a complete d-shell. Speaking in terms of atomic d-orbitals, the missing electron, i.e. the highest energy orbital, turns out to be one of the two electrons in the $d_{x^2-y^2}$ orbital (Fig. 1.3).

According to band theory, one would expect that the half filled band makes the compound metallic, whereas in reality it is an insulator. The resolution lies in the work of Mott who showed that if contrary to the simple non-interacting picture the electrons used so far, the electrons *do* interact due to on-site repulsion effects and in particular a half filled band can split into a so-called upper and lower Hubbard band, with an energy gap in between. This splitting occurs for the half-filled Cu^{2+} $d_{x^2-y^2}$ and the arising energy gap makes the material a Mott insulator .

Therefore introducing electron-electron interaction explains the insulating nature of the undoped parent compound which for cuprate superconductors is a Mott insulator.

In the undoped compound the spins of the valence electrons order *antiferromagnetically*. Elastic neutron scattering experiments showed that the ordered moment directions point *parallel to the CuO_2-planes*. The steep dispersion of antiferromagnetic spin waves detected by inelastic neutron scattering indicates that the superexchange

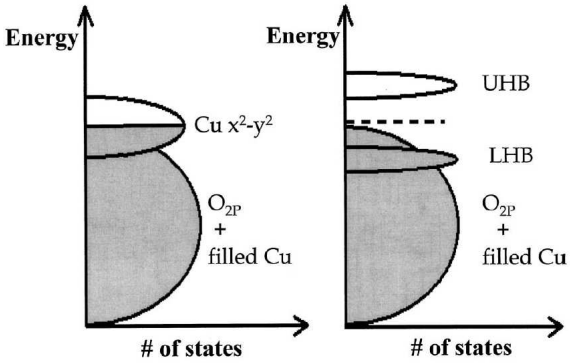

Figure 1.3: Schematic picture of energy states in cuprates and split $d_{x^2-y^2}$ band for interacting electrons (upper hubbard band, lower hubbard band) [Cav00]

interaction between neighbouring spins is very strong.

It is generally accepted that high temperature superconductivity is a result of Cooper pair formation - just as in BCS. In technical terms it is the onset of off-diagonal long-range order in the two particle density matrix. Experimentally this statement is supported by flux quantization and the Josephson effect. Upper critical field and Fermi velocity estimate the size of a Cooper pair to about $10 - 30$ Å - only moderately larger than the crystal unit cell. NMR measurements indicate that the spin state of the pairs is a *singlet state* $s = 0$.

To a good approximation, Cooper pairs form independently in the different CuO_2-planes, as inferred from the small inter-layer hopping energy deduced from c-axis resistivity measurements.

As mentioned, contrary to most conventional superconductors and the BCS theory, the isotope effect in optimally doped high temperature superconductors is only very small if at all existent. So the interaction must be all electronic in nature and involve phonons in a at most subtle way.

Chapter 2

Experimental methods and preparation of pure $YBa_2Cu_3O_x$ crystals

2.1 Neutron scattering method

2.1.1 Neutrons for science

Neutron scattering experiments require large scale facilities with a lot of technological service, i.e. table top experiments are not in sight. Research reactors for neutron scattering are located at research centers such as FRM Munich, LLB Saclay-Paris and ILL Grenoble. Spallation sources are located at ISIS Oxford and PSI Switzerland.

The main instrument used for this work is the neutron triple axis spectrometer, which I will describe in the following sections.

2.1.2 Basic triple-axis spectrometer

Scattering of a neutron at a crystal Neutrons are electrically neutral particles with a magnetic dipole moment. Traveling at a given velocity $\vec{v}$ they posses a momentum $p = \hbar\vec{k}$ and an energy E. They are connected by

$$E = \frac{mv^2}{2} \qquad \vec{p} = m\vec{v} \qquad E = \frac{\hbar^2 k^2}{2m}$$

When a neutron hits a small crystal, most of the time it will pass through without interaction. In some cases however it will scatter, either without losing energy (*elastic scattering*) or with losing energy (*inelastic scattering*). The inelastic scattering is more unlikely to occur. In general the neutron will change direction, and the scattering strength depend on the direction considered.

Mathematically its is possible to separate the scattering into a direction-*independent* contribution, which is called *incoherent scattering* $S_{\text{inc}}(E)$, and the direction-*dependent*

part, which is called *coherent scattering* $S_{\text{coh}}(E, \vec{k})$. Incoherent scattering is in general weaker than coherent scattering, but there is also a lot of variation between different atomic elements.

We denote the momentum of the neutron incident on the crystal k_i and its final momentum k_f.

$$\xrightarrow{k_i} \text{crystal} \xrightarrow{k_f}$$

The neutron can lose energy E and momentum $\vec{k}$ when being scattered in a crystal and from simple momentum conservation we can write

$$\vec{k}_i = \vec{k} + \vec{k}_f \qquad\qquad \frac{\hbar^2 k_i^2}{2m_{\text{ntrn.}}} = E + \frac{\hbar^2 k_f^2}{2m_{\text{ntrn.}}}$$

With constants plugged in the energy equation can be written

$$(k_i / \text{Å})^2 = \frac{E / \text{meV}}{2.072} + (k_f / \text{Å})^2$$

The lost momentum and energy can be associated with a quasi particle of energy E and momentum $\hbar\vec{k}$. The scattering condition can be rewritten with the transferred wavevector $\vec{k}$.

$$2\vec{k}_i \cdot \vec{k} = \frac{E}{2.072} + k^2$$

Note that for elastic scattering

$$\xrightarrow{k_i} \text{crystal}(\vec{G}) \xrightarrow{k_f} \qquad \text{(first order)}$$

the so-called *higher order* scattering is always possible

$$\xrightarrow{nk_i} \text{crystal}(n\vec{G}) \xrightarrow{nk_f} \qquad (n^{\text{th}} \text{ order})$$

as it also satisfies the scattering condition keeping the directions of the incoming and outgoing wave-vectors the same.

Principle of triple axis spectrometer In order to deduce physical processes, the energy and the momentum of the interacting neutrons have to be known. As in a neutron beam there is a broad energy distribution, the aim of the triple axis spectrometer configuration is to set up a geometry that ultimately allows only neutrons of well-defined energy and momentum to reach the sample and the detector.

Usual triple axis spectrometer scans are carried out by changing the spectrometer configuration while keeping track of the neutron flux reaching the final detector (Fig. 2.1).

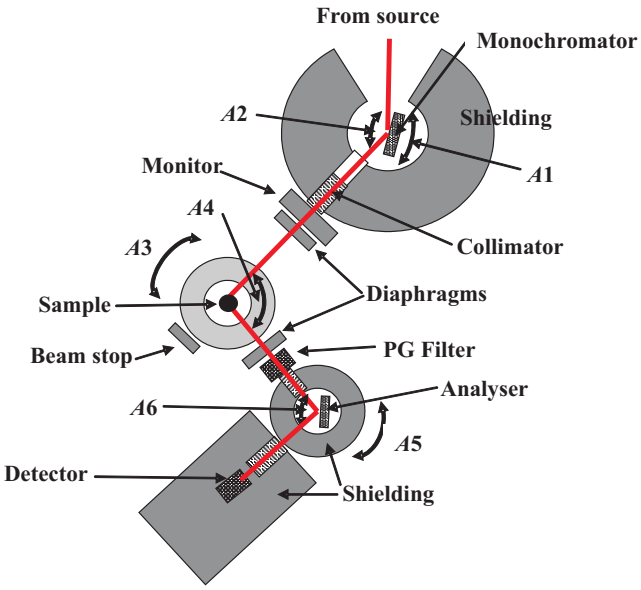

Figure 2.1: Basic setup of a neutron triple axis spectrometer (here shown IN8 Grenoble)

Source of neutrons Neutrons are present in all matter, however for creating an experimental beam of these particles, they have to be set free.

One way is to use uranium fission in reactors. The technological trouble to control the radioactivity have to be overcome, however the reward is a high neutron flux available to all instruments set up around the reactor core. For use in experiment, the high energy neutrons are slowed down with a moderator. They follow the common Maxwell-distribution for a given moderator temperature, which is close to room-temperature for so called thermal spectrometers. In the beam, the number of neutrons with a given wave-vector is

$$\mathrm{d}N_{\mathrm{ntrn.}}(k \ldots k + \mathrm{d}k) \propto k^3 e^{-24.05k^2/T}\mathrm{d}k$$

where the magnitude of the wave-vector k is measured in $\mathrm{\AA}^{-1}$ and T in K.

Alternatively spallation sources can produce intense pulses of neutrons. A proton beam is accelerated towards heavy atoms, inducing fission and neutron emission on collision. This type of source is suitable for time-of-flight spectroscopy but unsuitable for the triple-axis method, because the effective mean neutron flux turns out to be lower than at reactor sources.

The average lifetime of a *free* neutron is limited to 10.3 minutes. However, this does not affect the experiment as for example at an energy 40 meV the neutron has a velocity 2.8km/s.

Path of flight After leaving the reactor, being thermalized by moderators and collimated by neutron guides, the neutrons that are destined to reach the detector take the following path through the instrument

1. emission from reactor core
2. elastic scattering at monochromator to select neutrons with k_i
3. experimental neutron flux estimation by "monitor" neutron counter
4. *desired scattering at the crystal*; scattered neutron loses momentum $\vec{k}$ and energy E
5. filter out undesired higher order neutrons ($> k_f$)
6. elastic scattering at analyser to select neutrons with k_f
7. registration by neutron detector/counter

The monochromator , crystal and analyser are positioned and oriented in such a way that the required scattering processes are possible and no other should occur. However, despite setting the monochromator to reflect k_i and the analyser to reflect k_f, higher order reflections can not be avoided, i.e. $n \cdot k_i$ and $m \cdot k_f$ respectively will also pass, because of imperfect filter operation (step 5 above). This can result in spurious contributions of the measured neutron rate, which is discussed in a later section.

Special Si(111) or Ge(111) monochromators and analyzers do not transmit second order neutrons, however using Si(111) for monochromator and analyzer reduces the neutron flux by a factor 5 compared to using the pyrolytic graphite reflection (002), which has a large reflectivity.

Physically only the transferred momentum is significant, which leaves some freedom in choosing k_i and k_f. For simplifying the analysis of the data usually k_f is held fixed while varying k_i. Due to the working principles of the filter set on k_f, the most commonly chosen values are $k_f = 2.662\,\text{Å}^{-1}$, $k_f = 4.1\,\text{Å}^{-1}$ for a graphite filter and $k_f = 1.55\,\text{Å}^{-1}$ for a beryllium filter. The choice needs to consider the constraints from the required wave-vector transfer at the crystal and also there is a difference in transmission of "good" neutrons and suppression of unwanted higher order neutrons. See Fig. 2.2 for the transmission properties of graphite at various incident energies and wavevectors. The marked wave vectors illustrate how the first order has a high transmission, whereas multiples of that wave length (higher orders) are mostly suppressed.

Background noise and shielding This is the ideal path of a neutron, however one has to take special care to avoid any stray neutrons reaching the detector through other ways. Special absorbing materials can be employed to shield external sources and shortcuts as much as possible. Cadmium is a good absorber, however it reemits high energy gamma radiation. Boron is generally weaker, but a better absorber for very high energy neutrons. Lithium is even weaker, but on the other hand it does not emit gamma radiation.

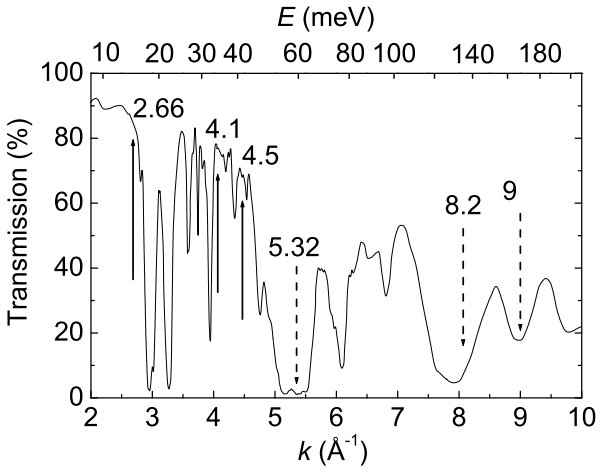

Figure 2.2: Transmission of graphite filter as a function of energy

Detection of neutrons In the detector the neutron events are simply counted. For example neutrons interact with helium, creating a proton which can be picked up by an electrode. This count rate should be normalized by the monitor count rate for quantitative comparison of scattering intensities.

2.1.3 Geometrical interpretation of scattering in momentum space

The conservation of momentum during scattering can for visualization be expressed geometrically as vectors (Fig. 2.3). This representation is called the scattering triangle. The distance between the midpoint of k and the foot of the perpendicular on k is $E/(2k \cdot 2.072\,\mathrm{meV\AA^{-2}})$. This distance is independent of k_i and k_f and thus knowing $\vec{k}$ and E one can visualize possible k_f and k_i. The scattering vectors, including the scattering at the monochromator and the analyzer are shown in Fig. 2.4.

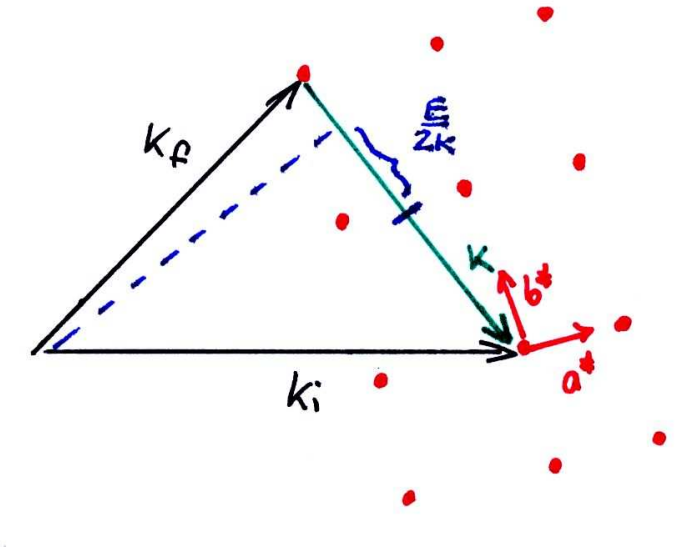

Figure 2.3: Scattering triangle with incoming neutron momentum k_i, outgoing neutron momentum k_f, transfered momentum k (green), crystal reciprocal lattice (red). The scattering of the (-1,2,0) reflection is shown as an example. In blue, a statement is made that can be useful to understand the scattering triangle (E has to be converted by dividing through $2.072\,\mathrm{meV\,\AA^{-2}}$)

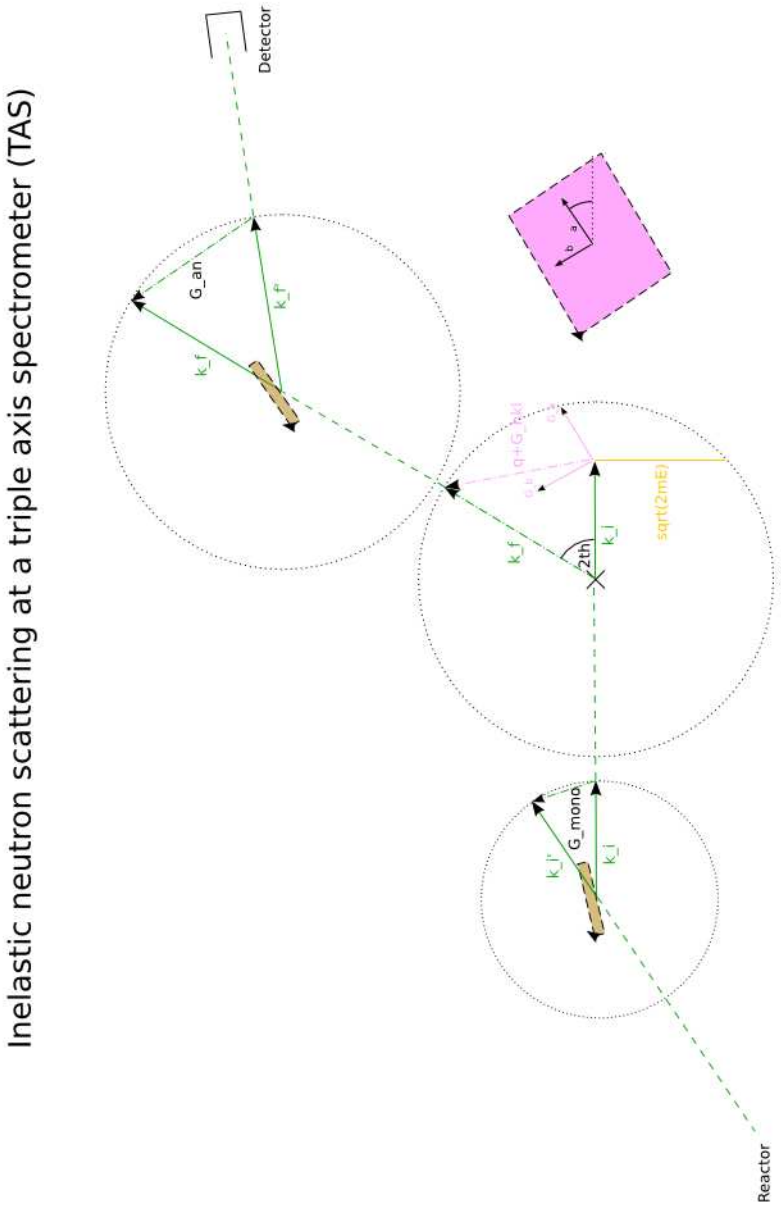

Figure 2.4: Path of the neutron from reactor, to analyzer, to sample, to monochromator and to the detector. Sample orientation and sample reciprocal lattice vectors shown in pink

2.1.4 Scattering cross-section, scattering functions and fluctuation-dissipation theorem

In this section the theoretical approach to quantum-mechanically calculate the neutron scattering cross-section σ is outlined. A complete theoretical treatment can be found in [Squ97, Lov86]. The scattering cross-section per spherical angle $\mathrm{d}\Omega$ and final energy range $\mathrm{d}E_f$ is defined by

$$\frac{\mathrm{d}^2\sigma}{\mathrm{d}\Omega\mathrm{d}E_f} = \frac{\text{scattered neutrons in energy range } E_f \text{ per time into solid angle } \mathrm{d}\Omega}{\text{incoming neutrons per time per area} \cdot \mathrm{d}\Omega\mathrm{d}E_f}$$

The neutron is scattered from condensed matter by virtue of two fundamental interactions: the strong force interaction with atomic nuclei and the electric dipole interaction with electronic magnetic moments. Electric dipole interactions with nuclear spins result only in incoherent scattering and are irrelevant here.

Using *Fermi's Golden rule* for the scattering potential V the scattering cross-section for a final energy range $E_f \ldots E_f + \mathrm{d}E_f$ into a spherical angle $\mathrm{d}\Omega$ is

$$\frac{\mathrm{d}^2\sigma}{\mathrm{d}\Omega\mathrm{d}E_f} = \frac{k_f}{k_i}\left(\frac{m_n}{2\pi\hbar^2}\right)^2 \left|\left\langle k_f\sigma_f\psi_f^c \,\middle|\, V \,\middle|\, k_i\sigma_i\psi_i^c\right\rangle^2\right| \delta(\hbar\omega + E_i^c - E_f^c)$$

with the incident neutron momentum k_i, scattered neutron momentum k_f, neutron mass m_n, initial neutron spin σ_i, final neutron spin σ_f, initial crystal wave function ψ_i^c, final crystal wave function ψ_f^c, transferred energy $\hbar\omega$, the initial total crystal energy E_i^c, the final total crystal energy E_f^c. Note that for clarity the neutron and sample related variables are coloured.

Averaging over initial states (usually Boltzmann distributed) and summing over final states yields

$$\frac{\mathrm{d}^2\sigma}{\mathrm{d}\Omega\mathrm{d}E_f} = \frac{k_f}{k_i}\left(\frac{m_n}{2\pi\hbar^2}\right)^2 \sum_{\psi_i^c\psi_f^c\sigma_i\sigma_f} p_{\psi_i^c\sigma_i} \left|\left\langle k_f\sigma_f\psi_f^c \,\middle|\, V \,\middle|\, k_i\sigma_i\psi_i^c\right\rangle^2\right| \delta(\hbar\omega + E_i^c - E_f^c) \tag{2.1}$$

with the pre-scattering initial quantum state probability $p_{\psi_i^c\sigma_i}$.

For a periodic potential $V = \sum_j V_j(\vec{r} - \vec{R}_j)$ expressed as its Fourier transform $V_j(\vec{k})$ we get

$$\frac{\mathrm{d}^2\sigma}{\mathrm{d}\Omega\mathrm{d}E_f} = \frac{k_f}{k_i}\left(\frac{m_n}{2\pi\hbar^2}\right)^2 \sum_{\psi_i^c\psi_f^c\sigma_i\sigma_f} p_{\psi_i^c\sigma_i} \left|\sum_j V_j(\vec{k}) \left\langle k_f\sigma_f\psi_f^c \,\middle|\, e^{\mathrm{i}\vec{k}\cdot\vec{R}_j} \,\middle|\, k_i\sigma_i\psi_i^c\right\rangle^2\right| \delta(\hbar\omega + E_i^c - E_f^c) \tag{2.2}$$

where $\hbar\vec{k}$ turns out to be the transferred momentum.

Nuclear neutron scattering

A single nucleus at position $\vec{R}$ is considered to be point-like and is treated as a Fermi pseudopotential and its Fourier transform

$$V_j(\vec{r}) = \frac{2\pi\hbar^2}{m_n} b_{\vec{R}} \delta(\vec{r} - \vec{R})$$
$$V_j(\vec{k}) = \frac{2\pi\hbar^2}{m_n} b_{\vec{R}}$$

where $b_{\vec{R}}$ is the scattering length . The nucleus scatters an incoming wave e^{ikz} isotropically to an s-wave outgoing wavefunction $-b/r \cdot e^{ikr}$. The scattering length b depends on the total spin of the neutron-nucleus system during scattering, therefore two values are possible from the spin combination rules of the spin ½ neutron. Some nuclei show complex b dependences on the neutron energy due to excited states (^{103}Rh, ^{113}Cd, ^{157}Gd, ^{176}Lu).

From equation 2.2 and the assumption that the nuclear spins are uncorrelated the scattering cross-section for the nuclear scattering potential is

$$\frac{\mathrm{d}^2\sigma}{\mathrm{d}\Omega \mathrm{d}E_f} = \frac{k_f}{k_i} \sum_{\psi_i^c \psi_f^c} p_{\psi_i^c} \left| \left\langle k_f \psi_f^c \left| \sum_{\vec{R}} b_{\vec{R}} e^{i\vec{k}\cdot\vec{R}} \right| k_i \psi_i^c \right\rangle \right|^2 \delta(\hbar\omega + E_i^c - E_f^c) \tag{2.3}$$

To separate the scattering length, Heisenberg operators $\vec{R}(t) = e^{i\hat{H}t/\hbar}\vec{R}e^{-i\hat{H}t/\hbar}$ can be introduced for the time dependent nucleus positions $\vec{R}$

$$\frac{\mathrm{d}^2\sigma}{\mathrm{d}\Omega \mathrm{d}E_f} = \frac{k_f}{k_i} \frac{1}{2\pi\hbar} \sum_{\vec{R}\vec{R}'} b_{\vec{R}} b_{\vec{R}'} \int_{-\infty}^{\infty} \sum_{\psi_i^c} p_{\psi_i^c} \left\langle \psi_i^c \left| e^{-i\vec{k}\cdot\vec{R}'(0)} e^{i\vec{k}\cdot\vec{R}(t)} \right| \psi_i^c \right\rangle e^{-i\omega t} \mathrm{d}t$$

Assuming that scattering lengths are *not correlated* (nuclear moments do not interact)

$$\overline{b_{\vec{R}'} b_{\vec{R}}} = (\overline{b})^2 \qquad \vec{R} \neq \vec{R}'$$
$$\overline{b_{\vec{R}'} b_{\vec{R}}} = \overline{b^2} \qquad \vec{R} = \vec{R}'$$

the total cross-section can be split into *coherent* and *incoherent* scattering

$$\left(\frac{\mathrm{d}^2\sigma}{\mathrm{d}\Omega \mathrm{d}E_f}\right)_{\mathrm{coh}} = \frac{\sigma_{\mathrm{coh}}}{4\pi} \frac{k_f}{k_i} \frac{1}{2\pi\hbar} \sum_{\vec{R}\vec{R}'} \int_{-\infty}^{\infty} \left\langle e^{-i\vec{k}\cdot\vec{R}'(0)} e^{i\vec{k}\cdot\vec{R}(t)} \right\rangle e^{-i\omega t} \mathrm{d}t$$
$$\left(\frac{\mathrm{d}^2\sigma}{\mathrm{d}\Omega \mathrm{d}E_f}\right)_{\mathrm{inc}} = \frac{\sigma_{\mathrm{inc}}}{4\pi} \frac{k_f}{k_i} \frac{1}{2\pi\hbar} \sum_{\vec{R}} \int_{-\infty}^{\infty} \left\langle e^{-i\vec{k}\cdot\vec{R}(0)} e^{i\vec{k}\cdot\vec{R}(t)} \right\rangle e^{-i\omega t} \mathrm{d}t$$

with the scattering cross-sections

$$\sigma_{\text{coh}} = 4\pi(\overline{b})^2$$
$$\sigma_{\text{inc}} = 4\pi\left(\overline{b^2} - (\overline{b})^2\right)$$

Incoherent scattering is of the nucleus with itself at different times which therefore does not give interference effects, i.e. it is isotropic. It arises from the the random distribution of the deviations of the scattering lengths from their mean value. A single isotope with zero spin would be purely coherent.

Nuclear scattering with energy transfer gives rise to phonon excitation. However, these processes are not considered in this work. Therefore the following paragraph only describes results of elastic nuclear scattering $\omega = 0$.

Elastic nuclear scattering from the crystal lattice The coherent and incoherent contribution from the static crystal structure $\omega = 0$ giving rise to Bragg peaks is

$$\left(\frac{\mathrm{d}\sigma}{\mathrm{d}\Omega}\right)_{\text{coh el}} = N\frac{(2\pi)^3}{V_0}\sum_{\vec{G}}\delta(\vec{k}-\vec{G})\left|F_N(\vec{k})\right|^2$$
$$\left(\frac{\mathrm{d}\sigma}{\mathrm{d}\Omega}\right)_{\text{inc el}} = N\sum_d \frac{\sigma_{d,\text{inc}}}{4\pi}e^{-2W_d}$$

where

$$F_N(\vec{k}) = \sum_d \overline{b}_d e^{\mathrm{i}\vec{k}\cdot\vec{d}}e^{-W_d} \qquad \text{(nuclear unit-cell structure factor)}$$

$$W_d = \frac{\hbar}{4M_dN}\sum_{s=\vec{q}}\frac{\left|\vec{k}\cdot\vec{e}_{ds}\right|}{\omega_s}\langle 2n_s+1\rangle \qquad \text{(Debye-Waller factor)}$$

with total unit cell number N, unit cell volume V_0, atoms in the unit cell d, phonon polarization vector $\vec{e}_{ds}$, phonon frequency ω_s, phonon mode number n_s, atomic mass of atom in unit cell M_d, and phonon frequency ω_s.

Consequently scattering peaks will be found at reciprocal wave vector $\vec{G}$ only, however the intensity can be modulated and due to special unit cell structures some peak could even be suppressed.

Magnetic neutron scattering

The main interaction of interest for this thesis, is when the *neutron dipole moment* $\vec{\mu}$ experiences the *magnetic field of the electrons* $\vec{B}_e$

$$V = -\vec{\mu}\cdot\vec{B}^e$$

The neutron moment derived from its spin and the electron magnetic field from Biot-Savarts law for the electron magnetic dipole and its motion

$$\vec{\mu} = -(\gamma \mu_N \hat{\vec{\sigma}})$$
$$\vec{B}_i^e = \nabla \times \left(\frac{\mu^{e_j} \times \vec{R^{ne}_j}^{\,0}}{\vec{R^{ne}_j}^{\,2}} - \frac{e}{c} \frac{v^{e_j} \times \vec{R^{ne}_j}^{\,0}}{\vec{R^{ne}_j}^{\,2}} \right)$$

with the symbols γ the nuclear gyromagnetic ratio, μ_N the nuclear magneton, $\hat{\vec{\sigma}}$ the spin operator, μ^{e_j} the electron dipole moment, v^{e_j} the electron velocity, e the electron charge, c the speed of light and $\vec{R^{ne}_j}$ the distance vector between electron and neutron.

With equation 2.1 the scattering cross-section is

$$\frac{\mathrm{d}^2\sigma}{\mathrm{d}\Omega \mathrm{d}E_f} = \frac{k_f}{k_i} \left(\frac{m_n}{2\pi\hbar^2} \right)^2 \sum_{\psi_i^c \psi_f^c \sigma_i \sigma_f} p_{\psi_i^c \sigma_i} \left| \left\langle k_f \sigma_f \psi_f^c \left| -\vec{\mu} \cdot \vec{B}^e \right| k_i \sigma_i \psi_i^c \right\rangle^2 \right| \delta(\hbar\omega + E_i^c - E_f^c)$$
$$= (\gamma r_0)^2 \frac{k_f}{k_i} \sum_{\psi_i^c \psi_f^c \sigma_i \sigma_f} p_{\psi_i^c \sigma_i} \left| \left\langle \sigma_f \psi_f^c \left| \hat{\vec{\sigma}} \cdot \tilde{Q}_\perp \right| \sigma_i \psi_i^c \right\rangle^2 \right| \delta(\hbar\omega + E_i^c - E_f^c)$$

where the effective magnetization is

$$\tilde{Q}(\vec{x}) = \sum_{e_j} \delta(\vec{r} - \vec{r}^{e_j}) \left\{ \frac{\hbar}{2} \hat{\sigma}^{e_j} - \frac{\mathrm{i}}{\hbar k} (\vec{k}^0 \times \hat{P}^{e_j}) \right\}$$
$$\therefore \tilde{Q}(\vec{k}) = \sum_{e_j} \left\{ \frac{\hbar}{2} \hat{\sigma}^{e_j} - \frac{\mathrm{i}}{\hbar k} (\vec{k}^0 \times \hat{P}^{e_j}) \right\} e^{\mathrm{i}\vec{k} \cdot \vec{r}^{e_j}}$$
$$\therefore \tilde{Q}_\perp(\vec{k}) = \vec{k}^0 \times (\tilde{Q} \times \vec{k}^0) = \tilde{Q} - (\tilde{Q} \cdot \vec{k}^0) \vec{k}^0$$
$$= \sum_{e_j} \left\{ \vec{k}^0 \times \left(\frac{\hbar}{2} \hat{\sigma}^{e_j} \times \vec{k}^0 \right) - \frac{\mathrm{i}}{\hbar k} (\vec{k}^0 \times \hat{P}^{e_j}) \right\} e^{\mathrm{i}\vec{k} \cdot \vec{r}^{e_j}}$$

with $\hat{P}^{e_j}$ the electron momentum operator, $\vec{k}^0$ the unit vector of the transferred momentum, $\vec{r}^{e_j}$ the crystal position, and the classical electron radius

$$r_0 = \frac{\mu_0}{4\pi} \frac{e^2}{m_e} \qquad (\gamma r_0)^2 = 0.3\,\mathrm{b}$$

where the unit barns stands for $1\,\mathrm{b} = 10^{-28}\,\mathrm{m}$. The connection to the physics of the material lies in the the knowledge about the wave-functions ψ_f^c.

It is useful to separate into components

$$\frac{\mathrm{d}^2\sigma}{\mathrm{d}\Omega \mathrm{d}E_f} = (\gamma r_0)^2 \frac{k_f}{k_i} \sum_{\alpha,\beta=x,y,z} \sum_{\psi_i^c \psi_f^c} p_{\psi_i^c} \left\langle \psi_i^c \left| \tilde{Q}_{\perp\alpha}^\dagger \right| \psi_f^c \right\rangle \left\langle \psi_f^c \left| \tilde{Q}_{\perp\beta} \right| \psi_i^c \right\rangle$$
$$\sum_{\sigma_i \sigma_f} p_{\sigma_i} \left\langle \sigma_i \left| \hat{\vec{\sigma}}_\alpha^\dagger \right| \sigma_f \right\rangle \left\langle \sigma_f \left| \hat{\vec{\sigma}}_\beta \right| \sigma_i \right\rangle \delta(\hbar\omega + E_i^c - E_f^c)$$

Unpolarized magnetic scattering For unpolarized neutrons the spin up and down state of neutrons are equally likely

$$\sum_{\sigma_i\sigma_f} p_{\sigma_i} \left\langle \sigma_i \left| \hat{\vec{\sigma}}^{\dagger}_{\alpha} \right| \sigma_f \right\rangle \left\langle \sigma_f \left| \hat{\vec{\sigma}}_{\beta} \right| \sigma_i \right\rangle = \delta_{\alpha\beta}$$

We obtain

$$\left(\frac{\mathrm{d}^2\sigma}{\mathrm{d}\Omega \mathrm{d}E_f}\right)_{\mathrm{unp}} = (\gamma r_0)^2 \frac{k_f}{k_i} \sum_{\alpha,\beta=x,y,z} (\delta_{\alpha\beta} - \vec{k}^0_{\alpha}\vec{k}^0_{\beta}) \sum_{\psi^c_i\psi^c_f} p_{\psi^c_i} \left\langle \psi^c_i \left| \tilde{Q}^{\dagger}_{\alpha} \right| \psi^c_f \right\rangle \left\langle \psi^c_f \left| \tilde{Q}_{\beta} \right| \psi^c_i \right\rangle \delta(\hbar\omega + E^c_i - E^c_f)$$

and rewriting the $\delta(x)$ function as an integral we find

$$\left(\frac{\mathrm{d}^2\sigma}{\mathrm{d}\Omega \mathrm{d}E_f}\right)_{\mathrm{unp}} = (\gamma r_0)^2 \frac{k_f}{k_i} \sum_{\alpha\beta} (\delta_{\alpha\beta} - \vec{k}^0_{\alpha}\vec{k}^0_{\beta}) \frac{1}{2\pi\hbar} \int_{-\infty}^{\infty} \mathrm{d}t e^{\mathrm{i}\omega t} \left\langle \tilde{Q}_{\alpha}(-\vec{k}, 0) \tilde{Q}_{\beta}(\vec{k}, t) \right\rangle_{\psi^c_i}$$

where the Heisenberg operator is

$$\tilde{Q}(\vec{k}, t) = e^{\mathrm{i}\hat{H}t/\hbar} \tilde{Q}(\vec{k}) e^{-\mathrm{i}\hat{H}t/\hbar}$$

Elastic unpolarized magnetic scattering In elastic scattering $\omega = 0$ we can simplify to

$$\begin{aligned}\left(\frac{\mathrm{d}\sigma}{\mathrm{d}\Omega}\right)_{\mathrm{el,unp}} &= (\gamma r_0)^2 \sum_{\alpha\beta} (\delta_{\alpha\beta} - \vec{k}^0_{\alpha}\vec{k}^0_{\beta}) \left\langle \tilde{Q}_{\alpha}(-\vec{k}) \right\rangle_{\psi^c_i} \left\langle \tilde{Q}_{\beta}(\vec{k}) \right\rangle_{\psi^c_i} \\ &= (\gamma r_0)^2 \left| \left\langle \tilde{Q}_{\perp}(\vec{k}) \right\rangle_{\psi^c_i} \right|^2\end{aligned}$$

which effectively states that the scattering cross-section is proportional to the perpendicular component of the effective magnetization of the electrons.

2.1.5 Modulations deduced from basic scattering theory

Periodicities and patterns in the crystal structure will give rise to predictable outcomes in the scattering results, which effectively represent the Fourier transform of the real space structure. Some special cases are considered here.

Form factors A crystal is made of unit cells which repeat infinitely. From general scattering theory of waves it is known that if the unit cell contains more that one atom, the scattering factor for an incident wave of wavevector $\vec{k}$ has an intensity proportional to

$$S(\vec{k}) = \sum_{i=\mathrm{atoms}} A_i e^{\mathrm{i}\vec{k}\cdot\vec{r}_i}$$

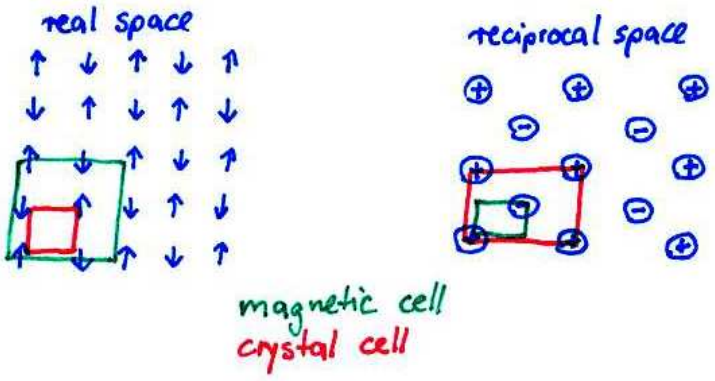

Figure 2.5: Schematic picture of 2D antiferromagnetic spins and the expected reflections shown in reciprocal space

where A_i is the scattering strength of the atom i. The scattering function $S(\vec{k})$ is proportional to the scattering cross-section σ.

Using coordinates relative to the unit cell

$$\vec{k} = h\vec{a}^* + k\vec{b}^* + l\vec{c}^*$$
$$\vec{r}_i = x_i\vec{a} + y_i\vec{b} + z_i\vec{c}$$

and for an *orthogonal* unit cell

$$\vec{a}^* = \frac{2\pi}{a}\vec{a}^0 \qquad \vec{b}^* = \frac{2\pi}{b}\vec{a}^0 \qquad \vec{c}^* = \frac{2\pi}{c}\vec{a}^0$$

this simplifies to

$$S(h,k,l) = \sum_{i=\text{atoms}} A_i e^{2\pi\mathrm{i}(hx_i+ky_i+lz_i)}$$

By the periodicity of the unit cell, only integer values of h,k,l give rise to scattering $S \neq 0$.

Form factor of a 2D antiferromagnet For example let us take a 2D antiferromagnet with the unit cell depicted in Fig 2.5. The scattering atoms are at positions $x = 0, y = 0$ and $x = 1/2, y = 1/2$ for atom of spin up with scattering amplitude A_1 and $x = 1/2, y = 0$ and $x = 1/2, y = 0$ for atom of spin down with scattering amplitude A_2. The structure factor would be

$$S(h,k,l) = A_1(1 + e^{\mathrm{i}\pi(h+k)}) + A_2(e^{\mathrm{i}\pi(k)} + e^{\mathrm{i}\pi(h)})$$

The measured scattering intensity is $|S|^2$ and therefore

$$I = |S|^2 = \begin{cases} 4(A_1 + A_2)^2 & \text{for } h \text{ and } k \text{ even} \\ 4(A_1 - A_2)^2 & \text{for } h \text{ and } k \text{ odd} \\ 0 & \text{for } h \text{ and } k \text{ one even one odd} \end{cases}$$

We see that there is a systematic extinction if only one of h or k is odd.

In Fig 2.5 we show the expected reflections, but this time in terms of $h_{\text{crystal}} = \frac{1}{2}h_{\text{AF}}$ and $k_{\text{crystal}} = \frac{1}{2}k_{\text{AF}}$. Half of the reflections will be masked by the crystal Bragg peaks, but we will see the other reflections at $(n + 1/2, m + 1/2)$ $(n, m \in \mathbb{Z})$, which are the reflections that one can see in every antiferromagnet. We will call these positions antiferromagnetic wave-vector Q_{AF}.

Bilayer modulation The compound $YBa_2Cu_3O_x$ has a pair of CuO_2-planes per unit cell. This structure in the unit cell will also result in a special form factor for a signal from any physics that takes place in the CuO_2-planes. This double plane structure with a defined bilayer separation along the c-axis will give an L dependent modulation.

Depending on whether the inter-bilayer correlations are in-phase or out-of-phase, two eigenmode modulations will arise. One for "odd" modes and one for "even" modes.

$$S_{\text{odd}} \propto \sin^2\left(\frac{\pi L}{3.4}\right) \tag{2.4}$$

$$S_{\text{even}} \propto \cos^2\left(\frac{\pi L}{3.4}\right) \tag{2.5}$$

The constant 3.4 derives from the bilayer separation distance. In this work only bilayer physics with "odd" inter-bilayer-phase are considered.

Incommensurate modulation Any ideally periodic structure $\cos(kx)$ will produce a sharp scattering peak at momentum transfer k. As a special case this periodic structure could be modulated by a factor $(\cos(kx)\cos(k_\delta x))$ and rewriting shows that this results in satellite peaks in the scattering experiment

$$\cos(kx)\cos(k_\delta x) = \frac{1}{2}\left(\cos\left((k + k_\delta)x\right) + \cos\left((k - k_\delta)x\right)\right)$$

A scattering experiment will detect the components of the Fourier transform and such signals at $k + k_\delta$ and $k - k_\delta$ are termed incommensurate, as their modulation periodicity k_δ is usually not commensurate with the crystal periodicity.

2.1.6 Magnetic susceptibility and fluctuation-dissipation theorem

Neutron scattering measurements determine the scattering cross-section, however another quantity, the susceptibility, has a more direct physical meaning. The relation between these two quantities is shown in the next paragraphs.

Complex susceptibility Many physical responses to stimuli can be examined with the abstract concept of a linear susceptibility. Let us define a *general force* f and *order parameter* s. The free energy functional would be equal to

$$F(t) = -\int \mathrm{d}\vec{x} f(\vec{x}, t) s(\vec{x}, t)$$

Common examples for [order parameter and general force] are [particle density and external potential] or [magnetization and external magnetic field] respectively.

The physical question is how the order parameter will respond to the external force. If the force is weak we can presume a linear response, but possibly one which is non-local in space and time. In mathematical terms this can be expressed as a convolution

$$s(\vec{x},t) = \int \mathrm{d}\vec{x}' \int_{-\infty}^{t} \mathrm{d}t' \chi(\vec{x}-\vec{x}', t-t') f(\vec{x}', t')$$

where $\chi(\vec{x},t)$ is the susceptibility. A convolution has a much simpler representation after a Fourier transform of space and time

$$\tilde{s}(\vec{k},\omega) = \tilde{\chi}(\vec{k},\omega)\tilde{f}(\vec{k},\omega)$$

Although the real-space susceptibility is real, the Fourier transform can be a complex number

$$\tilde{\chi}(\vec{k},\omega) = \chi'(\vec{k},\omega) + \mathrm{i}\chi''(\vec{k},\omega)$$

The real and imaginary part can be interpreted as the in-phase (reactive) response χ' and lagging (dissipative) response χ''.

The *static susceptibility* is given by $\tilde{\chi}_0(\vec{k}) = \tilde{\chi}(\vec{k}, \omega = 0)$. One can show that the spatially averaged order parameter obeys

$$\left\langle \langle s \rangle_{\vec{x}}^2 \right\rangle_t = \frac{k_B T \chi_0(0)}{V}$$

where V is the volume. In the thermodynamic limit $V \to \infty$ the spatially average quantities vanish.

Kramer-Kronig relations The susceptibility obeys *causality*, i.e. the effect cannot precede the cause. This can be expressed as the statement that $\chi(t)$ is real-valued on the half-line $t > 0$. Together with complex analysis it is now possible to derive a relation between the real and imaginary part of $\tilde{\chi}$.

$$\tilde{\chi} = \frac{1}{\pi \mathrm{i}} \int_{-\infty}^{\infty} \frac{\tilde{\chi}(\omega')}{\omega' - \omega} \mathrm{d}\omega' \qquad \text{(Kramer-Kronig)}$$

$$\therefore \chi'(\omega) = \frac{2}{\pi} \int_0^{\infty} \chi''(\omega') \frac{\omega'}{\omega'^2 - \omega^2} \mathrm{d}\omega' \tag{2.6}$$

$$\chi''(\omega) = -\frac{2\omega}{\pi} \int_0^{\infty} \chi'(\omega') \frac{1}{\omega'^2 - \omega^2} \mathrm{d}\omega' \tag{2.7}$$

where the final form has made use of the equation $\chi''(\omega) = -\chi''(-\omega)$. Therefore from the knowledge of the imaginary part alone it is in principle possible to calculate the real part.

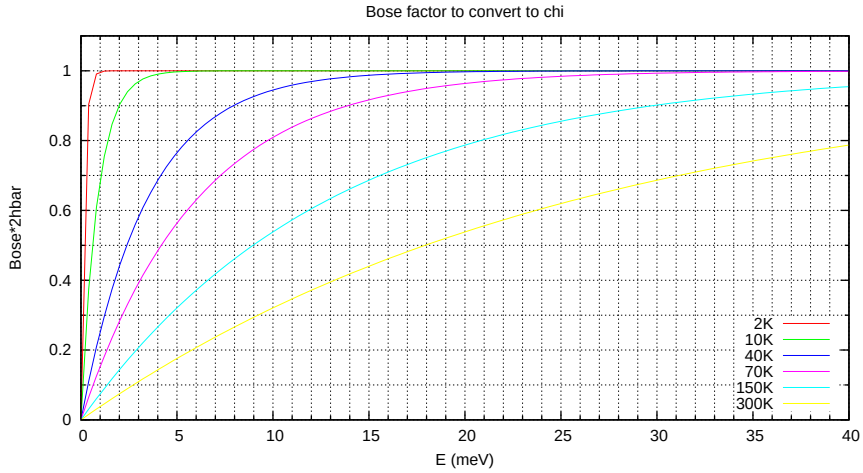

Figure 2.6: Bose factor $1 - \exp(-11.6E/T)$ to be used to scale the scattering cross-section to χ''

Dissipations and fluctuations To see why χ'' also corresponds to the dissipation be calculate the average power dissipated from

$$p = \langle f \mathrm{d}s \rangle = \lim_{T\to\infty} \frac{1}{T} \int_0^T f(t) \frac{\partial s}{\partial t} \mathrm{d}t$$

where the spatial dependence has been ignored for simplicity. Assuming a sinusoidal force $f(t) = \Re(f_\omega e^{-\mathrm{i}\omega t})$ we can deduce that

$$p(\omega) = \frac{\omega |f_\omega|^2}{2} \chi''(\omega)$$

from what we can see why χ'' is called the dissipative response.

The imaginary susceptibility $\chi''(\vec{k},\omega)$ can be related to the correlation function $S(\vec{k},t) = \left\langle s(\vec{k},t) s(\vec{k}+\vec{r},t+\tau) \right\rangle_{\vec{r},\tau}$ by

$$\chi''(\vec{k},\omega) = \frac{1}{2\hbar}(1 - e^{-\beta\hbar\omega})\tilde{S}(\vec{k},\omega) \qquad \text{(fluctuation-dissipation theorem)} \tag{2.8}$$

$$= \frac{1}{2\hbar}(1 - e^{-11.6\,\mathrm{K}/\,\mathrm{meV}\cdot E/T})\tilde{S}(\vec{k},\omega) \tag{2.9}$$

$$\chi''(\vec{k},\omega) \propto (1 - e^{-11.6\,\mathrm{K}/\,\mathrm{meV}\cdot E/T})\sigma(\vec{k},\omega)$$

The prefactor, which is called the Bose factor, is plotted in Fig. 2.6 Note that at high temperatures

$$1 - e^{-\beta\hbar\omega} \sim \beta\hbar\omega \qquad \text{(high } T\text{)}$$

This will be important in the neutron data analysis, as neutron scattering measures $\tilde{S}(\vec{k},\omega)$ whereas for physical interpretations quite often χ is the more natural quantity.

2.1.7 Data analysis methods of neutron scattering data

Treatment of single data point A data point consists of all its configuration parameters such as Q, E, T and k_f and also the resultant counts C measured in this configuration while counting until a the neutron monitor reaches incident counts M.

Usually the transferred momentum Q is given in the system of reciprocal axes a^*, b^* and c^*. For an *orthorhombic* crystal system these axes are

$$\vec{a}^* = \frac{2\pi}{|\vec{a}|}\vec{a}^0 \qquad \vec{b}^* = \frac{2\pi}{|\vec{b}|}\vec{b}^0 \qquad \vec{c}^* = \frac{2\pi}{|\vec{c}|}\vec{c}^0$$

Each components of Q divided by the reciprocal axes length gives Q in terms of reciprocal lattice units r.l.u. All wave vectors in this thesis are given in reciprocal lattice units.

$$\vec{Q} = (H, K, L)\,\text{r.l.u.} = \left(\frac{2\pi}{a}H, \frac{2\pi}{b}K, \frac{2\pi}{c}L\right)$$

As neutron scattering is a small probability, high number process (large number of neutron that could scatter potentially), it is described by Poisson statistics. For that reason the estimated value of the real model counts $\tilde{C}$, which is deduced from the value of the measured counts is $\tilde{C} = C$ and the error is the Poisson error $\Delta\tilde{C} = \sqrt{C}$ (more precisely $\sigma_\mu = \sqrt{k+1}$, but the difference is small).

$$\tilde{C} = C \pm \sqrt{C}$$

Usually one is interested in the count rate normalized by monitor. Therefore the end result for a measured count rate C at monitor M is

$$\binom{C}{M} \rightarrow \frac{C}{M} \pm \frac{\sqrt{C}}{M}$$

Note that the error bar represents the standard deviation of the data and assuming a Gaussian statistical distribution of the data around the real model value (correct in approximation for Poisson with large count rates), the error bars tell us that 66% of the data points are within one errorbars of the physical model. However this also means that it is normal that *every third data point lies outside one errorbar* of the model.

Quite often a single point is remeasured with a new count number at a new monitor. The many data point measured at equal condition can be combined, if one imagines the measurement process hadn't stopped, but the point were measured in one go continuously, i.e. count numbers and monitor values should add

$$\binom{C_1}{M_1} \cup \binom{C_2}{M_2} \rightarrow \binom{C_1 + C_2}{M_1 + M_2} \rightarrow \frac{C_1 + C_2}{M_1 + M_2} \pm \frac{\sqrt{C_1 + C_2}}{M_1 + M_2}$$

and analogously for more points. One can see that after remeasuring data the errorbar of the scattering rate will improve. For example recounting a scan once more "doubles the statistics" and thus reduces the error $\sqrt{C}/M$ to $\sqrt{C}/M/\sqrt{2}$ by a factor $\sqrt{2}$.

Occasionally the difference between two data points measured at the same spot in Q and E, but at different temperatures T or magnetic fields B is of interest. In such a case the scattering rates can be subtracted to find this difference, however the error bars still add as taught for subtraction of Gaussian statistical data values.

$$\begin{pmatrix} C_1 \\ M_1 \end{pmatrix} - \begin{pmatrix} C_2 \\ M_2 \end{pmatrix} \rightarrow \left(\frac{C_1}{M_1} - \frac{C_2}{M_2} \right) \pm \sqrt{\frac{C_1}{M_1^2} + \frac{C_2}{M_2^2}}$$

Analysis of one full data scan All data scans have one parameter varying as the x value and the corresponding count number as the $I(x)$ value. Several analysis procedure are common apart from fitting a custom function to the data.

Q scan data with a Gaussian peak can be fitted to that peak added to a linear or quadric background. For example an incommensurate peak around 0.5 with a quadric background would be the function

$$I(H) = I_0 \cdot 2^{-\left(\frac{H-(0.5-\delta)}{\Delta}\right)^2} + I_0 \cdot 2^{-\left(\frac{H-(0.5+\delta)}{\Delta}\right)^2} + a(H-0.5)^2 + b(H-0.5) + c$$

Here the parameter Δ is the half width of the half maximum of the peaks and δ is the incommensurability. It is up to the experimenter to determine the order of the fitting variables to produce a converging fit. It is important to note that for

$$\delta < \Delta \sqrt{\frac{\ln 2}{2}} \approx 0.59\Delta$$

the incommensurate model function has a *flat-top* shape and does not show two separate maxima.

Another important quantity from the analysis is the Q integrated intensity of the data. It should be noted that this integration is performed in two or three Q dimensions, so that for example

$$I_{\text{int}} = \int \mathrm{d}^2 k I \propto I_{\max} \Delta_x \Delta_y$$

If an isotropic signal is assumed, then $I_{\text{int}} \propto I_{\max} \Delta^2$. The integrated intensity is thus best estimated with fits to data.

The extraction of a magnetic contribution can be done with scans at low temperature and high temperature scans where the magnetic correlation length is greatly reduced and the peak intensity is far below the background.

Instrumental resolution effect As the resolution manifests itself as a convolution of the data $I(k, E)$ with the resolution function $R(k, E)$,

$$I_{\text{data}}(\vec{k}, E) = \int_{\vec{k}', E'} I_{\text{phys}}(\vec{k}', E') R(\vec{k} - \vec{k}', E - E')$$

sharp physical features get smeared out. Usually the resolution function is approximated by a Gaussian resolution ellipsoid given by

$$R(\vec{k}' - \vec{k}, E - E') = R(\vec{k}, E) \exp\left(-\frac{1}{2} \begin{pmatrix} k_x & k_y & k_z & E \end{pmatrix} \mathbf{M} \begin{pmatrix} k_x \\ k_y \\ k_z \\ E \end{pmatrix} \right)$$

where the principal axes of the 4x4 resolution matrix **M** define the axes of the resolution ellipsoid.

In order to estimate the real Q or E width $\sigma_{Q,\text{physics}}$ and $\sigma_{E,\text{physics}}$ of a measured peak that is seemingly broad in the scan, be can use the equation

$$\sigma_{\text{data}} = \sqrt{\sigma^2_{\text{phys}} + \sigma^2_{\text{res}}}$$

i.e. widths roughly add in quadrature. This equation derives for the assumption that both measured data and the resolution function are a Gaussian as functions of $\vec{k}$ and E. The convolution reads

$$\begin{aligned} I_{\text{data}} &= \int_{-\infty}^{\infty} \exp\left(-\left(\frac{k' - k'_0}{\sigma_{\text{phys}}} \right)^2 \right) \exp\left(-\left(\frac{k - k'}{\sigma_{\text{res}}} \right)^2 \right) \mathrm{d}k' \\ &\propto \exp\left(-\left(\frac{k - k_0}{\sqrt{\sigma^2_{\text{phys}} + \sigma^2_{\text{res}}}} \right)^2 \right) \end{aligned}$$

Phenomenological interpretation of data Roughly speaking most neutron scattering measurements scan through well defined $\vec{k}$ and E configurations and yield a Gaussian peak in the count rate at some $\vec{k}$, E value of a defined width $\Delta\vec{k}$ and sometime a visible width ΔE.

$$C(\vec{k}) \propto 2^{-\left(\frac{(\vec{k}' - \vec{k})}{\Delta k/2} \right)^2}$$

As we know from quantum mechanics elementary particle are represented as waves $\psi \propto e^{-\mathrm{i}(\omega t - \vec{k}\cdot\vec{r})}$, we can recognize the link between momentum $\vec{k}$, energy E and space $\vec{r}$ and time t. For the elementary particle a momentum $\vec{k}$ corresponds to a *modulation in space* with spacing

$$\lambda = \frac{2\pi}{k} \tag{2.10}$$

and an *oscillation period in time* given by

$$T = \frac{2\pi}{\omega} \tag{2.11}$$

since then the wavefunction ψ repeats. The same we will assume for the quasi-particles that we measure with neutron scattering as long as a well-defined theory is not available.

Similarly to particles, we can obtain a velocity of the structure that we have detected in our measurements. For a single quasi-particle the velocity is

$$v = \frac{\omega}{k}$$

However for the total wavefunction usually there is a superposition of state with different $\vec{k}$.

$$\psi \propto \int A_{\vec{k}} e^{\mathrm{i}(\vec{k}\cdot\vec{r}-\omega(\vec{k})t)}$$

Note that we have included the momentum $\vec{k}$ dependence of the energy ω. If this superposition is peaked at $\vec{k}_0$, i.e. $A_{\vec{k}_0} \to \max$, then we can expand about this point

$$\begin{aligned}
\psi &\propto \sum A_{\vec{k}} e^{\mathrm{i}\left(\vec{k}\cdot\vec{r}-\omega(\vec{k})t\right)} \\
&\approx \sum A_{\vec{k}} e^{\mathrm{i}\left(\vec{k}\cdot\vec{r}-\left(\omega(\vec{k}_0)+\left.\frac{\partial\omega}{\partial\vec{k}}\right|_{\vec{k}_0}\cdot(\vec{k}-\vec{k}_0)\right)t\right)} \\
&= e^{\mathrm{i}(\vec{k}_0\cdot\vec{r}-\omega(\vec{k}_0)t)} \sum A_{\vec{k}} e^{\mathrm{i}\left((\vec{k}-\vec{k}_0)\cdot\vec{r}-\left(\left.\frac{\partial\omega}{\partial\vec{k}}\right|_{\vec{k}_0}\cdot(\vec{k}-\vec{k}_0)\right)t\right)}
\end{aligned}$$

from which we can see that this superposition, also called wave-packet, travels approximately at a speed

$$\vec{v}_g = \frac{\partial\omega}{\partial\vec{k}}$$

which is the *group velocity*. This is the phenomenological velocity our measured structure apparently travels at.

Finally the width $\Delta\vec{k}$ and ΔE of the measured signal can give us an estimate about the spacial size d and lifetime τ of the structure, if we assume that the spacial extension has *sharp boundaries*. The measured signal roughly corresponds to the square modulus of the Fourier transform of the real space picture. As a simple example calculation we assume we limited sinusoidal one-dimensional structure of dimension d:

$$f(x) = \begin{cases} \cos(kx) & \text{for } -\frac{d}{2} < x < \frac{d}{2} \\ 0 & \text{otherwise} \end{cases} \tag{2.12}$$

Its Fourier transform will be

$$\tilde{f}(k) \propto \frac{\sin\left(\frac{kd}{2}\right)}{k} + \frac{\sin\left(\frac{-kd}{2}\right)}{-k}$$

which corresponds to a experimental peaks of the form $\sin^2(x)/x^2$ and hence a half maximum at

$$kd \sim 2.8 \tag{2.13}$$

Similarly for a structure with a finite lifetime τ

$$\omega\tau \sim 2.8 \tag{2.14}$$

For correlation lengths ξ which are rather an exponential decay $\exp(-|x/\xi|)$, the estimation is

$$\Delta k\xi \sim 1$$

To sum up, our measurements will indicate a structure with

spacing periodicity	$\lambda = {}^{2\pi}/_{k}$	
correlation length	$\xi = {}^{1}/_{\Delta k}$	
spacial extension	$d = {}^{2.8}/_{\Delta k}$	$d \sim \dfrac{0.44a}{h}$
oscillation time	$T = {}^{2\pi}/_{\omega}$	
lifetime	$\tau = {}^{2.8}/_{\Delta\omega}$	
velocity	$v_g = \dfrac{\mathrm{d}\omega}{\mathrm{d}k}(k)$	

Correction of the data To extract quantitative comparisons between data under different scattering conditions, the count rate should be corrected for various contributions.

A general energy dependent correction is the monitor correction. The monitor that each data point is scaled to counts neutrons including the higher order neutrons that also get reflected by the monochromator. But the measured data point relate to the first order neutron only. Due to the Boltzmann distribution the ratio of first order to higher order neutrons is energy dependent. Also keeping in mind an energy-dependent monitor efficiency, neutron scattering data at different energies should be scaled by an appropriate factor to exclude these artifical energy dependence.

An L dependent correction is the bilayer correction. For odd excitations the bilayer factor $\sin^2(\pi L/3.4)$ (Eq. 2.5) can be divided out, since it represents only the correlations arising from the bilayer structure of the physics. However, prior to this the data the contribution originating solely from bilayer physics has to be extracted.

Finally, as physically the magnetic susceptibility is more meaningful, than the scattering function, it is sensible to extract the signal contribution belonging to quasiparticle processes (magnons, phonons) and divide out the energy and temperature dependent Bose factor (Eq. 2.9).

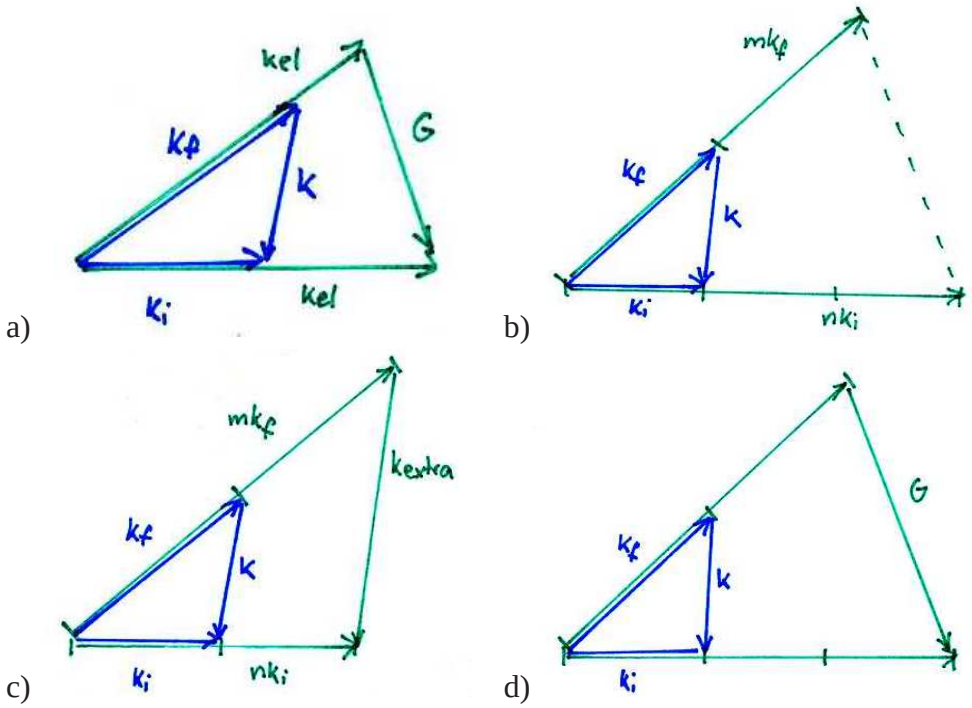

Figure 2.7: Spurious processes at the sample with intended scattering triangle (blue) and spurious process (green): a) incoherent mono./ana.; b) elastic incoherent sample; c) higher order sample; d) triple elastic

2.1.8 Spurious effects

Knowing and predicting spurious effect is essential to a technique that suffers quite often from these artefacts. Identifying them can save a lot of valuable beam time and confirm interpretation of data.

Any neutron that reaches the detector is counted, but as we saw, by the laws of physics only special ways are possible for a neutron to reach the detector. The apparent signal that is seen from spurious process is often called *spurion*. Let us consider which processes can lead to spurious counts being included in the counted scattering rate. Scattering processes in general can be elastic coherent scattering, inelastic coherent scattering and incoherent scattering, where the latter is direction independent and thus in principle always possible.

Spurious counts are only relevant if they are at least the same order of magnitude as the planned process. Elastic coherent scattering is the strongest, whereas incoherent and inelastic scattering are much weaker.

Spurions in elastic scans When doing elastic scans the “normal” process is

$$\text{reactor} \xrightarrow{k_f} \text{mono.(el.)} \xrightarrow{k_f} \text{crystal(el.)} \xrightarrow{k_f} \text{ana.(el.)} \xrightarrow{k_f} \text{detector}$$

An comparably strong process is higher order scattering

$$\text{reactor} \xrightarrow{nk_f} \text{mono.(el.)} \xrightarrow{nk_f} \text{crystal(el. } \vec{G}) \xrightarrow{nk_f} \text{ana.(el.)} \xrightarrow{nk_f} \text{detector}$$

From $n\vec{k}_i = \vec{G} + n\vec{k}_f$ one can see, that there is an apparent scattering at a nominal momentum transfer $\vec{G}/n = \vec{k}_i - \vec{k}_f$.

Spurions in inelastic scans A normal inelastic process is

$$\text{reactor} \xrightarrow{k_i} \text{mono.(el.)} \xrightarrow{k_i} \text{crystal(inel.)} \xrightarrow{k_f} \text{ana.(el.)} \xrightarrow{k_f} \text{detector}$$

In this chain the inelastic scattering is a weak process. Then spurious processes with also only one weak process can include

$$\text{inc.mono.}(k_{\text{el.}} = nk_f)\text{: reactor} \xrightarrow{k_{\text{el.}}} \text{mono.(inc.)} \xrightarrow{k_{\text{el.}}} \text{spur.(el.)} \xrightarrow{k_{\text{el.}}} \text{ana.(el.)} \xrightarrow{k_{\text{el.}}} \text{detector}$$

$$\text{inc.ana.}(k_{\text{el.}} = mk_i)\text{: reactor} \xrightarrow{k_{\text{el.}}} \text{mono.(el.)} \xrightarrow{k_{\text{el.}}} \text{spur.(el.)} \xrightarrow{k_{\text{el.}}} \text{ana.(inc.)} \xrightarrow{k_{\text{el.}}} \text{detector}$$

$$\text{inc.sample}(k_{\text{el.}} = nk_i = mk_f)\text{: reactor} \xrightarrow{nk_i} \text{mono.(el.)} \xrightarrow{nk_i} \text{crystal(el.inc.)} \xrightarrow{mk_f} \text{ana.(el.)} \xrightarrow{mk_f} \text{detector}$$

$$\text{higher order: reactor} \xrightarrow{nk_i} \text{mono.(el.)} \xrightarrow{nk_i} \text{crystal(inel.)} \xrightarrow{mk_f} \text{ana.(el.)} \xrightarrow{mk_f} \text{detector}$$

$$\text{triple el.}(k_{\text{el.}} = nk_i = mk_f)\text{: reactor} \xrightarrow{k_{\text{el.}}} \text{mono.(el.)} \xrightarrow{k_{\text{el.}}} \text{spur.(el.)} \xrightarrow{k_{\text{el.}}} \text{ana.(el.)} \xrightarrow{k_{\text{el.}}} \text{detector}$$

Note that incoherent scattering is where the given wavevector would not pass otherwise. The spurion scattering can be due to the crystal itself or due to contributions such as powder scattering from aluminum in the sample holder.

A spectrometer is usually set to a definite wave-vector transfer $\vec{k}$, energy transfer E and final wave-vector k_f ($k_i^2 = k_f^2 + E/2.072$).

$$\xrightarrow{k_i}\text{spur.}(\vec{k}) \xrightarrow{k_f} \qquad \vec{k}_i = \vec{k} + \vec{k}_f \qquad k_i^2 = \frac{E}{2.072} + k_f^2$$

Theoretically it is possible to predict what these value for spurious scattering would be. If the spurion originates from powder scattering at the sample, then only the magnitudes of the scattering vectors matter, which usually have much simpler equations. All resultant wave-vectors are supposed to lie in the scattering plane. In the following $\vec{A}_\perp$ will denote a vector perpendicular to $\vec{A}$ and in the scattering plane. It is most easily found by the cross-product with the scattering plane normal $\vec{A}_\perp = \vec{A} \times \vec{n}$.

Spurions in inelastic scans - incoherent mono./ana. case At the crystal the scattering is elastic with wave-vector transfer $\vec{G}$. The incoming and outgoing wave-vectors of the neutron still have the directions $\vec{k}_i^0$ and $\vec{k}_f^0$ of the normal scattering, but the magnitude $k_{\text{el.}}$.

$$\xrightarrow{k_{\text{el.}}}\text{spur.}(\text{el.},\vec{G}) \xrightarrow{k_{\text{el.}}} \qquad k_{\text{el.}} \cdot \vec{k}_i^0 = \vec{G} + k_{\text{el.}} \cdot \vec{k}_f^0$$

With the above equation it is possible to solve these vector equations for $\vec{k}$, i.e. the spectrometer setup where spurions are expected,

$$\vec{k}(\vec{G}, k_f, E, k_{\text{el.}}) = (k_i + k_f)\sin\theta \cdot \vec{G}^0 + (k_i - k_f)\cos\theta \cdot \vec{G}^0_\perp$$

$$k = \sqrt{k_i^2 + k_f^2 - 2k_i k_f \cos 2\theta} = \sqrt{(k_i - k_f)^2 + k_i k_f \frac{G^2}{{k_{\text{el.}}}^2}}$$

$$\sin\theta = \frac{G}{2k_{\text{el.}}}$$

or for $\vec{G}$, i.e. what the elastic wave-vector would have to be to give spurions in a given configuration.

$$\vec{G}(\vec{k}, k_f, E, k_{\text{el}}) = k_{\text{el}} \cdot \left\{(\sin\theta_i - \sin\theta_f)\vec{k}^0 \pm (\cos\theta_i - \cos\theta_f)\vec{k}^0_\perp\right\}$$

$$G = 2k_{\text{el}} \sin\frac{\theta_i - \theta_f}{2} = k_{\text{el}}\sqrt{\frac{k^2 - (k_i - k_f)^2}{k_i k_f}}$$

$$\sin\theta_i = \frac{k_i^2 - k_f^2 + k^2}{2k_i k}$$

$$\sin\theta_f = \frac{k_i^2 - k_f^2 - k^2}{2k_f k}$$

Depending on the order and case considered the elastic spurion scattering vector is

$$k_{\text{el.}} = nk_i \qquad \text{or} \qquad k_{\text{el.}} = mk_f$$

Easy incoherent mono./ana. spurion check Therefore the easiest way to check for spurions is to check precalculated values of $\vec{G}$ against

$$\frac{G}{n} = \sqrt{\frac{k_i}{k_f}(k^2 - (k_i - k_f)^2)} \qquad \text{or} \qquad \frac{G}{m} = \sqrt{\frac{k_f}{k_i}(k^2 - (k_i - k_f)^2)}$$

For Al or Si the magnitude of the scattering vectors are

$G(\text{Al}111) = 2.69\,\text{Å}^{-1}$ $\qquad$ $G(\text{Si}111) = 2.00\,\text{Å}^{-1}$

$G(\text{Al}200) = 3.10\,\text{Å}^{-1}$ $\qquad$ $G(\text{Si}220) = 3.27\,\text{Å}^{-1}$

$G(\text{Al}220) = 4.39\,\text{Å}^{-1}$ $\qquad$ $G(\text{Si}113) = 3.84\,\text{Å}^{-1}$

$G(\text{Si}400) = 4.63\,\text{Å}^{-1}$

$G(\text{Si}133) = 5.04\,\text{Å}^{-1}$

Note that Si is a monocrystal, so that usually the orientation of the crystal with respect to the Si is important.

Spurions in inelastic scans - elastic incoherent sample case

$$\xrightarrow{k_{\mathrm{el.}}}\text{spur.(el.inc.)}\xrightarrow{k_{\mathrm{el.}}} \qquad k_{\mathrm{el}} = nk_i = mk_f$$

This type of spurion will appear at the spectrometer set to energies

$$E = 2.072\left(\frac{m^2}{n^2} - 1\right)k_f^2$$

For example, when using $k_f = 2.662\,\mathrm{\AA}^{-1}$ the spurions would show up in energy scans at 18 meV ($3k_f = 2k_i$) and 44 meV ($2k_f = k_i$).

Spurions in inelastic scans - higher order case Higher order scattering at monochromator and analyser with normal coherent inelastic scattering at the sample is another possibility for unwanted neutrons to arrive at the detector.

$$\xrightarrow{nk_i}\text{spur.(inel.,}\vec{k}_{\mathrm{extra}})\xrightarrow{mk_f} \qquad n\vec{k}_i = \vec{k}_{\mathrm{extra}} + m\vec{k}_f \qquad (nk_i)^2 = \frac{E_{\mathrm{extra}}}{2.072} + (mk_f)^2$$

This process will occur if there is inelastic scattering from the sample at $\vec{k}_{\mathrm{extra}}$ E_{extra} for arbitrary reason.

$$\vec{k}_{\mathrm{extra}} = \vec{k}\frac{m+n}{2} + \frac{m-n}{2}\left(\vec{k}^0\frac{E}{k} + \vec{k}^0_{\perp}\sqrt{(2k_f^2) - \left(\frac{E}{k} - k\right)^2}\right)$$

$$E_{\mathrm{extra}} = 2.072\cdot(nk_i^2 - mk_f^2) = nE + 2.072k_f^2(n-m)$$

Spurions in elastic scans - triple elastic case A very strong spurious contribution arises if there is a chance of scattering a neutron $k_{\mathrm{el.}}$ elastically at all components, possibly with higher orders.

$$\xrightarrow{k_{\mathrm{el.}}}\text{spur.el.}(\vec{G})\xrightarrow{k_{\mathrm{el.}}} \qquad k_{\mathrm{el}}\vec{k}_i^0 = \vec{G} + k_{\mathrm{el}}\vec{k}_f^0 \qquad k_{\mathrm{el}} = nk_i = mk_f$$

With the elastic scattering at the crystal being associated with wave-vector transfer $\vec{G}$ one can find this type of spurion if the spectrometer is set to

$$\vec{k} = \vec{G}^0_{\perp}\sqrt{(mk_f)^2 - \frac{G^2}{4}\left(\frac{1}{m} - \frac{1}{n}\right)} + \vec{G}\frac{\frac{1}{m}+\frac{1}{n}}{2}$$

$$k = \sqrt{k_f^2\left(1 - \frac{m}{n}\right)^2 + \frac{G^2}{mn}}$$

$$E = 2.072\left(\frac{m^2}{n^2} - 1\right)k_f^2$$

Given k_f and the orders n,m, we see that there are predetermined energies at which one has to keep in mind the triple elastic spurion possibility.

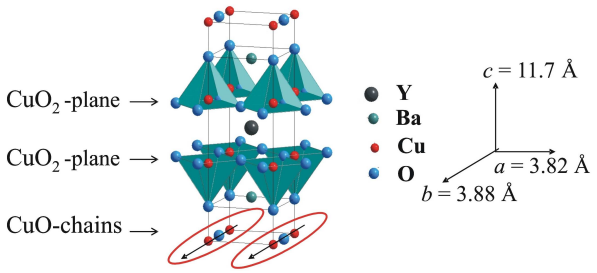

a)

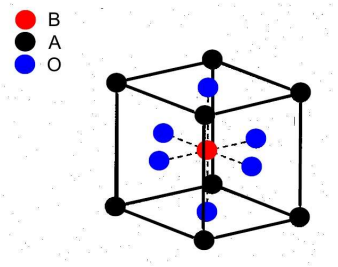

b)

Figure 2.8: a) Structure of the $YBa_2Cu_3O_x$ compound; b) General perovskite structure

Other artefacts Apart from higher order spurions and incoherent scattering, other artefacts that could appear in scans are

- air scattering, nitrogen condensation at 60 K
- helium scattering and condensation at 1.5 K
- stray neutrons from neighbouring spectrometers
- resolution ellipsoid streaks from nearby Bragg peaks

2.2 Crystal structure

The compound $YBa_2Cu_3O_x$ is a crystal with perovskite structure and a density of

$$\varrho(\text{YBCO}) = 6.8\,\text{g}\,\text{cm}^{-3}$$

It has a layered structure with two CuO_2-planes per unit cell separated by Y atoms. This bilayer is adjacent to CuO_δ chains layer with Ba atoms in between (Fig. 2.8). Therefore the stacking sequence is -BaO-CuO_2-Y-CuO_2-BaO-CuO_δ-.

This compound is non-stoichiometric in its oxygen content. The unit cell axes change with varying oxygen content. Data for the unit cell axes of $YBa_2Cu_3O_{7-\delta}$ are shown in Fig. 2.9 and additional data can be found in [Jor89, Kru97, Tak87, Cav87a]. At $x = 6.35$ the crystal undergoes a transition from the tetragonal structure $a = b$ to and orthorhombic structure $b > a$. *By definition* the longer axis is the b axis and this is also the axis along which the oxygen in the CuO-chain layers orders.

Oxygen order in CuO chains The oxygen in the CuO-chain layers tends to order in chains which defines the b axis of the unit cell. As a result, when for $x = 6.35$ the probability for chain formation increases, the unit cell undergoes a transition to orthorhombic symmetry. In $YBa_2Cu_3O_{6.5}$ the number of oxygen atoms is just right to create an alternation of completely filled and completely empty chains - an ideally ordered state which is called ortho-II state (Fig. 2.10). The ortho-II phase is especially stable and

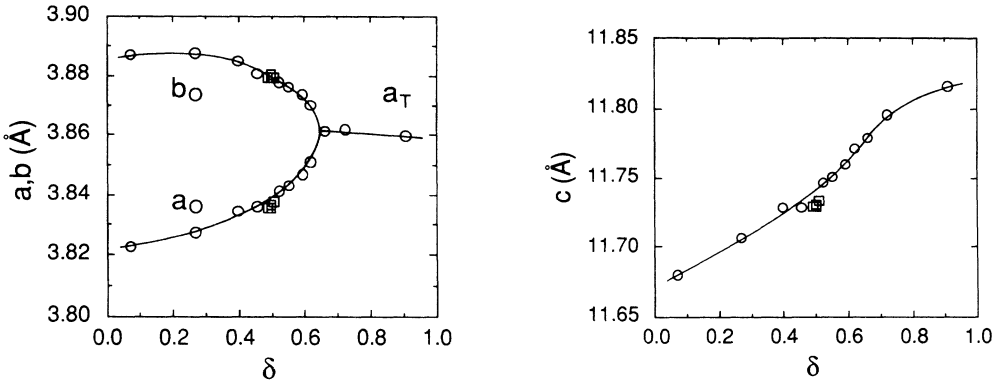

Figure 2.9: Unit cell axis of $YBa_2Cu_3O_{7-\delta}$ [Jor89]

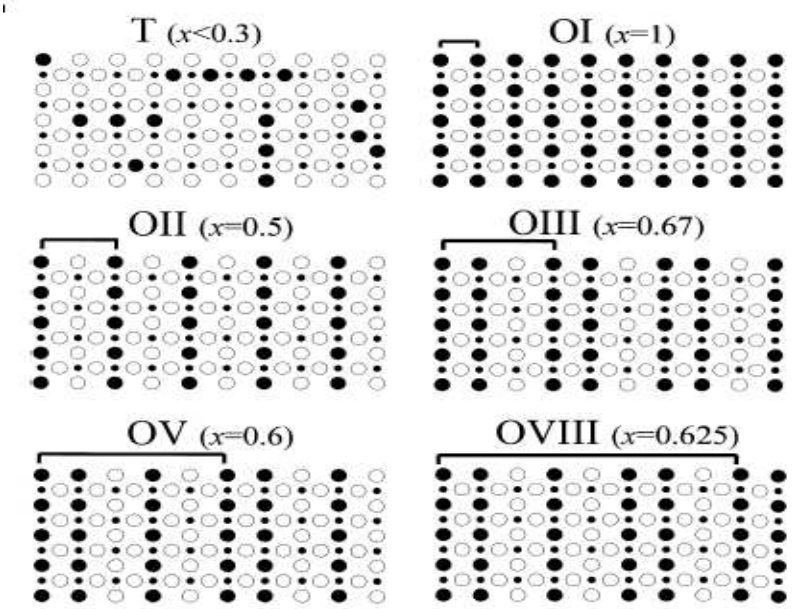

Figure 2.10: Oxygen order phases in CuO chain layer of $YBa_2Cu_3O_x$

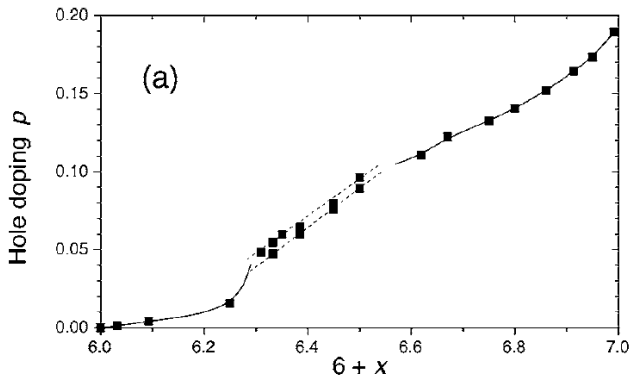

Figure 2.11: Dependence of hole doping p on oxygen content x in $YBa_2Cu_3O_x$ [Lia06]

exhibits the longest correlation length of all oxygen ordered-phases [And99a]. When all oxygen chain places are occupied, the phase is called ortho-I phased.

The chain order can depend on the preparation conditions and is crucial for the charge content in the CuO planes and consequently T_c. This effect is described in the next paragraph.

Charge content in CuO planes It is thought that the charge reservoir layers consisting of CuO chains induce hole carriers into the CuO_2-planes, however a CuO chain of at least Cu-O-Cu-O-Cu is needed to create a hole carrier [Zaa88]. This is the reason why hole carrier content and oxygen doping are not quite linear, but depend on average chain ordering. The relation is shown in Fig. 2.11. However a linear fit would yield [Tal95a]

$$p(x) = 0.187 - 0.21(1 - x)$$

It is difficult to determine the exact charge doping level of a given $YBa_2Cu_3O_x$ sample for reasons summarized in [Tal95a, Lia06]. However, it is possible to find estimates from literature data and parameters like the c-axis length or T_c. The relation between the hole carrier concentration p and the c-axis at room temperature was found to be

$$p(c) = 11.491y(c) + 5.17 \cdot 10^9 y(c)^6 \qquad y(c) = 1 - \frac{c}{11.844\,\text{Å}}$$

A universal relation in all cuprates between T_c and the hole carriers is approximately [Pre91, Tal95a]

$$\frac{T_c}{T_{c,\max}} = 1 - 82.6(p - 0.16)^2$$

2.2.1 Magnetic susceptibility as function of temperature

The critical temperature T_c of $YBa_2Cu_3O_x$ as a function of oxygen doping shows a dome-like structure with an superconductivity onset at $x \approx 6.35$, a plateaux at $x =$

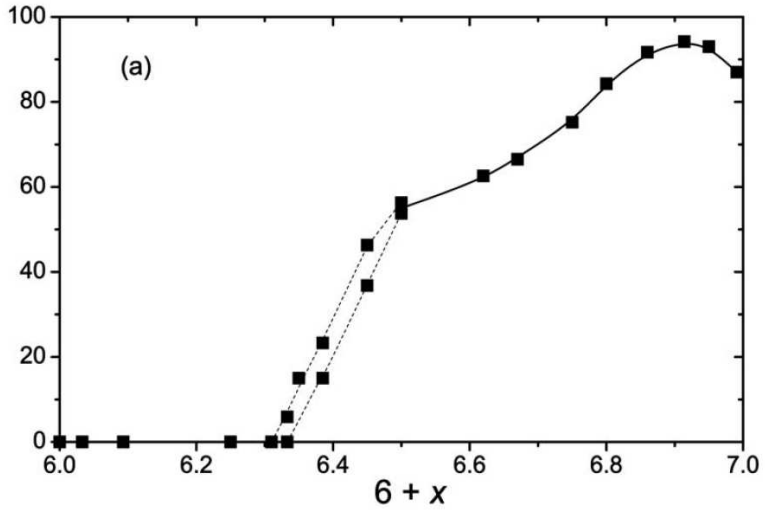

Figure 2.12: Superconducting critical temperature T_c of $YBa_2Cu_3O_x$ [Lia06]

6.6, a maximum at $x = 6.93$ and a decrease of T_c at high doping up to the highest possible $x = 7.0$ (Fig. 2.12). The data scatters slightly and other data can be found in [Lia06, Jor89, Lib93].

2.3 Previous neutron scattering data

2.3.1 Undoped parent compound

The parent compound $YBa_2Cu_3O_{6.0}$ is an antiferromagnetic insulator with 3D Néel order and magnetic moments parallel to the CuO_2-planes. The antiferromagnetic coupling constant in the CuO_2-plane is $J_{\parallel} = 106\,\text{meV}$. The inter-plane coupling $J_{\perp}$ is nearly four orders of magnitude lower and the intra-bilayer coupling $J_{=}$ along c is about 11 meV (reference in [Tra05]) The spin waves are well described by the Heisenberg model. It is interesting to note, that out-of-plane spin excitations exhibit a 5 meV anisotropy gap, whereas the in-plane magnons are gapless.

Upon charge doping the antiferromagnetic order is destroyed and a universal spin excitation spectrum is found in various cuprates. Detailed reviews of the spin excitation spectrum in cuprates are given in [Tra05, Bou98, Bir06, Fur98]

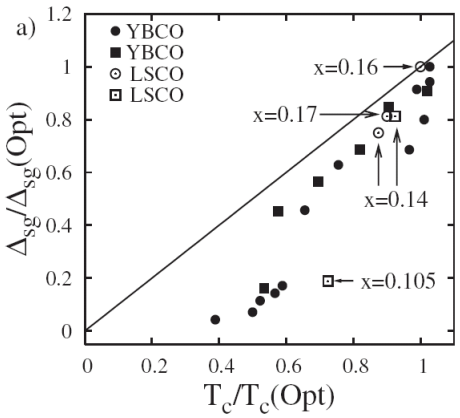

Figure 2.13: Scaling between spin gap Δ_{SG} and T_c [Cha07a]

2.3.2 Spin-gap

In the metallic state of $YBa_2Cu_3O_x$ an energy gap in χ'' can be found, i.e. at low temperatures below at certain energy E_{SG} the intensity is greatly reduced.

$$\chi''(Q_{AF}, T < T_c) \begin{cases} \approx 0 & E < E_{SG} \\ > 0 & E_{SG} < E \end{cases}$$

In the heavily doped region $0.65 < x < 0.94$ this spin gap is roughly proportional to the critical temperature (Fig. 2.13)

$$E_{SG} \approx 3.4 k_B T_c \qquad (0.65 < x < 0.94)$$

thus the spin gap in optimally doped $YBa_2Cu_3O_x$ is about 33 meV. In the weakly doped region where a spin gap can still be detected $x = 0.4 \ldots 0.65$ it drops rapidly with T_c and is smaller than this linear relation.

The energy of the spin gap does not seem to change with increasing temperature, but with increasing temperature magnetic scattering appears inside the gap with a complete filling at a temperature $T^*_{INS} > T_c$.

2.3.3 Hour-glass dispersion in cuprates

An hour-glass-like dispersion of the magnetic excitation was found in optimally doped $YBa_2Cu_3O_x$, moderately underdoped $YBa_2Cu_3O_x$ [Hay04], moderately underdoped $La_{2-x}Sr_xCuO_4$ [Tra04b] and optimally doped $La_{2-x}Sr_xCuO_4$ [Vig07] (Fig. 2.14). Therefore the *local peak intensities in K scans* yields an hour-glass shape when plotted in an *E-K* graph (Fig. 2.14). In $YBa_2Cu_3O_x$ the neck of the hour-glass shaped is the energy of the maximum intensity and has been termed “resonant mode” (see section 2.3.4). In contrast to that, in $La_{2-x}Sr_xCuO_4$ the maximum integrated intensity is at 18 meV, where the signal is still incommensurate.

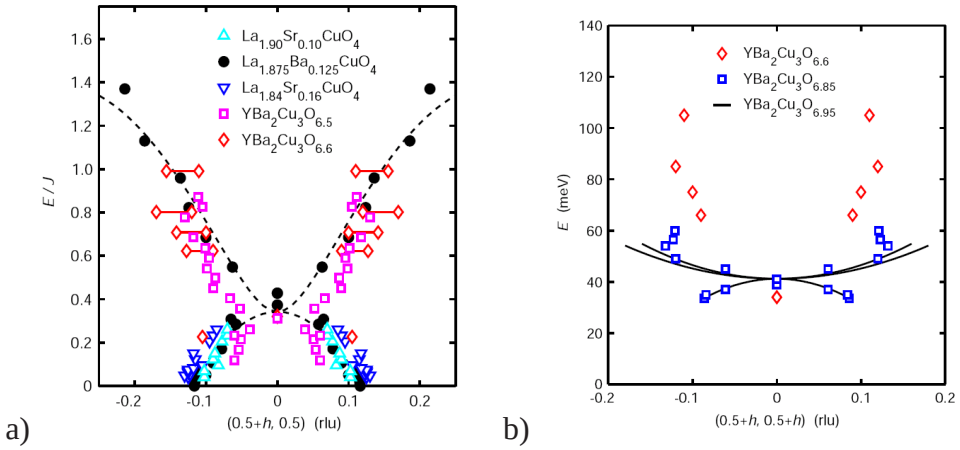

Figure 2.14: Maximum scattering intensity for cuprates: a) underdoped cuprates; b) close to optimally doped cuprates

As the pure sample is heated above the transition temperature T_c into the normal state, the hour-glass dispersion become a Y-shaped dispersion. At energies below 30 meV the single peak has a flat-top Gaussian shape and can be fitted with Gaussians off-centred by the incommensurability $H \pm \delta$. This δ corresponds the the sample peak separation that is found in our Zn doped samples at low energies.

In more underdoped $YBa_2Cu_3O_x$ the low-energy response displays signs of incommensurate peaks at low energies $E \sim 24$ meV and low temperatures: $x = 0.6$ [Dai98, Moo98], $x = 0.7$ [Ara99], $x = 0.85$ [Bou00]. The incommensurability increases with increasing doping level p.

2.3.4 Resonance mode

The spin excitation spectrum of optimally doped $YBa_2Cu_3O_{6.93}$ manifests itself as a sharp Gaussian shaped peak at a specific energy $E_R = 38$ meV, with FWHM $\Delta q \sim 0.2$ and a sharp drop in intensity when increasing the temperature above T_c [Fon95] (Fig. 2.15).

$$\chi''(Q_{\mathrm{AF}}) \begin{cases} = \delta(E - E_R) & T < T_c \\ \approx 0 & \text{otherwise} \end{cases}$$

The E width is hardly larger than the instrumental resolution yielding an intrinsic energy width of the resonance of $\Delta E < 3$ meV [Reg94, Fon95]. The magnitude of the spin fluctuations left in the normal state is at most $70\mu_B^2\,\mathrm{eV}^{-1}$ [Fon95, Fon96].

The dependence of the signal along L in k-space follows from the fact that the compound $YBa_2Cu_3O_x$ has a CuO_2-bilayer structure (section 2.5). Theoretical considerations predict that there will be a so-called odd contribution with a dependence $I \propto \sin^2(L/3.4)$ and even contribution with a dependence $I \propto \cos^2(L/3.4)$ [RM91, Moo93, Reg94, Fon95, Bou96, Fon96, Hay96]. Due to specific spin correlations among

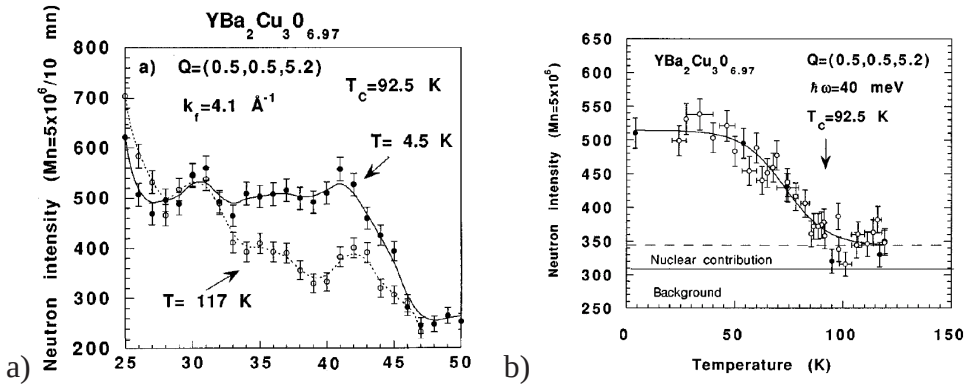

Figure 2.15: Resonance mode in $YBa_2Cu_3O_{6.97}$ at 39 meV; Disappearance of resonance in normal state seen in a) energy dependence; b) temperature dependence [Bou96]

the bilayer planes, the resonance manifests itself most clearly in the odd excitations, which peak at $L = 1.7$ or a bit weaker at $L = 5.4$. For this reason most data presented here is at the antiferromagnetic wave-vector position with the stated L component: (0.5,0.5,1.7).

The even mode resonance at $L = 3.4$ was discovered much later than the odd mode resonance. It is found at higher energies and is weaker than the odd mode resonance [Pai06].

The absolute weight of the resonance remains approximately constant [Dai99, Fon99b] with doping however the energy shifts roughly according to [Bou98, Fon99b, He05]

$$E_R \sim 5k_BT_c$$

The resonance feature has also been detected in $Bi_2Sr_2CaCu_2O_x$ [Fon99c, Mes00, He01] and $Tl_2Ba_2CuO_{6+\delta}$ [He02]. However, in $La_{2-x}Sr_xCuO_4$ no strong temperature dependent excitation at Q_{AF} was observed. In contrast to all other cuprate compounds, $La_{2-x}Sr_xCuO_4$ is dominated by the low-energy dispersive excitations.

Several models have been suggested to account for the magnetic resonance feature in cuprates: band structure singularities [Bul96, Abr98], antiferromagnetic interactions [Liu95, Onu95a, Mil96] and interlayer tunneling [Yin97]. These models start from the band picture of electron, however other suggestions have been made to describe the resonance as spin-wave-like excitations of localized electrons, akin to those observed in the insulating parent compound. [Dem95, Zha97, Zha96, Mor98, Ass97].

2.4 Sample preparation and mounting for neutron spectrometers

2.4.1 Crystal growth

A growth procedure giving high quality crystals has been described in [Erb96, Lia98, Lia92]. With the flux growth method a well defined amount of basis powders are thoroughly mixed together and placed in a furnace.

To produce pure $YBa_2Cu_3O_x$, a mix of 99.0g $BaCO_3$, 97.8g CuO, 3.17g Y_2O_3 was used and treat with a furnace temperature evolution set to

$$20\,°\text{C} \xrightarrow{300\,\text{K}/h} 1050\,°\text{C}(6h) \xrightarrow{30\,\text{K}/h} 976\,°\text{C}(2h) \xrightarrow{0.2\,\text{K}/h} 968\,°\text{C} \xrightarrow{0.1\,\text{K}/h} 964\,°\text{C} \rightarrow \text{decant}$$

This procedure is very sensitive to even a few degrees deviation and therefore the precise set temperatures have to be calibrated for every furnace. The procedure yields crystals with typical dimensions ~4mm.

2.4.2 Annealing and effect on chain oxygen

Since $YBa_2Cu_3O_x$ has a variable oxygen stoichiometry, a heat treatment in an atmosphere containing specific amounts of oxygen can modify the oxygen content in the material - a process which is called annealing. By in-diffusion or out-diffusion the oxygen content of the CuO-chains can be adjusted. In-diffusion is slower than out-diffusion [Lag93] and also depends on oxygen content The two variables to be decided on are partial pressure of oxygen in the annealing atmosphere and the temperature.

In principle there are different parameter sets possible to achieve the same final oxygen content, but annealing below 600 °C significantly slows down the out-diffusion (several days) [Lag93] (i.e. surface reaction limited). On the other hand it should be noted that $YBa_2Cu_3O_x$ decomposes at 900 °C. A theoretical fitted curve which describes the relation between oxygen content x in $YBa_2Cu_3O_x$ and the annealing oxygen partial pressure p_{O_2} and annealing temperature T is given by [Hon91, Equ.6]

$$\frac{x(x-6)^2}{1-(x-6)} = 3.594 \cdot 10^{-4} \cdot e^{9631\text{K}/T} \sqrt{p_{\text{O}_2}\text{bar}^{-1}}$$

An experimental curve for the dependence of final oxygen content on oxygen partial pressure and temperature is shown in Fig. 2.16. For the required annealing times one is on the safe side with one week of annealing.

After such a treatment the crystals should be quenched - for example by dropping them into liquid nitrogen. This is to stop the in/out-diffusion process abruptly, since if the sample is cooled down slowly, in that constant environment, an undesired oxygen concentration will set in - at least on the surface of the samples.

An easy way to check to oxygen content after annealing is measuring the c-axis with x-ray diffraction or neutron scattering and comparing to literature values (Fig.

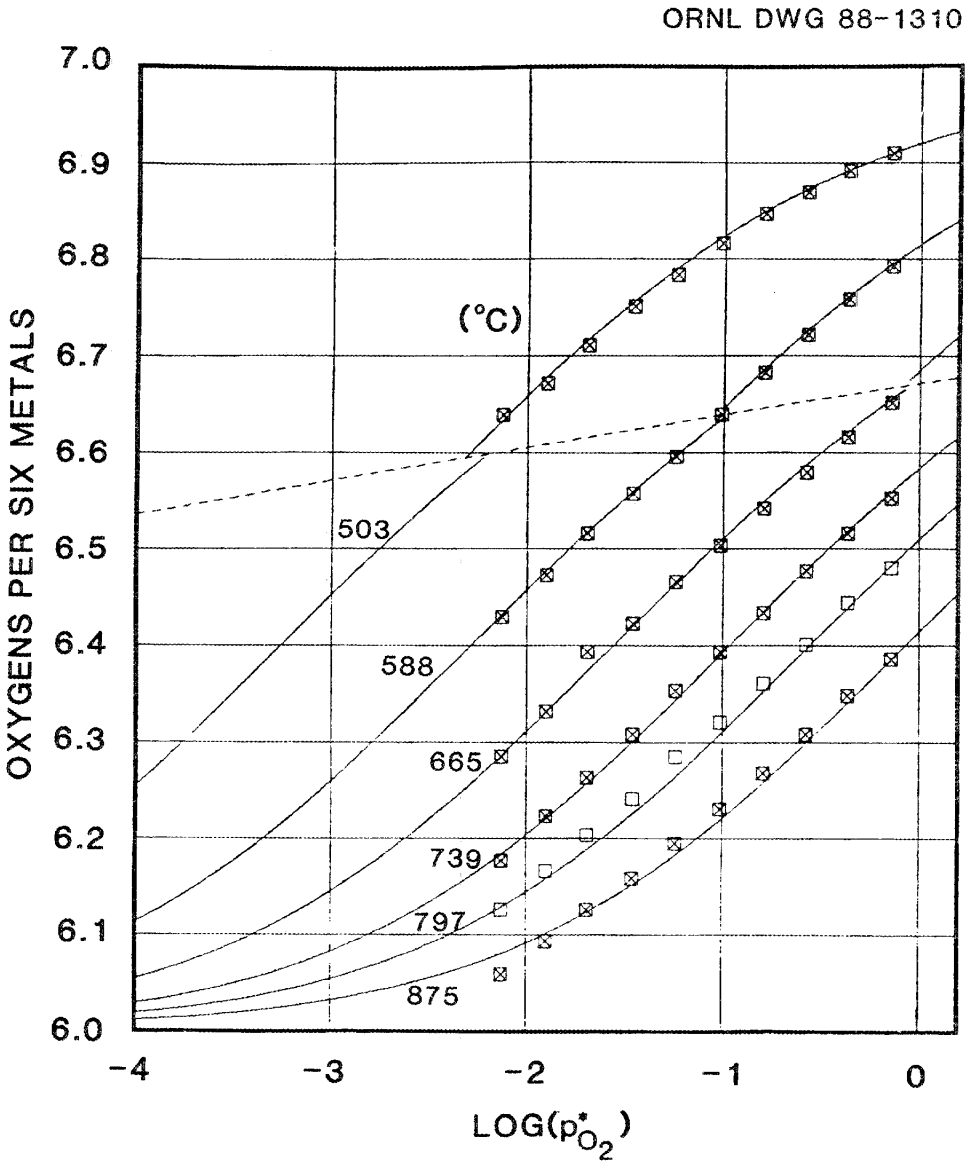

Figure 2.16: Relation between annealing oxygen partial pressure, temperature and equilibrium oxygen content in $YBa_2Cu_3O_x$ [Spe88]

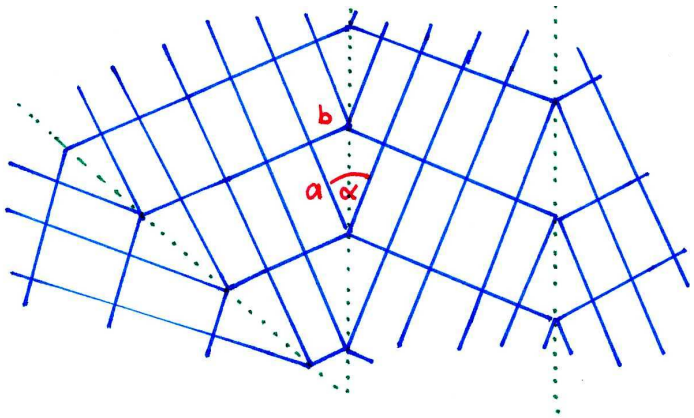

Figure 2.17: Twin domain formation for orthorhombic crystals

2.9). Another way to measure the charge carrier content directly is by measuring the thermopower at room temperature. The relation to the charge content is described in [Tal97, Tal95a, Tal95b, Obe92].

2.4.3 Postanneal chain ordering

The oxygen in the CuO-chains will order into chain fragments, which in turn induce hole charges in the CuO_2-planes. Single oxygen atoms do not induce these charge, so oxygen chain order is essential[Uim92]. It is possible that after quenching the oxygen is partially disordered and has not completely formed oxygen chains yet. Then leaving the crystals at room temperature for a day will result in additional oxygen chain formation, so that for underdoped crystals the T_c can rise by 10 K. Relaxation times of the critical temperature were measured and turned out to be $\sim$ 10h.

2.4.4 Detwinning

The crystals $YBa_2Cu_3O_x$ show an orthorhombic phase for $x \geq 6.35$, i.e. the a-axis and the *b*-axis have different lengths as can be seen in Fig. 2.9. As usual for such kind of crystals, they exhibit so called twin-domains, i.e. during the growth process the a-axis and the b-axis can switch as shown in Fig. 2.17. Note that the angle between the crystal axes in the domains is not exactly 90°, but

$$\alpha = 2 \arctan \frac{a}{b}$$

which is approximately $\alpha_{6.93} = 88.2°$ for optimally doped $YBa_2Cu_3O_{6.93}$.

For anisotropic features that order along a certain direction in the crystal only, the bulk technique neutron scattering will superimpose in the measured spectrum. To be enable to distinguish between a-axis and b-axis contributions, the crystals have to be detwinned. This can be done with a thermomechanical process called detwinning ,

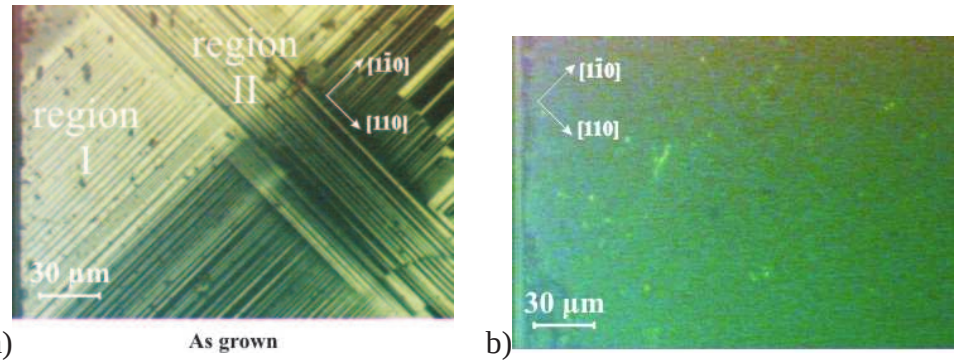

a) As grown b)

Figure 2.18: Crystal as seen in polarized light microscope: a) before detwinning; b) after detwinning

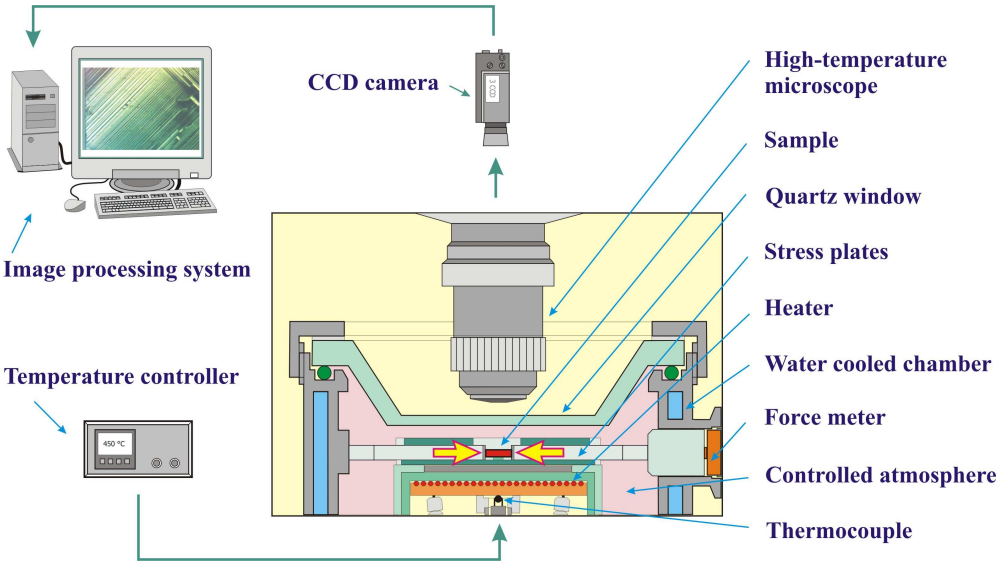

Figure 2.19: Detwinning apparatus

where uniaxial pressure is exerted on the crystal under high activation temperatures, so that domains start to flip to reduce that total energy by aligning the shorter axis in the direction of the uniaxial pressure. A possible apparatus is shown in Fig. 2.19.

For the crystals in this work a pressure of 50 MPa was used with a temperature of 550 °C and the detwinning was performed for 2 hours on each crystal. Various other conditions have been used in other works and suggestions can be found in [Sch89, Wel89, Vil96, Kai89, Pyk93, Mei91, Lia02, Ric91, Vor93]. Calculations and measurements for detwinning speed can be found in [Kis89, Cav87b]. For detwinning models see the reference in [VT90].

To check for detwinning polarized visible light spectroscopy is useful. With specifically adjusted polarisers, the twin domain can be seen as light and dark regions (Fig. 2.18).

If heat is again applied *retwinning* of the sample can occur. This can happen at $T > 130\,°C$.

The twinning can be checked with neutron scattering, where two Bragg peaks of the different domains can be seen next to each other. Their positions are related to the ratio of the crystals axes and their intensity ratio corresponds the domain ratio.

2.4.5 Crystal care

After the growth crystals have been extracted, they are still susceptible to various environmental influences if not treated correctly. It is important to avoid humidity to avoid contamination [Zha94, Zhu95], but aceton and ethanol do no harm however [Bar87]. In general it was found that water vapor and CO_2 can degrade $YBa_2Cu_3O_x$ so exposure to air should be minimized and sample should be kept in desiccators whenever possible.

2.4.6 Coalignment of crystals

In order to obtain a sufficient sample volume for neutron scattering small single crystals have to be coaligned, to yield a large effective sample with crystal axes oriented the same way. To achieve this, the crystals were in turn glued on a silicon plate (Fig. 2.20). Checks with a Laue back-scattering setup for orientation were performed while the glue had not dried, and misorientations above 1° were corrected immediately. Both sides of the silicon plate were used and two layers of crystals gave maximum density in order to fit as much mass a possible into the neutron beam.

2.4.7 Sample orientation for triple axis experiments

Antiferromagnetic magnetic excitation are naturally measured at antiferromagnetic wavevectors

$$Q_{\mathrm{AF}} = (0.5 + n, 0.5 + m, L) \qquad n, m \in \mathbb{Z} \tag{2.15}$$

Figure 2.20: Sample with crystals in aluminum plate mounted on a multi-goniometer holder

Bragg	200	001	013	113	110	006	100	008	011	002
Intensity	1000	426	414	313	205	174	158	135	56	9

Table 2.1: Bragg peak intensities of selected positions as found with ICSD online

As there is some correlation between the CuO_2-plane-bilayer the intensity is modulated by the bilayer modulation with a maximum at $L = 1.7$. Therefore candidates for our measurements are (0.5,0.5,1.7) and (0.5,1.5,1.7). As due to Cu form factor the intensity decreases with increasing $|Q|$, at the points (1.5,1.5,1.7) and beyond the signal would be too weak.

When aligning the sample on the Bragg peaks, it is a useful information to know their scattering intensities which are shown in table 2.1 Several important point are notable. (100) is weak and thus (200) is preferable for orientation. (011) is also quite weak making the orientation on (H, K, K) delicate. (113) is comparably strong, which has to be kept in mind as it can contribute as a second order process when measuring close to (0.5,0.5,1.5).

The 2θ angle that is critical to consider in order to avoid wall crashes of the instrument, depends on the incident wavelength and magnitude of the Bragg peak wavevector.

$$2k_i \sin\theta = |Q|$$

Alternative Bragg peaks could be used if some configurations are infeasible or a higher precision on the measurements is required.

Another constraint is the requirement of satisfying the scattering conditions. Con-

sequently the highest transfer energy possible is limited by

$$E < 2.072\,\mathrm{meV\,\AA}^2 \cdot k(k + 2k_f)$$

For this reason low k and high E can only be attained with large k_f.

Chapter 3

Effect of Zn impurities on magnetic excitation spectrum of $YBa_2Cu_3O_x$

Impurities provide one way of slightly perturbing the physics in order to induce changes that can be interpreted with physical ideas or be compared to theoretical predictions. Theory can treat such impurities as perturbations and predict possible outcomes of spectroscopy experiments. This way constraints exclude certain directions for theories.

Various impurities are possible which differ in the impurity electron structure and the doping destination in the cuprate crystal. Apart from intrinsic impurities which come from imperfections or intentional electron radiation, external impurities can be introduced by doping with additional atoms. Provided impurities substitute for Cu due to similar atomic size, two different Cu sites are possible in $YBa_2Cu_3O_x$. When impurities go to the chain Cu sites, they alter the doping effects of those to the impurity's different valence. On the other hand, a more interesting case is when impurity atoms substitute for Cu in the CuO_2-planes, as then they reside right at the place where superconductivity is thought to originate. The most prominent examples for such impurities are Zn, Ni and Li. The main differences in these impurities is their effective influence on local magnetism and charge in the CuO_2-planes. Since the valence and spin state of copper substituting impurities can be different from copper, the impurities will locally alter the spin or charge balance. In particular:

- Zn^{2+}: spin-less, no charge induced due to large binding energy
- Ni^{2+}: effective spin 1 at the impurity site, no charge induced
- Li^{+}: spin-less, itinerant charge induced due to low binding energy

The behaviour of other dopants can be found in [Wei91, And91]

Experimentally the effect of these impurities often turns out to be similar with the difference that Zn shows much stronger effects than Ni. For superconductivity directly, the effect of even a small amount of Zn impurities actually does produce significant changes. In the following I will describe the preparation, characterization of

$YBa_2(Cu_{1-y}Zn_y)_3O_x$ crystals and finally present the measured neutron scattering data on the samples and the relation to other experimental techniques.

3.1 Preparation of $YBa_2(Cu_{0.98}Zn_{0.02})_3O_x$

Growth Impurities are added by mixing suitable compounds among the initial substances for crystal preparation and then adjusting the temperature evolution of the furnace according in order for relatively large crystals containing the impurity atom to form. However, experimentally it has been found that Zn impurities do not substitute beyond 5% per Cu [Tak88, Xia88a, Zag95, Lan94a]. If more Zn is provided during crystal growth, the green phase Y_2BaCuO_5 is formed and some Zn left untouched.

In short, after mixing 99.21g $BaCO_3$, 89.90g CuO, 3.00g $YO_{1.5}$ and 2.88g ZnO, single crystals of $YBa_2(Cu_{1-y}Zn_y)_3O_x$ were grown by the flux method with Ba-Cu-O as the flux. The furnace temperature evolution is given by

$$20\,°C \xrightarrow{300\,K/h} 1020\,°C(4h) \xrightarrow{30\,K/h} 976\,°C(2h) \xrightarrow{0.2\,K/h} 970\,°C \xrightarrow{0.1\,K/h} 962\,°C \rightarrow \text{decant}$$

and free standing crystals with dimensions of the order of 4 mm were obtained after decanting [Lin92]. This procedure is very sensitive to even a few degrees deviation and therefore the precise furnace set temperatures might be furnace dependent, as there is never a perfect equality between set and real temperature.

Annealing As-grown crystals do not have a well defined oxygen content, since during the heating process oxygen is free to move in and out the crystals dependence on temperature and pressure (here ambient pressure) (see section 2.4.2). Therefore an additional temperature treatment is necessary to adjust the oxygen content x of the $YBa_2(Cu_{1-y}Zn_y)_3O_x$ sample to the final value. It turns out that Zn does not alter the annealing parameters that apply for the pure compounds and the results from section 2.4.2 apply correctly. In this work 560 °C and ambient pressure for a gas of 20% oxygen in argon was used to get underdoped $x = 6.6$ crystals. To get underdoped $x = 6.45$ crystals 580 °C and ambient pressure for a gas of 0.5% oxygen in argon was used.

The reason for using $x = 6.6$ is that at this doping the intrinsic disorder in the compound is minimal [Cav87a]. The other oxygen doping level $x = 6.45$ makes the Zn doped $YBa_2(Cu_{0.98}Zn_{0.02})_3O_{6.45}$ have $T_c \sim 0$, i.e. making the low temperature state close to the superconducting transition.

Detwinning Just as the pure $YBa_2Cu_3O_x$, the underdoped crystals in this experiment have different length a and b axis and therefore come out twinned. Therefore crystals with irregular shape are cut into cuboids in order to be detwinned. Thermomechanical detwinning can flip twin domains to produce single domain crystals with a unique direction of the a axis. This procedure is unchanged from what is described for the pure crystals in section 2.4.4.

Aligning Once a considerable total mass of detwinned crystals is available, the crystals are aligned to a batch for neutron scattering experiments. This was described briefly in section 2.4.5. For this experiment the $YBa_2(Cu_{0.98}Zn_{0.02})_3O_{6.6}$ sample had 650 mg of crystals mounted on an aluminum plate and the $YBa_2(Cu_{0.98}Zn_{0.02})_3O_{6.45}$ sample had 1100 mg of crystaled mounted on a 600 mg silicon plate.

3.2 Characterization of the crystals

Zn content The Zn content was measured with EDX and ICP (inductively coupled plasma) independently. The EDX analysis employs electron irradiation or x-rays to excite the atoms of the substance and measures the emission spectrum at given positions on the crystal. For such a small amount of Zn impurities the intensity of the small Zn peaks in the spectrum is difficult to judge and analyze and therefore the EDX measurement gives results with considerably large error bars attached. Nevertheless the results $(2 \pm 0.3)\%$ are in agreement with the expectations.

More sensitive is the ICP technique, which however is destructive and requires a sufficient amount of material to analyze. These kind of measurements have been performed and confirmed a Zn concentration of 2% per Cu.

Therefore a total Zn content of 2% Zn per Cu was confirmed in accordance with the initial weight of the source materials.

Average separation of Zn atoms This Zn content can be converted to an estimate for the average distance d_{Zn} between Zn atoms in the CuO_2-planes. First we need to find the Zn occupation in the CuO_2-planes. Two of three Cu atoms in the units cell are in the planes and a total Zn concentration of y corresponds to $1.5y$ Zn per plane-Cu atom. Assuming that in the planes each Zn occupies a square of size d_{Zn}^2, it turns out that

$$d_{Zn} = \frac{1}{\sqrt{1.5y}} a$$

Therefore for $y = 2\%$ we find

$$d_{Zn} = 5.8a$$

given in lattice parameters.

Superconducting transition temperature Another useful and easy to measure property is the superconducting onset transition temperature T_c seen in the diamagnetic transition of the magnetization. Using a the ready made PPMS measurement setup made by "Quantum Design", the magnetization has been measured.

One can see that $YBa_2(Cu_{0.98}Zn_{0.02})_3O_{6.6}$ has a transition temperature of $T_c = 30\,\mathrm{K}$ (Fig. 3.1), which is roughly the same as the literature predictions for $x = 6.6$ and

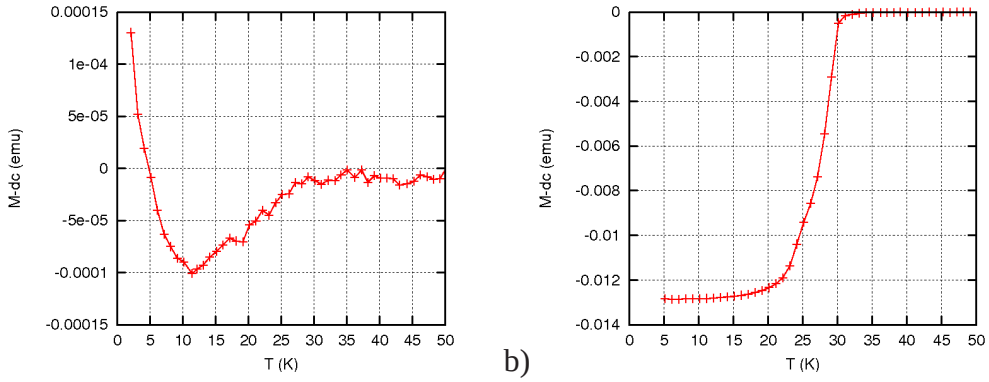

Figure 3.1: Magnetic susceptibility of a crystal of a) $YBa_2(Cu_{0.98}Zn_{0.02})_3O_{6.45}$; b) $YBa_2(Cu_{0.98}Zn_{0.02})_3O_{6.6}$

sample	mass	annealing	twin domain ratio	T_c
$YBa_2(Cu_{0.98}Zn_{0.02})_3O_{6.45}$	1500mg	580 °C, 0.5% O_2	1:13	~ 0 K
$YBa_2(Cu_{0.98}Zn_{0.02})_3O_{6.6}$	650mg	560 °C, 20% O_2	1:4	~ 30 K

Table 3.1: Properties of the samples used for the neutron scattering experiments

$y = 2\%$ (eq. 3.2). The transition is relatively sharp $\Delta T \sim 7$ K keeping in mind that more underdoped cuprates usually have broader transitions [Moo02].

The $YBa_2(Cu_{0.98}Zn_{0.02})_3O_{6.45}$ sample does not show a superconducting transition into the diamagnetic state. The prediction from literature references would be $T_c \sim 0$ K (Fig. 3.1) and therefore this result is not unexpected. Note that as the crystals have all similar dimensions, the signal for the more underdoped sample is two orders of magnitude smaller than the superconducting sample. We see that the special property of the latter sample is, that it is chemically very close to the onset of superconductivity at low temperatures. Actually it is possible to perform AC magnetization measurements, in which case the imaginary part of the magnetization shows an upturn at very low temperatures and seems to peak at ~ 0 K. The susceptibility shows an upturn at temperatures below 10 K. This behaviour could be due to a paramagnetic moment, which is what is also observed in NMR measurements as will be described later.

Detwinning ratio The quality of the detwinning can be checked by performing neutron scattering scans of the Bragg peaks and finding the ratio between the main peak and the shoulder coming from the minority twin-domain. With known lattice parameters the positions of the peaks can be checked for consistency.

With this method the twin domain ratio was found to be 1:4 for $YBa_2(Cu_{0.98}Zn_{0.02})_3O_{6.6}$ and 1:13 for $YBa_2(Cu_{0.98}Zn_{0.02})_3O_{6.45}$.

3.3 Effect of Zn on the crystal structure and the superconducting phase

In this section the effects of Zn impurities on superconductivity and magnetism, which are most important for the understanding of the following neutron data, are described. Additional experiments relevant for the interpretation are described in a later section.

Unaffected crystal structure of Zn in Cu-planes Zn impurities in $YBa_2Cu_3O_x$ are known to substitute for the Cu atoms in the CuO_2-planes [Xia88b, Mae89], and they do not modify the doping level substantially [All91]. Therefore they are expected to directly influence the superconductivity which originates from the CuO_2-planes and at the same time they do not influence lattice parameters or oxygen doping in the Cu chains. This make interpretation of results free from doubts about changes in the crystal structure.

Suppression of T_c Zinc is an impurity that suppresses superconductivity in $YBa_2Cu_3O_x$, in particular T_c, stronger than most other impurities. Surprisingly the suppression is linear to the doping amount, i.e. the $T_c(y, x)$ reduction in $YBa_2(Cu_{1-y}Zn_y)_3O_x$ is [Zag95, Chi91, Bon94, Fuk96b]

$$T_c(y, 7.0) = T_c(0, 7.0) - 8.8\,\mathrm{K} \cdot y/\% \tag{3.1}$$

$$T_c(y, 6.6) = T_c(0, 6.6) - 20\,\mathrm{K} \cdot y/\% \tag{3.2}$$

Interestingly in both $La_{2-x}Sr_xCuO_4$ and $YBa_2(Cu_{1-y}Zn_y)_3O_x$ the width of the transition is the same $\Delta T_c = 2.4\mathrm{K} \cdot (y/\%)$ [Rao88]. Some explanations for the depression of T_c are given in [Jay88] and references 1-27 in [Gup98]. Actually the T_c depression departs from linearity above 4% Zn [Shi92, Wes89] which was attributed to a non-linear charge transfer [Lan94b].

This very sensitive behaviour is reminiscent of the extreme susceptibility of collective singlet ground states in quasi-one-dimensional systems to non-magnetic impurities. The strong suppression of T_c is universal and can also be detected in other cuprate high temperature superconductors [Aga94].

To explain this, a straightforward explanation refers to the pair breaking effect via the basic Abrikosov-Gorkov mechanism, however there is evidence to suggest that this effect is too small to account for the rapid reduction of T_c [Wal93]. More elaborate theories taking into account the symmetry of the order parameter do reproduce the strong reduction in T_c [Fra97].

Induced local moment Once in the CuO_2-planes, the Zn impurities induce magnetic moments on the neighbouring Cu sites [Mah94] which are associated with low energy magnetic excitations [Sid96, Kak93, Mat93]. NMR experiments [Bob99, Bob01, All91, Mah94, Men99, Jul00, Wal93, Ish93], susceptibility measurements [Jee88, Jee88,

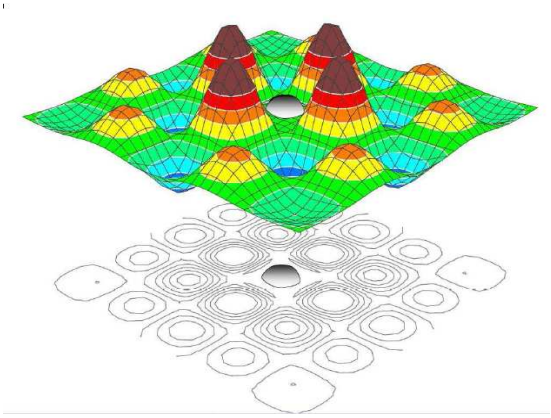

Figure 3.2: Staggered magnetic polarization around a Zn impurity resulting in a staggered magnetization [All07]

Zag96] and C_V measurements [Sis00] have shown clear pieces of evidence that there is an induced magnetic moment with total spin ½ in the vicinity each Zn impurity.

The NMR studies showed that the effect of a staggered paramagnetic polarization induced by Zn in $YBa_2(Cu_{1-y}Zn_y)_3O_7$ persists with little temperature dependence from above to below T_c [Oua06, Oua04]. The induced local moment is estimated to be $0.64\mu_B$ per Zn and moreover the nearest neighbours to the Zn impurity have a magnetic moment $0.32\mu_B$ per Cu and are antiferromagnetically coupled to the Zn moment [Zag95] (Fig. 3.2).

On the theoretical side, there have been a few works which attempt to show microscopically how such local moments may form in a two-dimensional strongly correlated fermion system [Zie96, Sen94, Sen96, Bas96, dH98]. One theoretical explanation for the local moment is that neighbouring spins in the CuO_2-planes form singlet and the induced moment arise from the spin whose singlet partner has been destroy by the Zn substitute [Par03]. When superconductivity disappears, the induced spins seem to freeze at low temperatures, creating a spin-glass-like disordered magnetic state [Men94].

Extension of the spin glass phase The compound $La_{2-x}Sr_xCuO_4$ shows spin glass behaviour at low temperatures in the doping range between the AF phase and the superconducting phase. On the other hand, the spin glass phase in pure $YBa_2Cu_3O_x$ is in a very narrow oxygen doping range. By doping Zn impurities this spin glass range is extended, so that the phase diagram of $YBa_2(Cu_{0.96}Zn_{0.04})_3O_x$ resembles that in pure $La_{2-x}Sr_xCuO_4$ (see Fig. 3.3).

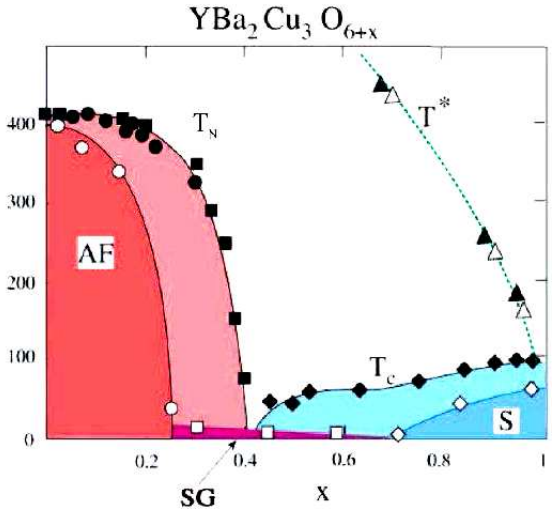

Figure 3.3: Phase diagram of pure and Zn-doped $YBa_2Cu_3O_x$: creation of an extended spin glass phase (SG) and suppression of antiferromagnetic phase (AF) and superconducting phase (S) upon Zn doping: dark symbols $YBa_2Cu_3O_x$; open symbols $YBa_2(Cu_{0.96}Zn_{0.04})_3O_x$ [All07]

3.4 Previous experimental data on $YBa_2(Cu_{1-y}Zn_y)_3O_x$ with techniques other than neutron scattering

3.4.1 Bulk measurements supporting pinning scenario

Stripe pinning One interpretation of the induced excitation observed with neutrons scattering comes from the stripe pinning idea, where fluctuating stripes are slowed down so that they can be observed in low-energy neutron scattering.

Support for the stripe pinning scenario came from thermal conductivity measurements in $La_{1.87}Sr_{0.13}CuO_4$ with optional Zn doping [Kaw05]. The thermal conductivity was slightly suppressed by an applied magnetic field as expected with stripe pinning and when Zn doping was present the suppression was smaller indicating that Zn doping had already developed some stripe pinning.

Stripe pinning force Examining this pinning force, early measurements tried to estimate the pinning force of pure and Zn doped $YBa_2(Cu_{1-y}Zn_y)_3O_{6.93}$ by high field magnetization studies [Zen95]. The deduced pinning force increased with magnetic field and reached a maximum at 25T for $y = 0$ and 5T for $y = 0.12$. Overall, the pinning force was reduced with increasing Zn content.

T_c as the key parameter Magnetization measurements on $YBa_2(Cu_{1-y}Zn_y)_3O_x$ examining the irreversibility field and the hysteresis indicated that the key parameter for

the magnetic properties is only T_c, i.e. samples with different x or y but the same T_c show the same behaviour [Mas01]. This is not surprising keeping in mind that a linear relation to the superfluid density $T_c \propto n_s$ has been suggested [Nac96] so that magnetic properties effectively depend on the superfluid density. From the T_c dependent vortex pinning force the authors argue that therefore a pure underdoped system should be as inhomogeneous as Zn-substituted system with equivalent T_c.

3.4.2 STM studies revealing quasi-particle states at impurities

STM is a technique for examining the surfaces of samples. By controlling the position of a conducting tip on the scale of interatomic distances, their tunneling current to the sample can be measured and thus the density of state deduced. The voltage between tip and sample is a free parameter to be adjusted. Finally spatially resolved pictures can provide valueable clues about the electronic structure of a substance.

This method is the most direct way for detecting inhomogeneities. The environment around Zn impurities can be examined to provide clues where the induced magnetic excitations originate.

Quasi-particle peaks at native impurity sites $Bi_{2-y}Pb_ySr_2Cu_2O_x$ An STM study not employing Zn doping, but examining the native impurities in $Bi_{2-y}Pb_ySr_2Cu_2O_x$ instead, yielded a low-energy peak at $\Omega = -2.75\,\text{meV}$. This feature shows no significant change upon crossing T_c. As a number of experimental studies suggest the existence of the pseudogap not only in the normal state, but also below T_c coexisting with superconductivity [LT06, Tan06, Boy07, Kon07], this feature could be attributed to the pseudogap state.

The relation to the Zn induced states is possible from the observation that the staggered paramagnetic polarization induced by Zn in $YBa_2Cu_3O_{7.0}$ is also unaffected by crossing T_c [Oua06, Oua04]. Another connection between impurity states and the pseudogap comes from ellipsometry experiments demonstrating that Zn impurities interact strongly with the pseudogap, [Pim05], with Zn giving rise to a gradual and inhomogeneous pseudogap suppression. As Ni on the other hand increases the pseudogap temperature, this can be interpreted as evidence for the importance of magnetic correlations in the pseudogap state.

Quasi-particle peaks at Zn impurity sites in BSCCO:Zn More directly related to Zn impurities, STM measurements on $Bi_2Sr_2Ca(Cu_{0.996}Zn_{0.006})_2O_x$ ($T_c = 84\,\text{K}$) measured a quasi-particle energy peak at $\Omega = -1.5\,\text{meV}$ at the Zn impurity sites [Pan00a]. It was found that superconductivity is destroyed within a radius of 15 Å and the quasiparticle LDOS maxima are detected not at the nearest neighbours, but at the next nearest neighbours again Fig. 3.4. Moreover Zn seems to be close to the unitary scattering limit.

Therefore impurities in general seem to induce extended quasi-particle states at their position in the CuO_2-plane.

3.4. Previous experimental data on $YBa_2(Cu_{1-y}Zn_y)_3O_x$ with techniques other than neutron scattering

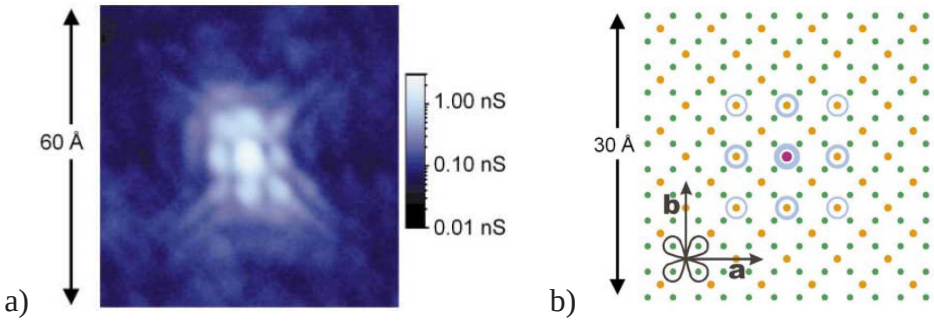

Figure 3.4: a) STM scans and b) corresponding model for the location of the maxima on next-nearest neighbours in the -1.5mV STM scan [Pan00a]; Cu atoms orange, O atoms green

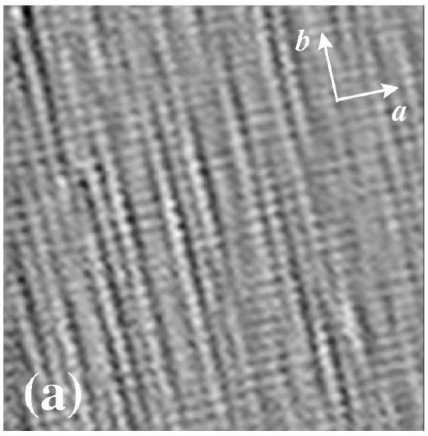

Figure 3.5: STM constant height image of $YBa_2(Cu_{0.97}Zn_{0.03})_3O_{6.93}$ (110 Å a side) at 5mV [Mak03]

Zn induced one dimensional modulations in $YBa_2(Cu_{0.97}Zn_{0.03})_3O_{6.93}$ Low temperature STM measurements on $YBa_2(Cu_{0.97}Zn_{0.03})_3O_{6.93}$ have detected one-dimensional charge-density modulations at low bias voltage on the surface, which have indirectly been attributed to the electronic local density of states in the CuO_2-planes [Mak03]. Perturbations have been seen which are parallel to the *b* axis and 10 to 21 lattice units long (Fig. 3.5). Their density was considerably higher than the Zn density alone - a reason why the authors attribute them to Zn induced instabilities at the Fermi surface, showing that the perturbation is not restricted to the local area around Zn impurities. The final conclusion was that Zn not just traps charge carriers, but triggers off a localization of the whole electronic state. This one-dimensional modulation can serve as an explanation for the observed large anisotropy in the low-energy neutron scattering data.

3.4.3 μSR studies in cuprates

In μSR measurements spin polarized muons are implanted into the samples, and get trapped at special attracting sites in the sample. The moment of the particle starts to precess with a speed according the the local magnetic field of the site. The muons decay into a positron and a neutrino after a lifetime of 2.2μs. The created positron is emitted preferentially in the direction of the magnetic moment of the muon and will leave the sample provided the sample is thin enough.

From the angular distribution of emitted positrons and the time between muon injection and positron detection, the precession velocity and thus the internal magnetic field at the muon site can be deduced. This method also allows the study of superconducting properties in particular of the penetration depth, since it is sensitive to the inhomogeneous field distribution emerging from vortices.

Swiss cheese model in $La_{2-x}Sr_xCu_{1-y}Zn_yO_4$ **and** $YBa_2(Cu_{1-y}Zn_y)_3O_{6.63}$ μSR measurements on Zn substituted $YBa_2Cu_3O_{6.63}$, $La_{1.85}Sr_{0.15}CuO_4$ and $La_{1.8}Sr_{0.2}CuO_4$ yielded the relation between the Zn content and the superconducting volume fraction which can be deduced from the relaxation rate [Nac96]. The evolution of the relaxation rate could well be fitted with a model where the Zn atoms are assumed to destroy superconductivity in a radius of 22.7 Å for $YBa_2(Cu_{1-y}Zn_y)_3O_{6.63}$ and 18.3 Å for $La_{1.85}Sr_{0.15}Cu_{1-y}Zn_yO_4$.

This extended influence of Zn impurities shows that they can induced substantial modifications in the electronic structure and keeping in mind that Zn atoms are only six lattice units apart in the CuO_2-planes, interactive effects between impurities are reasonable.

Zn-enhanced 1/8th phase in $La_{2-x}Sr_xCu_{1-y}Zn_yO_4$ Zero-field μSR time spectra were measured for $La_{2-x}Sr_xCu_{1-y}Zn_yO_4$ [Koi05]. From the muon-spin precession static stripe order was found most clearly for $x = 0.115$ where the 1/8 anomaly is most pronounced in $La_{2-x}Sr_xCuO_4$. With a substitution of Zn below the threshold $y \leq 0.03$, a precession is observed for $x = 0.10$, $x = 0.115$, $x = 0.13$, suggesting that Zn favours the development of static order by pinning a fluctuating phase.

For heavily doped samples $y > 0.03$, the precession disappears - probably due to destruction on spin correlations resulting from the spin dilution effect of the impurities.

By fitting the data to a three term function the authors deduce the volume ratio of three different phase depending on y. One phase corresponds to fast fluctuations beyond the μSR time window, one phase corresponds to slowing-down and incoherent magnetic order and the last phase corresponds to coherent static magnetic order (Fig. 3.6). The coherent magnetic order peaks at $y = 0.02$. It is important to note the the superconducting volume fraction follows remarkably close the volume ratio of the (first) fast fluctuating phase.

From the ratio of the three phases the radius of the Zn-affected area can be estimated to be $\xi \sim 36$ Å which is in agreement with other estimates from the swiss cheese model.

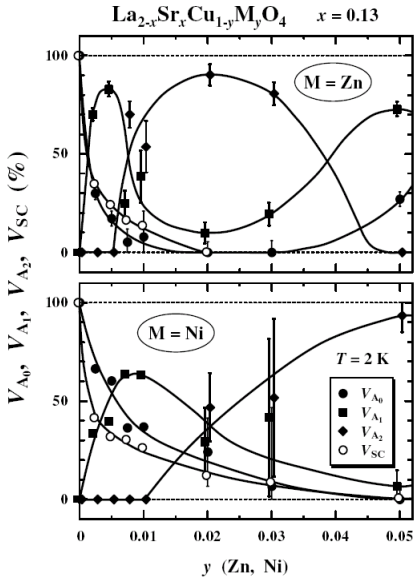

Figure 3.6: Zn doping dependence of the fraction of three phases identified by fitting μSR measurements [Koi05]

Zn-induced effect around 1/8th charge doping Previous μSR studies on the compounds $Bi_2Sr_2Ca_{1-x}Y_x(Cu_{1-y}Zn_y)_2O_x$ [Ako98, Wat99, Wat00] and $YBa_2(Cu_{1-y}Zn_y)_3O_x$ [Ako00] also found a slowing-down of Cu-spin fluctuations around the 1/8 charge doping state, however no muon-spin precession has been observed. These findings suggest that dynamical stripes which are most pronounced in the 1/8 phase could be a universal feature of hole-doped cuprates.

Consequently the μSR data provides evidence that Zn can favour the development of a non-superconducting phase (here the stripe phase).

3.5 Previous neutron scattering data in Zn doped cuprates

3.5.1 Zn-induced quasi-elastic incommensurate excitations in $La_{2-x}Sr_xCu_{1-y}Zn_yO_4$

The spin spectrum of pure $La_{1.86}Sr_{0.14}CuO_4$ shows incommensurate excitations at low energies, but these excitations are suppressed below a quasi-gap energy [Yam95] so that no static excitations are observed. It was found that when doping $La_{1.88}Sr_{0.12}CuO_4$ with Nd, static incommensurate excitations appear [Tra95].

But also Zn doping can induce quasi-static excitations as was shown in [Hir97]. The authors detect sharp quasi-static incommensurate excitations at 0.4 meV (not exactly 0 meV to avoid incoherent scattering) with a width a correlation length in excess of 70 Å. With excess oxygen doping the superconductivity in the pure sample can

be destroyed, yet the induced long-range AF fluctuations appear, indicating that these incommensurate excitations are not associated with superconductivity.

3.5.2 Zn-enhanced low-energy excitations in overdoped $La_{2-x}Sr_xCu_{1-y}Zn_yO_4$

Neutron scattering measurements on overdoped $La_{2-x}Sr_xCuO_4$ (x=0.20, x=0.25) showed that Zn enhances the low-energy response at 6 meV [Wak05]. A noteable observation was that while the two different compounds had different incommensurability parameters δ and correlation length ξ, upon Zn doping δ was reduced and the width $\xi \sim 6$ Å increased to the same value for both samples. No static order is induced by Zn in overdoped $La_{2-x}Sr_xCuO_4$.

3.5.3 Zn induced in-gap state in optimally doped $La_{1.85}Sr_{0.15}Cu_{1-y}Zn_yO_4$

Pure $La_{1.85}Sr_{0.15}CuO_4$ has a spin gap below 8 meV at low temperatures (around 10 K). Measurements on Zn doped $La_{1.85}Sr_{0.15}Cu_{1-y}Zn_yO_4$ showed that this spin gap is closed with increasing y [Kim03]. As the intensity above the gap does not change with Zn doping, the authors conclude that Zn induces a novel state rather than broadening the gap onset or lowering its energy. Also the temperature dependence of the sample with 0.8% Zn impurities indicates that this new state appears at low temperatures, resulting in a specific upturn at low temperatures of the signal at 3 meV. For higher doping levels $y = 0.017$ even a static signal appears with an in-plane correlation length of 80 Å, which is much longer than the inter-zinc distances.

A suggested explanation for the in-gap state is an onset of correlation between the moments of different Zn atoms in the CuO_2-plane.

3.5.4 Zn-induced low energy excitations and suppression of resonance in optimally doped $YBa_2(Cu_{1-y}Zn_y)_3O_{6.93}$

The optimally oxygen doped and Zn doped compound $YBa_2(Cu_{0.98}Zn_{0.02})_3O_{6.97}$, where superconductivity is most robust to impurity doping, was studied extensively by Yvan Sidis [Sid96].

In order to compare data at all energies, different experimental setups which are required to examine low and high energies respectively need to be accounted for.

Including all possible data scalings such as monitor correction, bilayer factor correction and monochromator correction (section 2.1.7), the magnetic signal in the pure and the $YBa_2(Cu_{0.98}Zn_{0.02})_3O_{6.97}$ sample has been compared (Fig. 3.7). The main difference is that Zn seems to induce a low energy signal, while the resonance vanishes, leaving a peaked contribution at 35 meV. The latter peak however does not display the

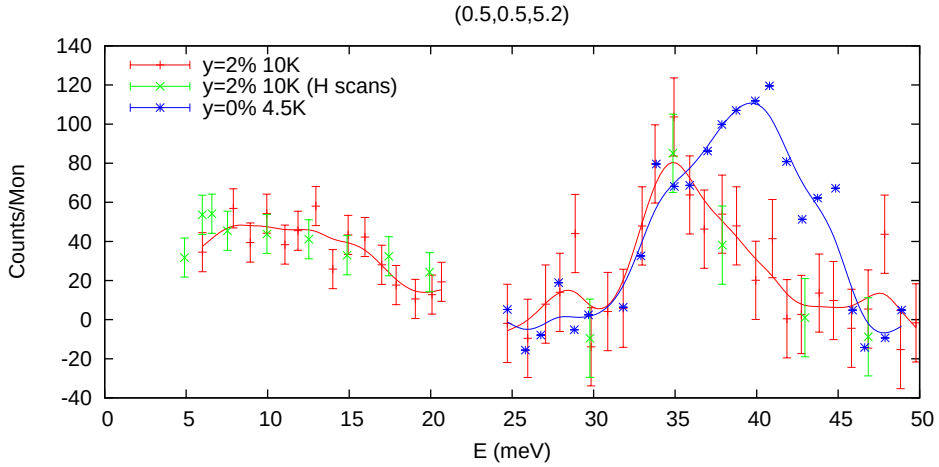

Figure 3.7: Neutron scattering intensity as a function of E at Q_{AF} in $YBa_2(Cu_{0.98}Zn_{0.02})_3O_{6.97}$ with high and low energy data scaled with respect to each other [Sid96]

T dependence with an abrupt change at T_c as expected for the magnetic resonance, however it indicates that a memory of the spin gap at $E_G \sim 33\,\mathrm{meV}$ remains.

On the theoretical side, these findings have been justified by Onufrieva who provided a model in the frame work of the t-t'-J model which explains χ'' by two contributions [Onu95b, Onu94, Onu95b]. One contribution from the subsystem of itinerant charge carriers and one from the localized spin subsystem with short range antiferromagnetic correlations. The itinerant charge carrier are thought to be responsible for the resonance peak.

3.5.5 Zn-induced low-energy excitations in optimally doped $YBa_2(Cu_{0.98}Zn_{0.02})_3O_{7.0}$

The magnetic signal in the $YBa_2(Cu_{0.98}Zn_{0.02})_3O_{7.0}$ sample studied by Sidis can be modelled at low-energies by

$$\chi''(H,K,L,\omega) \propto \exp\left(\frac{(\vec{Q}_{HK} - Q_{\mathrm{AF}})^2}{\sigma^2}\right) \cdot f_{\mathrm{Cu}} \sin^2\left(\frac{\pi L}{3.4}\right) \cdot \frac{\omega\Gamma}{(\omega-\omega_0)^2+\Gamma^2}$$

Each term will be explained in the following sections.

At 10 meV there is a clear Gaussian signal at (0.5,0.5,1.6) with a width of $\Delta Q \sim 0.29\,\mathrm{\AA}^{-1}$ which despite identical background is not seen in the pure compounds (Fig. 3.8).

The bilayer origin of this signal was confirmed by observing acoustic bilayer modulation (Eq. 2.5) in the L-dependence if the peak amplitude as expected from theory. This provides strong evidence that the signal is from spin excitations that are in the coupled bilayer CuO_2-planes.

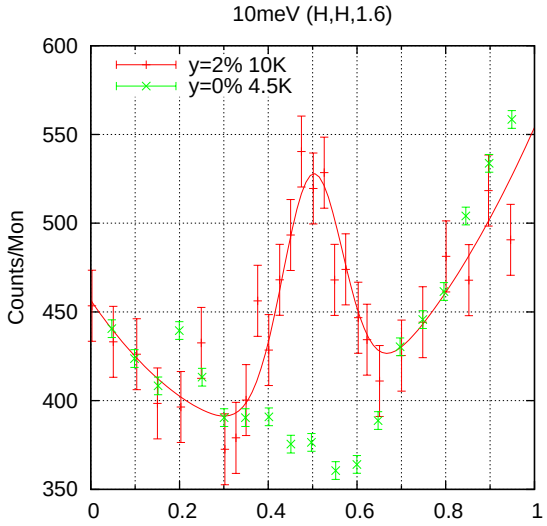

Figure 3.8: Neutron scattering intensity as function of Q in pure and Zn-doped $YBa_2Cu_3O_x$: induced low-energy magnetic signal in $YBa_2(Cu_{1-y}Zn_y)_3O_{7.0}$ [Sid96]

As seen in the model function, the signal amplitude as function of energy is fitted well with a Lorenzian form with the parameters $\omega_0 = 6\,\text{meV}$ and $\Gamma = 6\,\text{meV}$. Due to limited resolution the possibility of an energy gap was not examined in the paper.

These results were one of the first indications from neutron scattering, that Zn impurities can create quasi-static fluctuations near Q_{AF}. Yet, other experimental techniques such as STM studies had shown that, apart from suppressing superconductivity in an atomic-scale region, Zn impurities also generate low-energy excitations with a spatial symmetry that is in accordance with the d-wave nature of the superconducting gap [Cha08c].

3.5.6 Suppressed resonance in $YBa_2(Cu_{0.98}Zn_{0.02})_3O_{7.0}$

In nearly optimally doped $YBa_2(Cu_{0.98}Zn_{0.02})_3O_{7.0}$ a general trend upon doping with Zn has been found. With increasing Zn content the intensity at E_{res} drops, E_{res} slightly shifts to lower energies and the width in energy increases as can be seen in Fig. 3.9.

A magnetic signal at (0.5,0.5,5.2) was detected at [10 K 35 meV], but no contribution was found at [200 K 35 meV], [10 K 30 meV] or [10 K 47 meV], i.e. too far away from E_{res} or at too high temperature [Sid00]. The energy dependence of the magnetic signal has been extracted keeping in mind that there are two phonon contributions at 30 meV and 42 meV with a width of about 5 meV.

With Zn doping, the temperature dependence of the suppressed resonance peak loses its marked transition at T_c. Whereas there is no sign of a signal at high temperature in pure $YBa_2(Cu_{1-y}Zn_y)_3O_{7.0}$, in Zn doped $YBa_2(Cu_{1-y}Zn_y)_3O_{7.0}$ fluctuations survive as high as up to 250K.

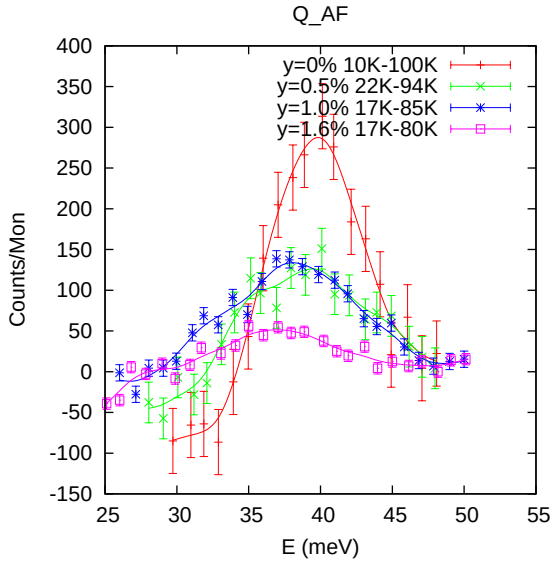

Figure 3.9: Neutron scattering intensity as function of E for $YBa_2Cu_3O_x$ with different Zn substitution levels: change of the resonance mode in $YBa_2(Cu_{1-y}Zn_y)_3O_7$ with increased doping of Zn (y = 0% [Fon95],y = 0.5% [Fon99a], y = 1% [Sid00], y = 1.6%)

3.5.7 Increase of energy-integrated spectral weight of resonance in $YBa_2(Cu_{0.95}Zn_{0.05})_3O_{7.0}$

High energy spin excitations in a sample $YBa_2(Cu_{0.95}Zn_{0.05})_3O_{7.0}$ have been examined previously [Fon99a]. By introducing 5% Zn impurities per Cu, the resonance broadens in energy range and also remains at high temperatures above T_c (Fig. 3.9). The authors find that the *energy integrated* spectral weight of the resonance features increases with Zn substitution, which they say is surprising for such a small amount of impurities.

3.5.8 Induced low-energy excitations in underdoped $YBa_2(Cu_{0.97}Zn_{0.03})_3O_{6.6}$

Some first results on underdoped $YBa_2(Cu_{0.97}Zn_{0.03})_3O_{6.6}$ were obtained by Kakurai [Kak93]. His team found that with such a large Zn content low frequency fluctuations at Q_{AF} were induced at all energies (2 meV-12 meV) and temperatures (10 K-200 K) studied. The temperature dependence of the intensities of the signal is shown in Fig. 3.10. Only at the lowest energies the excitations show a temperature dependent decrease of peak intensity with increasing temperature. The Q-width is very similar to the pure sample, indicating that the antiferromagnetically correlated regions have a similar spacial extension in pure and the Zn-doped compound as they are related directly to the Q-width (Eq. 4)

As an explanation for the finding of low frequency fluctuations the authors propose that dynamically correlated regions might be pinned by impurities leading to a quasi-

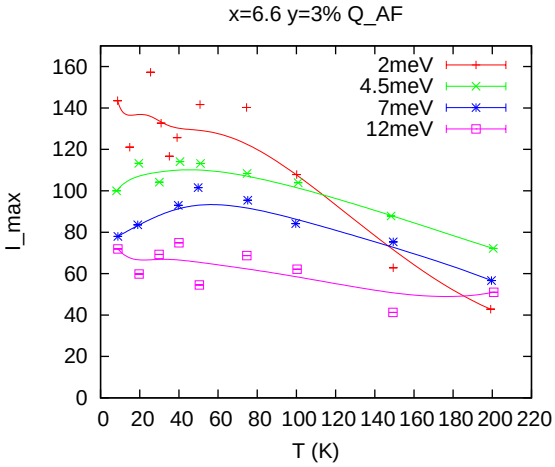

Figure 3.10: Neutron scattering magnetic signal intensity as function of temperature for different low energies in $YBa_2(Cu_{1-y}Zn_y)_3O_{6.6}$ as determined by the amplitude of Gaussian fits to the commensurate signal [Kak93]

static component which increases with temperature.

3.6 Neutron scattering data on $YBa_2(Cu_{0.98}Zn_{0.02})_3O_x$

For the $YBa_2(Cu_{1-y}Zn_y)_3O_x$ crystals investigated in this work, two parameters play an important role. First, the oxygen concentration x can be set. In this work $x = 6.45$ and $x = 6.6$ have been examined. Both energy ranges will be discussed separately. In principle the Zn content y is another parameter, however, in this work $y = 2\%$ is constant.

The main results for the $YBa_2(Cu_{0.98}Zn_{0.02})_3O_{6.6}$, described in detail in the following sections, are an appearance of low energy $E \sim 7$ meV fluctuations and a change of the resonance in the energy range $E \sim 37$ meV. This region is divided by the phonon contaminated region $E \sim 25$ meV, where the study of magnetic fluctuations turns out to be difficult. The high energy suppression of the resonance is not unexpected keeping in mind that Zn impurities do decrease T_c of a $YBa_2(Cu_{1-y}Zn_y)_3O_x$ crystal substantially.

The main result for the $YBa_2(Cu_{0.98}Zn_{0.02})_3O_{6.45}$ sample is, that a strong short-range 3D-ordered magnetic signal appears at (0.5,0.5,1), similarly to measurements in strongly underdoped $YBa_2Cu_3O_{6.35}$.

In the following section both samples and the low- and high-energy regions are discussed in detail.

3.6.1 Zn-induced low-energy excitations in $YBa_2(Cu_{0.98}Zn_{0.02})_3O_{6.6}$

In this thesis previous low-frequency measurements on a $YBa_2(Cu_{0.98}Zn_{0.02})_3O_{6.6}$ sample have been repeated, but with the advantage of being able to resolve differences in the *a* and *b* direction when scanning along *H* or *K* in reciprocal space around Q_{AF}. To achieve this, the sample consisted of a batch of carefully aligned and most importantly detwinned single-domain crystals.

The sample was mounted alternatingly in the (1,0,0) × (0,1.5,1.7) and (0,1,0) × (1.5,0,1.7) scattering plane in order to scan around Q_{AF}. The powerful spectrometer IN8 at ILL Grenoble with a setup to $k_f = 2.66\,\text{Å}^{-1}$ was used to perform scans of the type (0.5, 1.5, 1.7) and (1.5, 0.5, 1.7).

Anisotropic incommensurate signal Scans along *H* and *K* are shown in Fig. 3.11. The scans were fitted with the functions

$$I(H) = A\exp\left(-\frac{(H-(0.5+\delta))^2}{\sigma^2}\right) + A\exp\left(-\frac{(H-(0.5-\delta))^2}{\sigma^2}\right) + aH^2 + bH + c$$

$$I(K) = A\exp\left(-\frac{(K-0.5)^2}{\sigma^2}\right) + aK^2 + bK + c$$

which represent Gaussian peaks with a quadratic background.

All scans were performed at the bilayer maximum $L = 1.7$. The sample is rotated by 90° from one scan type to the other ($(H,K) \rightarrow (K,-H)$), resulting in resolution effects on the instrument to be identical, so that comparison of results and in particular peak widths is facilitated.

As seen in the plots, scans along *H* ("a" direction) show a clear incommensurate peak structure around Q_{AF}, whereas scans along *K* ("b" direction) show a single peak centered at Q_{AF}. The position δ of the incommensurate peaks does not disperse with energy notably. The apparent change of peak width in the 10 meV *H* scans of the 7 meV *K* scans is not thought to be physically relevant, but rather an artifact of the statistically perturbed measurement process.

The data suggests a complete model of the signal described by

$$I(H,K) = A\exp\left(-\frac{\left(\begin{pmatrix}H\\K\end{pmatrix}-\begin{pmatrix}0.5+\delta\\0.5\end{pmatrix}\right)^2}{\sigma^2}\right) + A\exp\left(-\frac{\left(\begin{pmatrix}H\\K\end{pmatrix}-\begin{pmatrix}0.5-\delta\\0.5\end{pmatrix}\right)^2}{\sigma^2}\right) \qquad (3.3)$$

which represents two Gaussian peaks centred at $Q_{AF} \pm (\delta, 0, 0)$, a FWHM $\Delta = \sigma 2\sqrt{\ln 2}$ and an incommensurability $\delta \sim 0.1$. A possible partial twinning with a domain ratio α can change the function to

$$I_{\text{twin}} = (1-\alpha)I(H,K) + \alpha I(K,H)$$

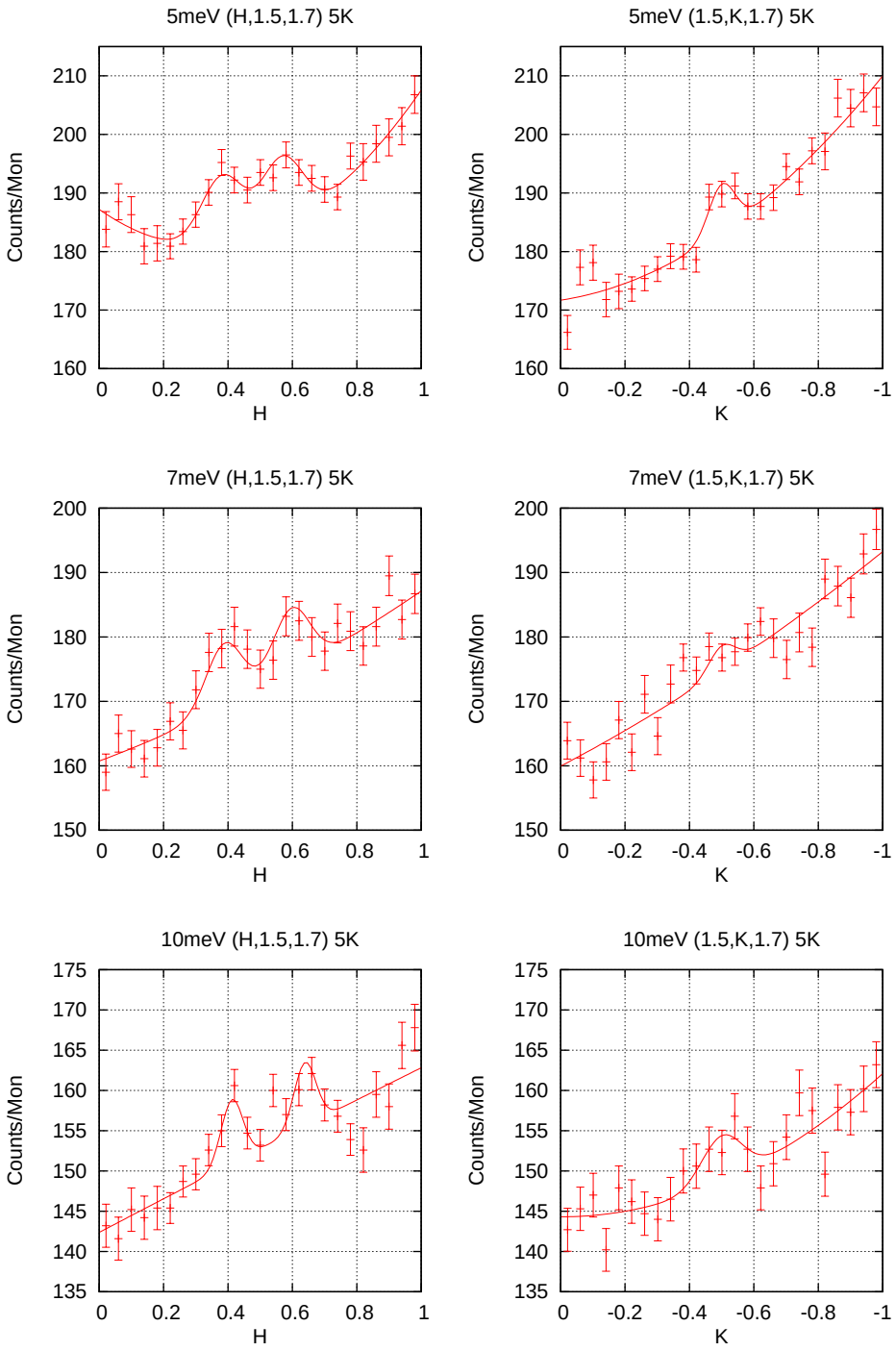

Figure 3.11: Neutron scattering Q-scans around Q_{AF} for different low energies in $YBa_2(Cu_{0.98}Zn_{0.02})_3O_{6.6}$ showing the a-b anisotropy at (IN8, $k_f = 2.66\,\text{Å}^{-1}$); incommensurability $\delta \sim 0.1$; Width of peaks for 10 meV H, 7 meV K and 10 meV K was taken from other fits to create the guide to the eye

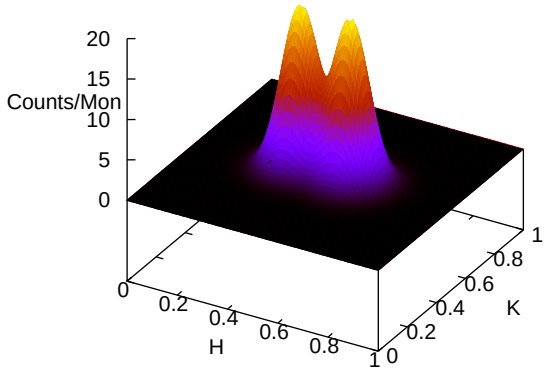

Figure 3.12: Representation of the in-plane distribution of the magnetic signal at low energies according to Eq. 3.3

For visualization a $I(H, K)$ plot of this phenomenological model is presented in Fig. 3.12. With this model in mind and taking into account the instrumental resolution the apparent commensurate character observed in diagonal scans (H, H, L_0) can be understood.

The signal is not restricted to the superconducting state as going to $T > T_c$ the signal remains as can be seen in Fig. 3.13 A scan along H shows the incommensurate signal and a "diagonal" scan $(H, H, 1.7)$ shows a centred peak as expected from the model.

Scans at the same energies have been performed on a pure $YBa_2Cu_3O_{6.6}$ sample, with the result that no signal was observed (Fig. 3.14). From the sample mass and the neutron flux, the statistics was chosen such as to be sufficient to show a similar signal if one were present.

Magnetic bilayer origin of signal The Brillioun zone periodicity is confirmed as the signal can be found at (0.5,1.5,1.7), (1.5,0.5,1.7) and (0.5,0.5,1.7). However the signal is not supposed to be seen at (0.5,0.5,0) or (0.5,0.5,3.5) since due to the bilayer modulation (Eq. 2.5) a maximum for odd excitations is expected at $L = 1.7$ and the contribution vanishes at $L = 0$ or $L = 3.5$.

To confirm the bilayer nature of the signal, measurements have been made at $L = 0$ where a signal arising from odd excitations of the coupled bilayers is expected to be absent. The data shown in Fig. 3.15 strengthen the bilayer origin of the signal.

To sum up one-dimensional low-energy incommensurate excitations have been found which presumably are induced by Zn and which originate from coupled bilayers. They show no notable dispersion and remain in the normal state.

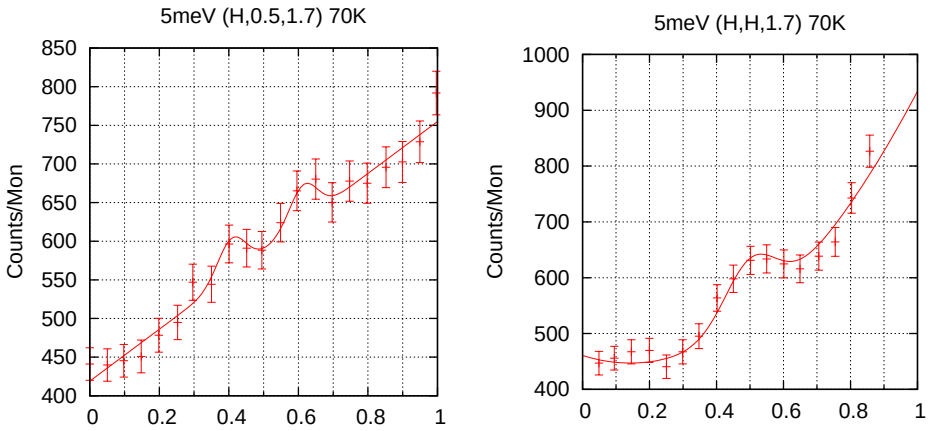

Figure 3.13: Neutron scattering Q-scans at 5 meV in the normal state of $YBa_2(Cu_{1-y}Zn_y)_3O_{6.6}$: persistence of the low energy magnetic signal slightly above T_c

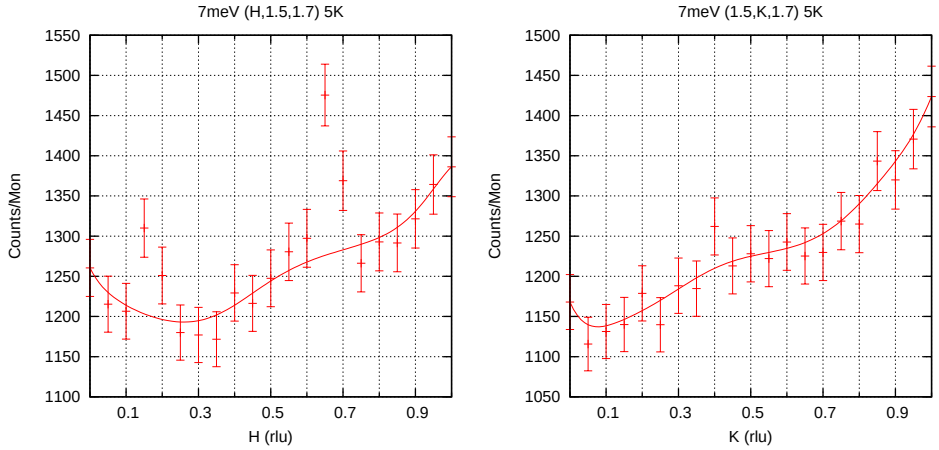

Figure 3.14: Neutron scattering Q-scans at 7 meV in pure $YBa_2Cu_3O_{6.6}$: absence of a low-energy signal; The peaks around 0.15 and 0.65 are spurions and were excluded in the fit

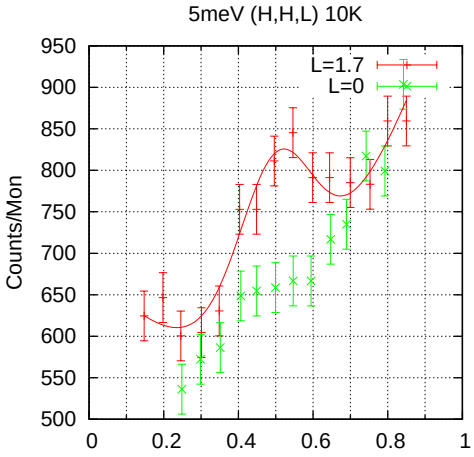

Figure 3.15: Neutron scattering Q-scan at 5 meV in $YBa_2(Cu_{0.98}Zn_{0.02})_3O_{6.6}$ at the maximum for odd excitations $L = 1.7$, and at the minimum $L = 0$

3.6.2 Zn-induced recovery of normal state at high energies at low temperatures

The high energies low-temperature excitations in underdoped $YBa_2(Cu_{0.98}Zn_{0.02})_3O_{6.6}$ look similar to the pure compound, but the character of the resonance in the pure compound is rather replaced by what looks like the normal state in the pure compound.

The raw low-temperature data do show magnetic excitations at the antiferromagnetic wave-vector at 38 meV, however the characteristic suppression upon crossing T_c is not seen anymore (Fig. 3.16). Thus Zn impurities not only suppress T_c, but also suppress of the resonance feature.

Reduction of the in-plane anisotropy at higher energies Anisotropies at E_{res}, which are present in the pure compound, can be compared in H and K plots. The data at 5 K in the Zn-substituted sample shows a weak anisotropy, however, it is much less pronounced than at 70 K in the pure compound (Fig. 3.17). A possible explanation is the poorer detwinning as in the pure sample the twin domain population ratio is 1:10 and in the Zn-substituted sample this ratio turns out to be 1:4 only.

The development of the anisotropy can be seen from scans at intermediate energies. This energy range is difficult to examine due to various contaminations. Some Q scans for selected energies are shown in Fig. 3.18. At 28 meV the H-scan is fittable with two Gaussian peaks, showing the decrease of the incommensurability as the energy increases. At 38 meV the data displays a single Gaussian peak, which cannot be resolved into incommensurate contributions.

Loss of characteristic temperature dependence at the resonance energy The temperature dependences of the signal at E_{res} have been measured for $YBa_2Cu_3O_{6.6}$ and

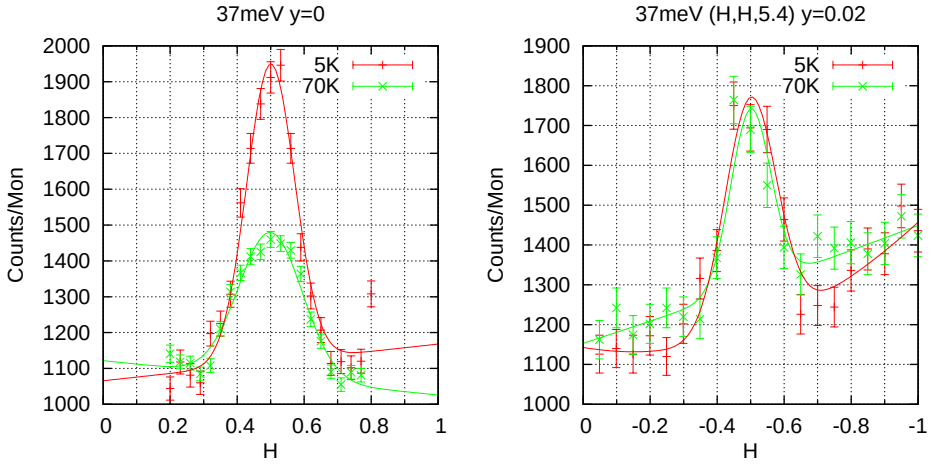

Figure 3.16: Neutron scattering Q-scans at E_{res}=37 meV (resonance of pure compound) in the superconducting and normal state of $YBa_2(Cu_{0.98}Zn_{0.02})_3O_{6.6}$ (IN8, $k_f = 4.1$ Å^{-1})

$YBa_2(Cu_{0.98}Zn_{0.02})_3O_{6.6}$. Measuring a phonon at 42.5 meV in the pure and the Zn-substituted compound, the signal in both samples could be calculated and compared. The result for the temperature dependence is shown in Fig. 3.19. The discrepancy at $L = 10$ is probably due to resolution effects due the different experimental setups. These effects are more pronounced at higher Q values.

One can see that the normal state intensity matches, while at T_c there is still an increase of the intensity, however the marked resonant upturn below T_c is absent. Therefore Zn drives the system strongly into the normal state - even more for the delicate resonance feature that is observed in cuprates.

3.6.3 Zn-induced changes in the spectrum of $YBa_2(Cu_{0.98}Zn_{0.02})_3O_{6.45}$

The pure $YBa_2Cu_3O_{6.45}$ has a $T_c = 35$ K. When doped with 2% Zn the T_c is suppressed as it would be for lower charge carrier density. However also the neutron scattering data resembles that of a sample with lower charge doping such as $YBa_2Cu_3O_{6.35}$ (T_c = 10 K).

Appearance of 3D magnetic order The most important effect is the appearance of 3D magnetic order, which can be deduced from the strong L-dependence of the elastic signal with peaked intensity at integer L-values Fig. 3.22. It seems that the signal is composed of two contributions. One at seen only at $L = 1$ (3D ordering) and the other usual diffuse response obeying the bilayer modulation and being seen at all L. In order to determine the contribution of each part, a procedure with some fixed fitting parameters was used.

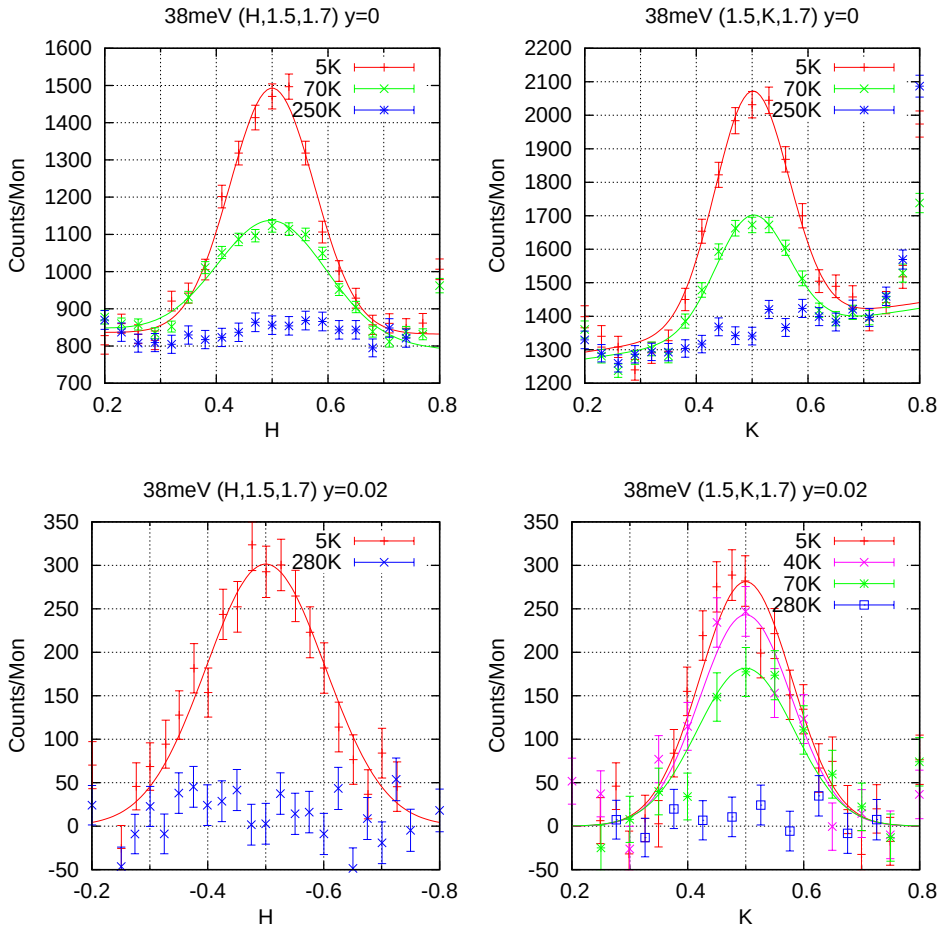

Figure 3.17: Temperature dependence of the magnetic intensity in scans along a^* and b^* at E_{res} in the pure and Zn-substituted $YBa_2(Cu_{1-y}Zn_y)_3O_{6.6}$ samples ($k_f = 4.1\,\text{Å}^{-1}$, IN8)

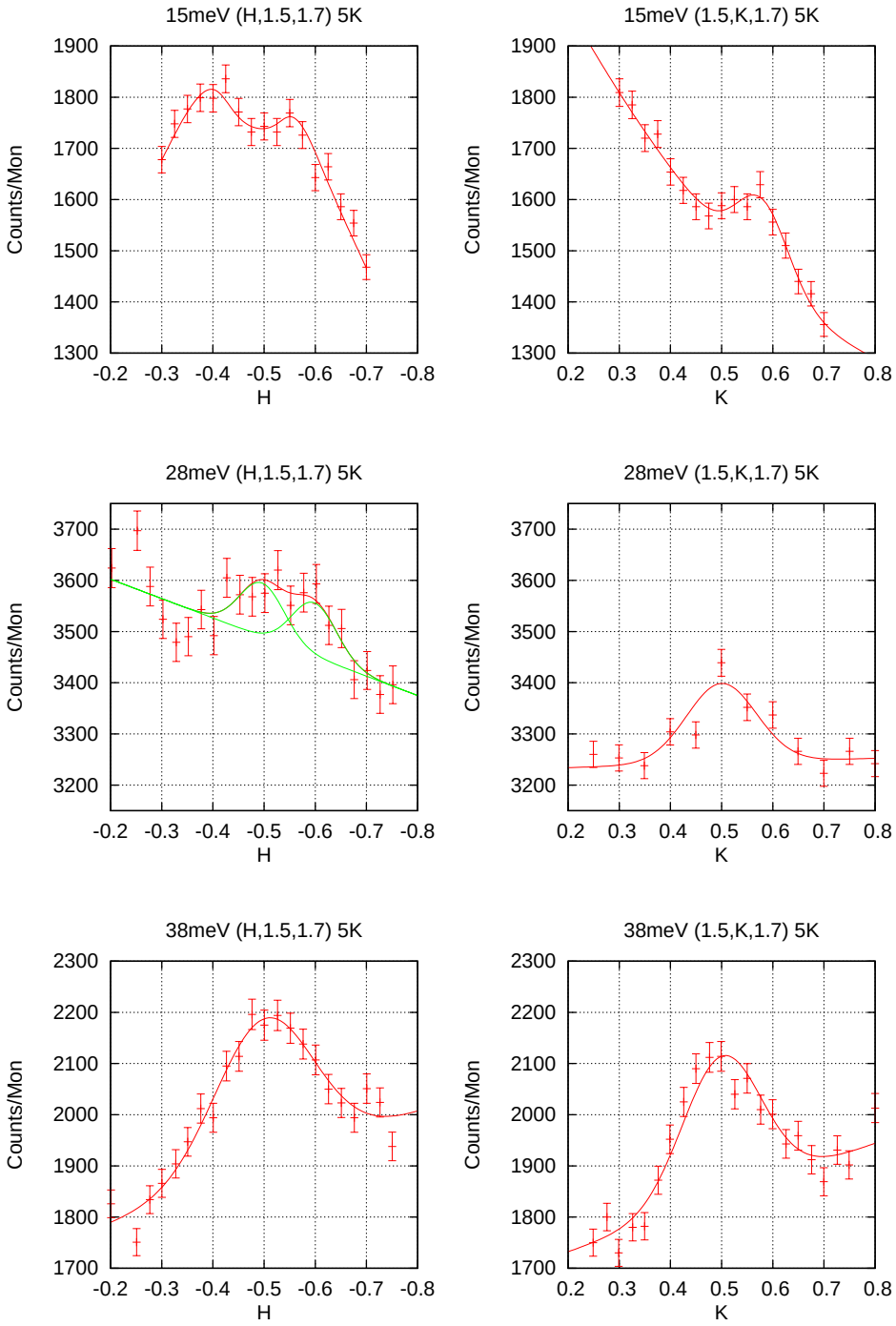

Figure 3.18: Neutron scattering Q-scans around Q_{AF} along H and K at high energies in $YBa_2(Cu_{0.98}Zn_{0.02})_3O_{6.6}$ (IN8, $k_f = 2.66\,\text{Å}^{-1}$)

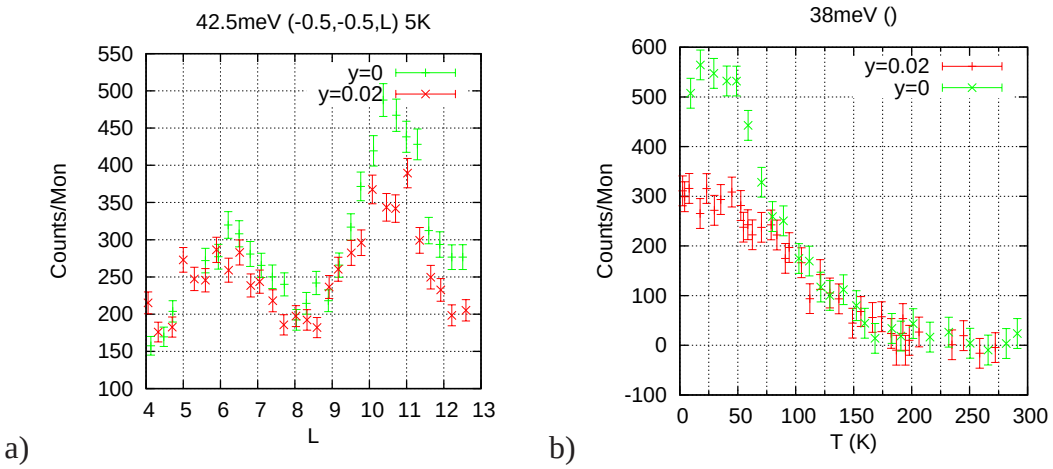

Figure 3.19: a) Neutron scattering L-scan of the 42.5 meV phonon in pure and Zn-substituted $YBa_2(Cu_{1-y}Zn_y)_3O_{6.6}$ after scaling the data by a factor; b) Neutron scattering intensity of the scaled signal at E_{res} as function of temperature dependence in pure and Zn-substituted $YBa_2(Cu_{1-y}Zn_y)_3O_{6.6}$

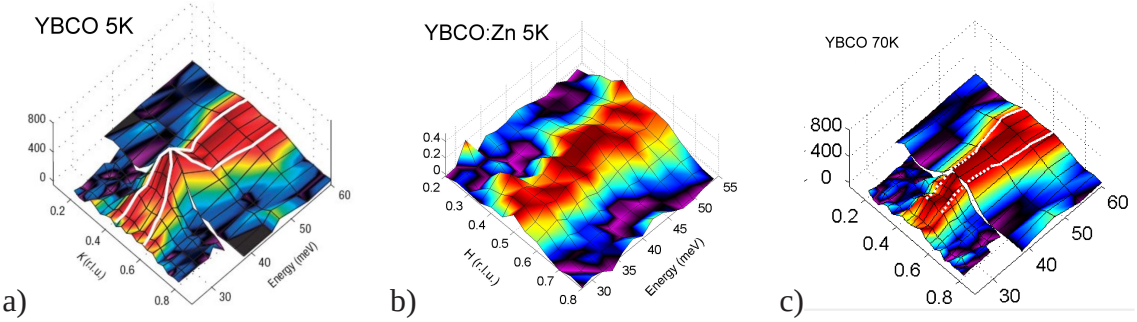

Figure 3.20: Dispersion of the neutron scattering intensity around E_{res} for: a) pure $YBa_2Cu_3O_{6.6}$ in the superconducting state; b) $YBa_2(Cu_{0.98}Zn_{0.02})_3O_{6.6}$ in the superconducting state; c) $YBa_2Cu_3O_{6.6}$ in the normal state

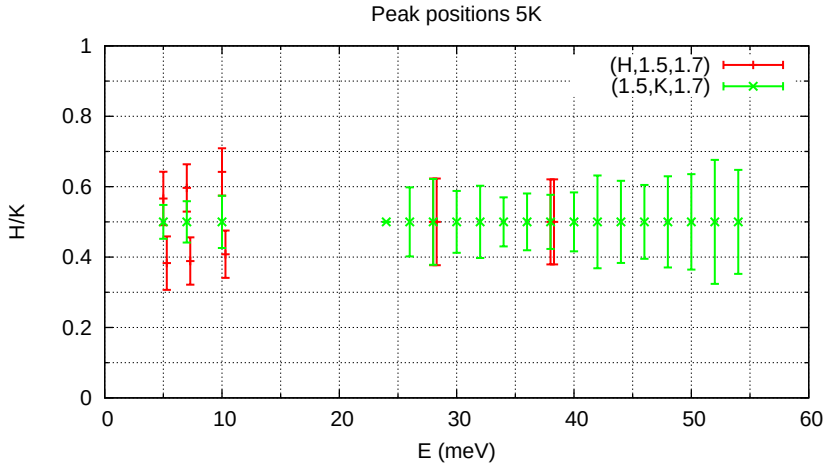

Figure 3.21: Positions of the peaks in scans along H and K, along with the peak width indicated by vertical bars in $YBa_2(Cu_{0.98}Zn_{0.02})_3O_{6.6}$ as determined from single Gaussian fits at high energies and double Gaussian fits at low temperature

First the width of the K scan at $L = 1$ was determined and this width was assumed to be the width for the 3D-ordered part in all subsequent fits. Next the H scan at $L = 1$ was fitted with two Gaussians of known incommensurability (same as in the pure compound [Hin08]) plus the 3D-ordered contribution with the same width as in the K scan, i.e. assuming that this part is isotropic. Now with the amplitudes determined from the H scan, the K scan was refitted with two centered Gaussians in order to visualize the diffuse contribution in that scan. Finally the H scan for $L = 1.4$ was fitted with the same method as the one at $L = 1.0$. The amplitude of the diffuse contribution at $L = 1.4$ comes out comparable to the $L = 1.0$ graphs as expected. Additionally, a small contribution from the 3D-ordered signal is seen, which is presumably the tails of its strength at $L = 1.0$ and $L = 2.0$.

From these scans the correlation length of the 3D-ordered signal in lattice units is

$$\xi_{\text{plane}} = 6\,a$$
$$\xi_{\text{c-axis}} = 1.2\,c$$

showing that the antiferromagnetic order is short ranged.

This 3D-ordered signal disappears above 30 K (Fig. 3.23) which is very close to what is seen in pure $YBa_2Cu_3O_{6.35}$.

It is important to note that a similar 3D order (Fig. 3.24) has been observed in $YBa_2Cu_3O_{6.35}$ ($T_c = 10$ K) which due to its lower oxygen content also has a low T_c.

Anisotropic inelastic bilayer signal The low-energy signal was examined from 0.3 meV to 5 meV and the anisotropy seen in the pure compound [Hin08] could be confirmed Fig. 3.25. The anisotropy is clearly visible, however a definite incommensurate struc-

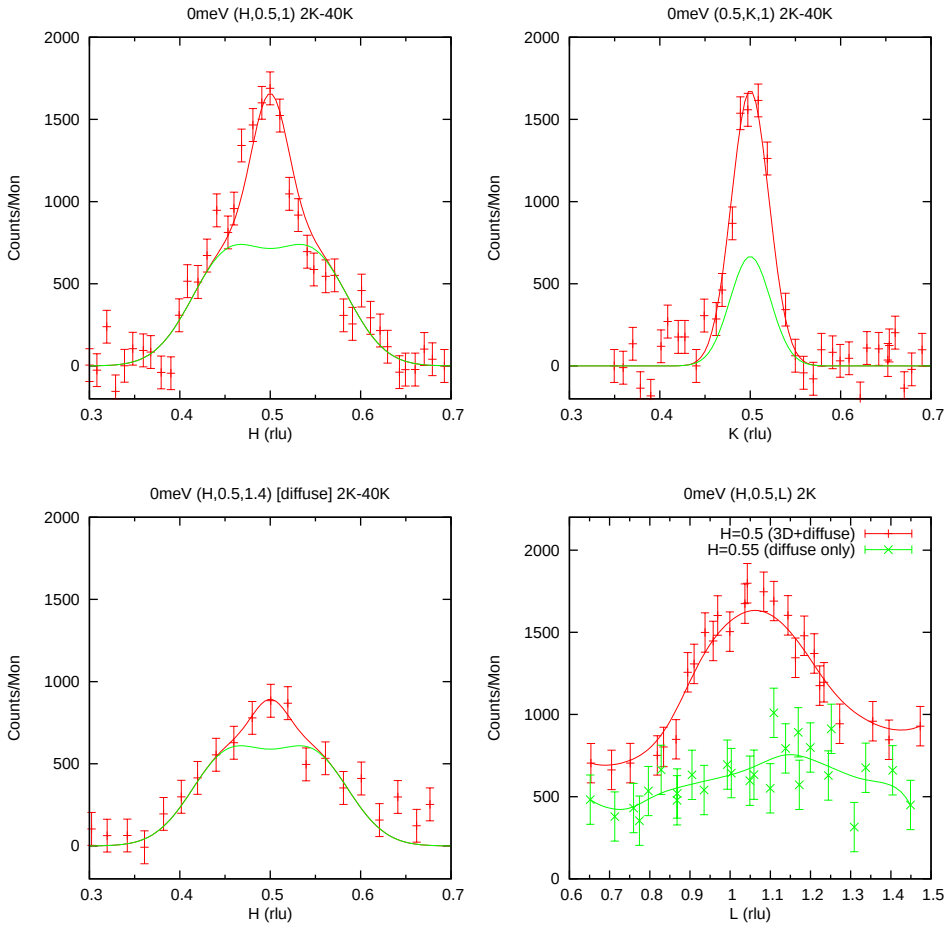

Figure 3.22: Elastic *Q*-scans showing the intensity difference between 2 K and 40 K at different *L*; The green curves show the diffuse contribution as explained in the text

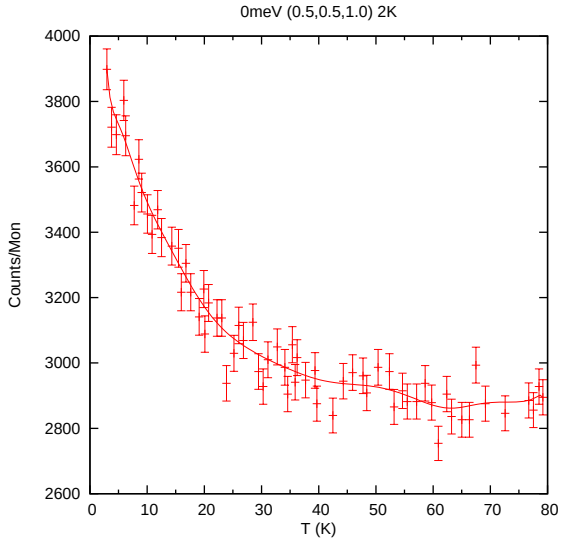

Figure 3.23: Elastic neutron scattering intensity as a function of temperature of the $L = 1$ 3D-ordered signal in $YBa_2(Cu_{0.98}Zn_{0.02})_3O_{6.45}$: disappearance at 30 K

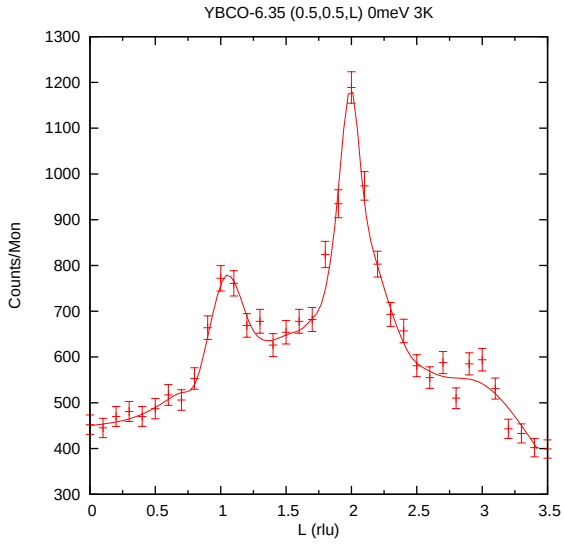

Figure 3.24: Polarized elastic neutron scattering L-scan at Q_{AF} in $YBa_2Cu_3O_{6.35}$ indicating for inter-layer correlations (measured by D. Haug)

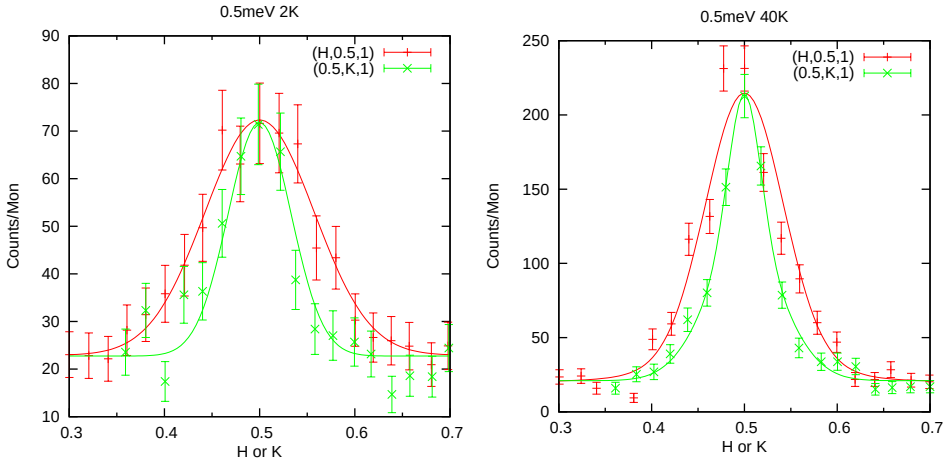

Figure 3.25: Inelastic neutron scattering Q-scan along H and K at 0.5 meV at low and high temperatures in $YBa_2(Cu_{0.98}Zn_{0.02})_3O_{6.45}$: indicating decreasing width at high temperature

ture could not be resolved. Curiously, the signal gets sharper as the temperature is increased to 40 K. This is interpreted in terms of the sharp elastic 3D-ordered signal at low temperatures becoming broader at elevated temperatures and thus its contribution to the quasi-elastic signal making its width artifically sharper.

It is interesting to examine the energy dependence of the peak width at low and high temperatures (Fig. 3.26). Two observations can be made. First, the width of the bilayer signal decreases slightly with increasing energy at low temperature. Second, at high temperatures this trend is reversed as expected from the prediction that the sharp elastic signal will broaden at high temperature and contribute at the lowest energies.

3.7 Summary of observed effects

To sum up the most important fact of the experimental data just mentioned:

- Zn strongly suppresses T_c, even stronger in underdoped cuprates
- Zn induces a staggered magnetization in a 15 Å radius around the impurity; unaffected by crossing T_c
- Zn suppresses the magnetic resonance feature and removes its sharp change at T_c
- Zn induces incommensurate low-energy magnetic excitations in underdoped $YBa_2(Cu_{1-y}Zn_y)_3O_x$
- Zn doping is similar to charge doping reduction; a 3D-ordered signal is seen in strongly underdoped crystals

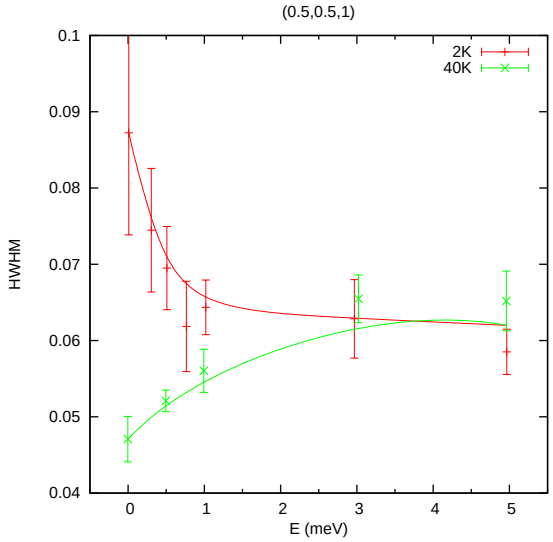

Figure 3.26: Half width at half maximum as a function of E in $YBa_2(Cu_{0.98}Zn_{0.02})_3O_{6.45}$ at low and at high temperatures

- stripe pinning with magnetic field is reduced if the compound is Zn doped (stripes already pinned)
- Zn induced quasi-elastic excitations in $La_{1.86}Sr_{0.14}Cu_{1-y}Zn_yO_4$
- Zn induces in-gap states in $La_{1.85}Sr_{0.15}Cu_{1-y}Zn_yO_4$ with inter-Zn correlations
- quasi-particles peaks at -1.5 meV found on next-nearest neighbours of Zn impurity sites
- 1D charge-instabilities seen with STM in $YBa_2(Cu_{1-y}Zn_y)_3O_x$
- Zn (if below a threshold) favours development of static order even away from the 1/8 phase in $La_{2-x}Sr_xCuO_4$
- slowing-down of Cu spins observed around the 1/8 phase charge doping in $YBa_2Cu_3O_x$ and $La_{2-x}Sr_xCuO_4$

Looking at these experimental results the nature of Zn seems to be, that the CuO_2-planes electronic structure seems to be fragile as soon as Zn impurities are introduced, as the impurities site affects a radius of four lattice units. The magnetic excitations, which are possibly not directly related to superconductivity, get restored at low-energies and broadened at high energies. This effect is anisotropic in anisotropic compounds such as $YBa_2Cu_3O_x$. Zn seems to induced local changes or even localize previously dynamic structures.

3.8 Interpretation of Zn effects

Theoretical calculations Theories have been proposed to explain the induced local antiferromagnetic states around zinc impurities in cuprates. Theoretically localized bound states around Zn impurities have been found in exact small-cluster t-J diagonalizations [Zie96, Poi94b, Poi94a, Oda97, Rie96]. Similarly the enhancement of local moment has been predicted [Mah94, Zie96]. Theoretical reviews attempting to explain the experimental data can be found in [Bal06, Hus02, Hir02].

Magnetic properties and disorder Magnetic properties of cuprates have been shown to change below a critical hole doping p_c where a Metal-Insulator Crossover (MIC) can be observed in the low temperature normal state . This effect can be attributed to a magnetic order competing with superconductivity. However, between different cuprate families p_c is not universal and varies from $p_c \sim 0.1$ in $YBa_2Cu_3O_{6.5}$ to $p_c \sim 0.16$ in $La_{1.84}Sr_{0.16}CuO_4$, which can related to the specific disorder that is inherent in each of these cuprates. Therefore, tuning the disorder by impurities could likewise change p_c and influence the magnetic properties. Indeed, similar effects could be obtained by introducing point defects in $YBa_2Cu_3O_x$ $x > 6.5$. An upturn in the resistivity, usually associated with the MIC, appears in underdoped $La_{2-x}Sr_xCuO_4$ and strongly underdoped $YBa_2Cu_3O_x$ $x < 6.5$ and saturates at high magnetic fields as expected for a Kondo-like effect [WU87]. For $YBa_2Cu_3O_x$ $x > 6.5$ this behaviour can be restored by the point defects in the CuO_2-planes [WU87]. However, the disorder-induced antiferromagnetism is not specific to the physics in the CuO_2-planes, as for example this effect has also been observed in the inorganic spin-Peierls spin-gap system $CuGeO_3$ [Reg95, Has96, Fuk96a].

Consequently, any change in disorder will affect the magnetic properties, in particular the magnetic excitations as shown in this work.

Magnetic instability The effect of disorder can also indicate the existence of a nearby magnetic instability. Since close to a magnetic instability quantum and thermal fluctuations are reduced around defects, the resulting magnetic correlations, that have been measured in this work, can induce the observed Kondo-like upturn of the resistivity [Gou87].

Anisotropy The one-dimensionality of the observed excitations has theoretically and experimentally been confirmed with other techniques. Evidence is found in particular in orthorhombic $YBa_2Cu_3O_x$, where charge transport properties [Tsu00] and spin fluctuations measured by inelastic neutron scattering [Dam03] are anisotropic in the *ab*-planes in the underdoped regime close to p_c. To account for this anisotropy, different phase have been proposed theoretically, such as a stripe phase [Sca95], a spiral magnetic state , incommensurate SDW [Joh89] or a *d*-wave Pomeranchuk instability [Pim05].

Stripe pinning The one-dimensionality of the induced excitations can be attributed to the stripe electronic phase. Impurities are thought to pin the fluctuating stripes and thus reduce energy of the possible scattering process at the stripe structures.

The stripe pinning scenario has been evidenced from μSR [Ris08, Ada08], magnetic susceptibility [Ada08], resistivity measurements [Pig07]. The stripe pinning model and its relation to transport, μSR and neutron scattering measurements has been discussed in [Koi01]. The universality for stripe pinning in different cuprate was shown in [Koi00a, Koi00b]. From theoretical investigations it was suggested that the stripe-pinning effect of Nd and Zn is different though [Smi01]. While Nd truly suppresses fluctuation of stripes, Zn pins the strips in a disordered manner and promotes line meandering.

Chapter 4

Effect of magnetic field on magnetic excitations in cuprates

Magnetic field as a perturbation Apart from impurity doping, another way to perturb the physics of a material is by application of a strong magnetic field. Again theories can incorporate the additional magnetic potential into their calculations and predict results so that wrong theories can be disproved. However, in practice calculations with magnetic field are unfeasibly complex. Another complication arising in superconductors is the inhomogeneous effect of an applied magnetic field. Due to the Meissner effect, superconductors in general try to expel magnetic field by producing dissipationless supercurrents. However this costs energy and for type-II superconductors such as the cuprates it is energetically advantageous to save expulsion energy by letting a few regions in the material become magnetically penetrated and non-superconducting. These regions are named vortices and their dynamics can give rise to new phenomena and also decisively determine the ability to carry supercurrent. The electronic structure of the vortex cores, as well as the interaction between them, is intimately connected with the nature and behaviour of charge carriers.

Vortex cores A vortex consists of a small non-superconducting core from where superconductivity starts to rebuild over a distance of the superconducting coherence length. Contrary to conventional superconductors, cuprates have a very small superconducting coherence length. Therefore also the vortex cores are tiny and also easily pinned by defects. The magnetic field inside the vortex core decays outside over a distance of the magnetic penetration depth λ. The extended character of the vortices bears many similarities with the dramatic effect of Zn impurities. Depending on many parameters, vortex dynamics can give rise to various vortex position ordering and even specific shapes of individual vortices. For example vortices in $YBa_2Cu_3O_x$ have been found to be elliptic and vortices in $Bi_2Sr_2CaCu_2O_x$ often have very irregular shapes. However this large scale behaviour will not be considered here. Instead in microscopic internal structure of the regions in and around the vortices will play a role. Apart from bulk neutron scattering, mostly STM and STS measurements can provide such infor-

mation.

Electronic structure of vortex cores The electronic structure of vortices in conventional superconductors was studied theoretically very early [Car64] with the prediction that at the vortex discrete electronic bound states below the superconducting gap form with an interlevel spacing of the order of Δ^2/E_F, but for most conventional superconductors this spacing is so small, that it cannot be resolved. High temperature superconductors turned out to be completely different as the core spectra of the cuprates revealed a single pair of low-energy peaks at specific energies $\pm E_{\text{core}}$.

Checkerboard modulation Another feature found in STM or STS measurements are periodic modulations in samples. Large scale modulation of the gap of the order 30-100 Å are found, but not considered here. However, additional small scale modulations of the LDOS of the order 16-20 Å around vortex cores have been found which corresponds to about four lattice spacings. These microscopic modulations will play a role as neutron scattering probes modulations with a correlation length of this order of magnitude.

4.1 Previous experimental data with techniques other than neutron scattering

Other experimental method are capable of detecting local order in sample in an applied magnetic field. In the following sections results from μSR, NMR and STM are presented, which support the idea of local formation of static order that was already indicated by the neutron scattering results in the previous chapters.

4.1.1 μSR measurements

μSR measurements are able to detect the local magnetic environment around the muon sites in a sample. Various cuprate superconductors have been object of study.

μSR measurements in $La_{1.88}Sr_{0.12}CuO_4$ have found field-induced quasi-static magnetism [Sav05]. μSR measurements on $YBa_2Cu_3O_{6.5}$ in applied fields of 4T could be well described by a model where static magnetic fields B=18G appear in the vortex cores below 10K [Mil02]. This effect has not been found in optimally doped $YBa_2Cu_3O_{6.93}$ at 6T or in the conventional superconductor $NbSe_2$.

4.1.2 Vortex core states deduced from NMR

Vortex core quasi-particle states in $YBa_2Cu_3O_x$ Nearly optimally doped $YBa_2Cu_3O_x$ (T_c = 92.5 K) crystals were examined with high-magnetic field ^{17}O NMR in order to resolve the electronic structure inside and outside the vortex cores [Mit01]. With fields up

to 37 T the vortices occupy 15% of the sample. Using the known distribution of internal magnetic field, spatially resolved NMR detected strong antiferromagnetic fluctuations outside the vortex cores and new electronic states inside the vortex cores different from conventional superconductors.

Antiferromagnetic ordering in the vortex cores in $Tl_2Ba_2CuO_{6+\delta}$ Another spatially resolved ^{205}Tl NMR study of nearly optimally doped $Tl_2Ba_2CuO_{6+\delta}$ ($T_c = 85\,K$) with fields up to 2.1T along the c-axis found direct evidence that antiferromagnetic spin correlations are significantly enhanced in the vortex core region. The core region shows local AF ordering with moments $0.1\mu_B$ parallel to the layers and a Neel temperature $T_N = 20\,K$ above which the cores are in a paramagnetic state.

4.1.3 Super-structures suggested by quantum oscillations

Quantum oscillations are oscillations in the inverse-field-dependence of electrical conductivity or magnetic susceptibility whose frequency is determined by the size of closed electron orbits on the Fermi surface. The observered oscillation frequencies combined with the negative sign of the low-T Hall coefficient are indicative of small electron-like surface pockets [DL07]. The normal Fermi surface as determined from ARPES measurements does not indicate Fermi pockets, however due to field-induced super-structures a Fermi surface reconstruction is possible and various theoretical works explain the appearance and size of the Fermi pockets by proximity to the 1/8 stripe phase [Mil07] or DDW [Pod08, Cha08a].

4.1.4 STM/STS measurements of checkerboard modulation and quasi particle states in vortices

Vortex core states in $YBa_2Cu_3O_{7.0}$ Vortex cores in optimally doped $YBa_2Cu_3O_{7.0}$ have been examined with STM and quasi-particle states near the vortex cores were found at $\pm 5.5\,meV$ [MA95, Shi03]. The energy shows no shifts with magnetic fields.

Vortex checkerboard modulation in $YBa_2Cu_3O_x$ STS studies on optimally doped $YBa_2Cu_3O_{6.93}$ revealed an intra-vortex features with a modulation of 4x4 lattice units [Bey08]. This extended effect around vortices was also found in other experiments. Neutron scattering experiments [Lak01] and STS studies [Ren98, Pan00b, Hof02, Fis07] showed that the effective vortex radius is substantially larger than ξ_{SC}. The authors find the normal superconducting coherence peak at $\Delta_{SC} = 20\,meV$ which is distributed fairly homogeneously across the sample. However another feature attributed to competing order with an energy 32 meV was also found. The measured spectra can be fitted well with a theoretical approach considering a CDW or SDW with a wavevector of 10 lattice spacings periodicity.

Upon application of magnetic field up to 6T vortices have been examined. Curiously the vortex size decreases from 77 Å for 2 T down to 50Å for 6 T. Apart from the zero-field features, i.e. the superconducting coherence peak and the competing order peak, additional subgap features at 7 meV appear and become more pronounced with increasing field. Fourier filtering analysis shows that the zero-field features display a checkerboard like modulation in the vicinity of the vortex cores with dimensions roughly 4 lattice units Fig. 4.1.

The energies of the superconducting coherence peak and the competing order feature remain unchanged with magnetic field, however the spectral weight is shifted into the latter implying a field-induced microscopic order.

The finding of a 4x4 lattice units modulation inside the vortex cores has been attributed to the presence of a coexisting order.

Vortex core states in $Bi_2Sr_2CaCu_2O_{8+x}$ Vortex core states in a magnetic field of 7 T have been found in $Bi_2Sr_2CaCu_2O_{8+x}$ (T_c = 87 K) at ±7 meV with an exponential decay radius of 22 Å [Pan00b]. In a second measurement, a very dilute concentration of Zn impurities was used to show that vortices predominantly become pinned at Zn impurity sites.

Relation between vortex core states and checkerboard in $Bi_2Sr_2CaCu_2O_{8+x}$ A relation between the vortex core states and the checkboard modulation was established in slightly overdoped $Bi_2Sr_2CaCu_2O_{8+x}$ (T_c = 88 K) [Lev05]. In zero field a 4x4 lattice units modulation can be found at -15 meV. Examining the vortex cores at 6 T yields non-energy-dispersive 4.3 lattice units checkerboard modulation oriented along the Cu-O bond clearly visible between 4 meV and 12 meV and between -4 meV and -12 meV, where the negative bias (occupied states) is 2/3 smaller than the positive bias.

The strongest signature of quasi-particle core states is seen at positions where the checkerboard modulation reaches a maximum, which draws a close connection between these two effects.

An indication of anisotropy comes from the observation that a $^4/_3$ lattice modulation is seen along the Cu-O bond in the a-axis direction only.

Vortex core checkerboard modulation in $Bi_2Sr_2CaCu_2O_{8+x}$ STM measurements on slightly over-doped $Bi_2Sr_2CaCu_2O_{8+x}$ (T_c = 89 K) in 5 T field displayed a 4x4 checkerboard spatial structure with a pattern along the Cu-O bonds [Hof02]. The correlation length is 7.8 lattice units. The checkerboard pattern is anisotropic, as the Fourier transform yields an intensity ratio of 3 between the *a*-axis and *b*-axis modulation. At 5 T the vortex-induced LDOS is detected at least 50 Å away from the core, which means that 25% of the sample is under influence of the phenomenon creating the checkerboard pattern.

As a theoretical explanation a SDW phase or two orthogonal stripes phases have been proposed to account for these observations.

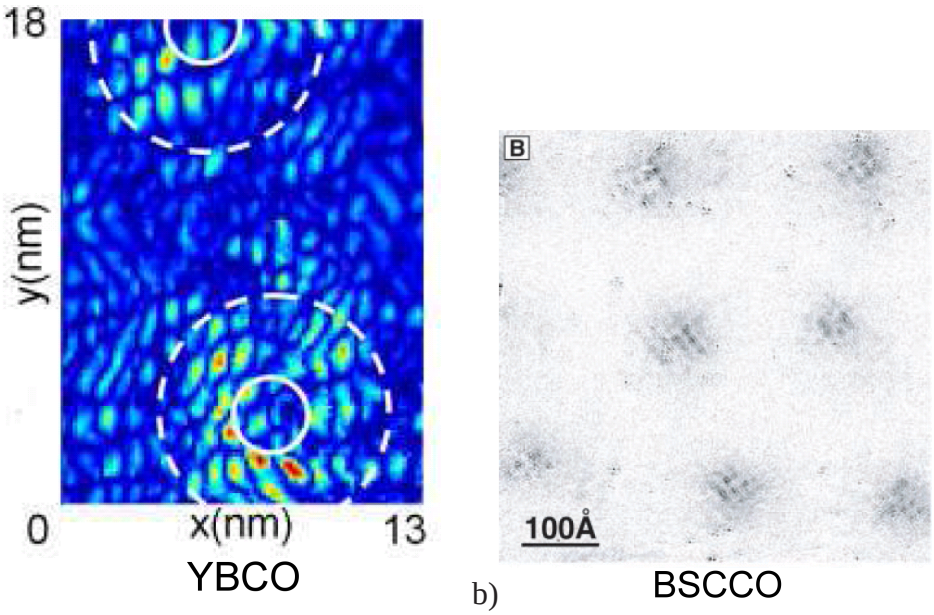

a) b)

Figure 4.1: Checkerboard pattern of superconducting coherence peak around vortex cores in a) Analyzed STM data on YBCO [Bey08]; b) STM data on BSCCO [Hof02]

Theoretical proposal for checkerboard modulation With the suppression of superconductivity inside vortex cores, a variety of competing ordered states can appear. As the superconductivity is weakened spin [Aro97, Dem01, Zhu01] or orbital order [Kis01, Wan01] will coexists near the core and this localized state will create a spatial modulation in the LDOS.

A pair density wave has been proposed be several authors [Che02, Che04, Tes04, And04]. The relation between pseudogap and the superconducting state has been the topic of many theoretical studies possibly leading to spatially modulated structures [Zaa89, Zha97, Voj99, Wen96, Cha01]. Other explanations include one-dimensional stripes [Kiv03], modulations of the electron hopping amplitude [Pod03], Cooper pair Wigner crystal [Che04], density wave [Tes04], incommensurate CDW [Li06] and orbital-current induced d-density wave [Seo07]. More theoretical approaches can be found in [Pan00b, Ref. 9-27]

Some properties of the phase diagram, the low-energy dynamics and the relation between superconductivity and magnetism can also be deduced from the SO(5) model [Zha97, Aro97] that unifies antiferromagnetism and d-wave superconductivity. This theory also predicts that vortex cores should be antiferromagnetic.

4.2 Preparation of $YBa_2Cu_3O_{6.45}$ samples

Growth, annealing and detwinning As the crystals are pure $YBa_2Cu_3O_x$, the growth and annealing producedure is unchanged from what is described in section 2.4.1 and

sample	mass	annealing	twin domain ratio	T_c
$YBa_2Cu_3O_{6.45}$	2000mg	580 °C, 0.5% O_2	1:12	~ 35 K

Table 4.1: Properties of the pure sample used for the neutron scattering experiments

2.4.2. Just as the Zn doped crystals, the pure crystals were annealed at 580 °C in 0.5% oxygen in argon to get an oxygen concentration of $YBa_2Cu_3O_{6.45}$.

Aligning The sample batch used for this experiment was a 650mg silicon plate with 2000mg of $YBa_2Cu_3O_{6.45}$ crystals all co-aligned.

4.3 Previous neutron scattering data of cuprates in magnetic field

Many cuprate superconductors have been probed with neutron scattering. Despite sharing common features, they also exhibit differences, so that different cuprate sample can reveal different information about the spin mechanism. Previous data of various cuprates will be cited, however the sample used for this work is a $YBa_2Cu_3O_{6.45}$ sample.

4.3.1 Competition between SDW and superconductivity in optimally doped La_2CuO_{4+x}

Connection and competition between SC and SDW The compound La_2CuO_{4+x} is a cuprate superconductor where superconductivity is reached via excess oxygen doping. In optimally doped $La_2CuO_{4.11}$ static SDW order can be found with a correlation length of at least 300 Å in plane and 13 Å out of plane. Curiously, the superconducting temperature and the onset of two-dimensional static SDW are the same $T_c = T_m = 42$ K. This suggests that the have some common roots, which is in contrast to $La_{2-x}Sr_xCuO_4$:Nd where superconductivity and SDW appear to compete.

On the other hand it was found that in a magnetic field of 7.5 T the intensity of the static SDW at the quartet $(1 \pm \delta, \delta, 0)$ nearly doubles [Kha02] (Fig. 4.2). whereas T_c is reduced in magnetic field by ~ 10 K as expected. Therefore $T_c \approx T_m$ is only valid in zero field. A similar coincidence has been observed in more lightly doped La_2CuO_{4+x} ($T_c = 34$ K).

The magnetic field dependence of the SDW intensity seems to be linear up the highest field measured 9 T which suggests that the effect originates from magnetic flux lines penetrating the sample.

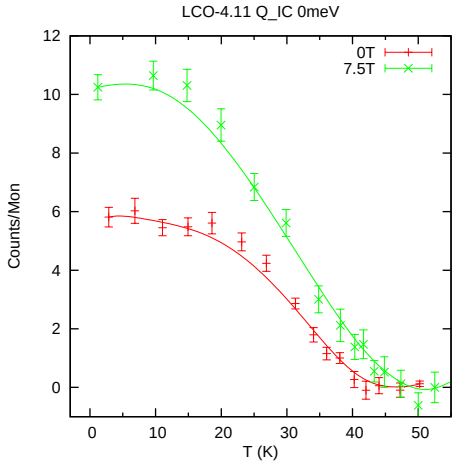

Figure 4.2: Elastic, incommensurate neutron scattering intensity as function of temperature in low and high magnetic field in $La_2CuO_{4.11}$: onset of SDW and enhancement with magnetic field [Kha02]

Spatial phase separation μSR measurements estimated that only 40% of the sample (sample 2 in reference) experience the internal magnetic field, which - as noted by the authors - is close to the percolation limit in 2D. As the μSR measurements show an abrupt change at T_c (contrary to $La_{2-x}Sr_xCuO_4$:Nd), the authors suggest that at T_c a microscopic phase separation [Kiv01] into magnetic regions of the order 15-50 Å occurs.

A second sample with equal mass prepared under identical conditions was examined. The SDW order turned out to be weaker just as the enhancement in magnetic field. Assuming a separation into non-superconducting and SDW regions and the assuming that the magnetic field enhances SDW only in the non-superconducting samples, the authors could predict the scaling relation between SDW strength and field enhancement between both samples.

4.3.2 Field induced SDW in $La_{1.856}Sr_{0.144}CuO_4$

In the cuprate superconductor $La_{2-x}Sr_xCuO_4$ spin excitations at low energies can be seen most clearly. In $La_{2-x}Sr_xCuO_4$ for low doping $x \leq 0.13$ static SDW order is observed whereas for high doping $x > 0.15$ a suppression of the scattering intensity in the spin gap 4 meV to 8 meV depending on x is identified.

Experiments on the intermediate doping $La_{1.856}Sr_{0.144}CuO_4$ showed that above a critical field of 3 T static SDW order is induced with an ordered moment of $0.06\mu_B$ at 14.5 T Fig. 4.3. A theoretical phase diagram explaining the dependence of superconductivity and SDW on magnetic field and the possibility of their coexistence has been proposed in [Dem01, Kiv02].

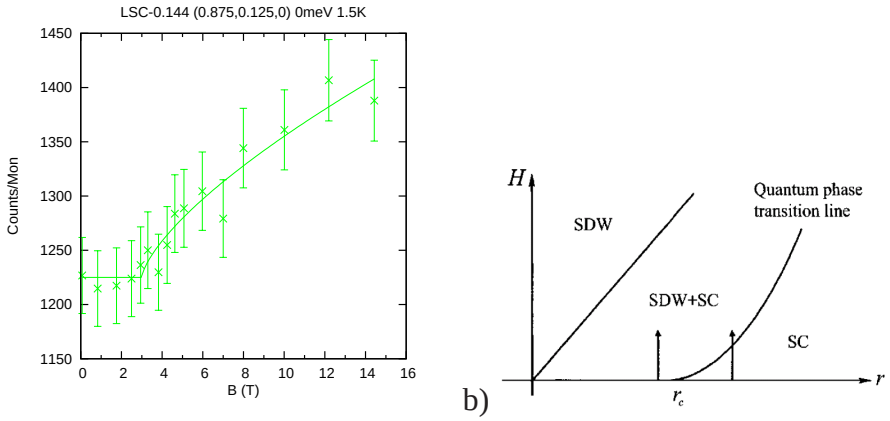

Figure 4.3: a) Elastic magnetic intensity at the incommensurate signal maximum as function of magnetic field B in $La_{1.856}Sr_{0.144}CuO_4$: induced static SDW wave order [Kha05]; b) Theoretical phase diagram with repulsive coupling r and magnetic field H [Dem01, Kiv02]

4.3.3 Three-dimensionality of field-enhanced order in $La_{1.9}Sr_{0.1}CuO_4$

In underdoped $La_{1.9}Sr_{0.1}CuO_4$ an applied magnetic field enhances the static incommensurate signal. It was also found that this order is inter-plane correlated as for (1.12,0.12,4) (i.e. $L = 4$) a magnetic field of 6 T also enhances the order whereas for non-integer L a signal, but not the field enhancement is seen [Lak05]. The estimated correlation length of the integer L signal is about 6 CuO_2-planes along the c-axis direction, which suggests that the two-dimensional pancake vortices created by the magnetic field are stacked on top of each other.

The authors attribute this signal to the motion of electron, rather than their spin, as the spin susceptibility measured by NMR is isotropic, unlike the effect of the magnetic field which is effective only applied along the c-axis.

4.3.4 In-gap excitations in optimally doped $La_{1.837}Sr_{0.163}CuO_4$

Subgap excitations with cores Without magnetic field, $La_{1.837}Sr_{0.163}CuO_4$ has a spin gap in the superconducting state at low energies, i.e. the intensity below 6.7 meV is strongly suppressed upon entering the superconducting state $T < T_c$. The spin gap below 6.7 meV acquires in-gap excitations which peak at 4 meV when 7.5T are applied Fig. 4.4a [Lak01]. The intensity is roughly the same as the ungapped normal state, despite the fact that vortices occupy only 12% of the sample ($H_{c2} \approx 62$T [And99b]) at this magnetic field. For the origin of the sub-gap excitations the authors suggest fluctuating antiferromagnetic regions within the vortex cores, which corresponds well with the estimation of the 2D Heisenberg antiferromagnetic multiplied by the volume ratio of the vortices. However, to account for all observations a more complicated

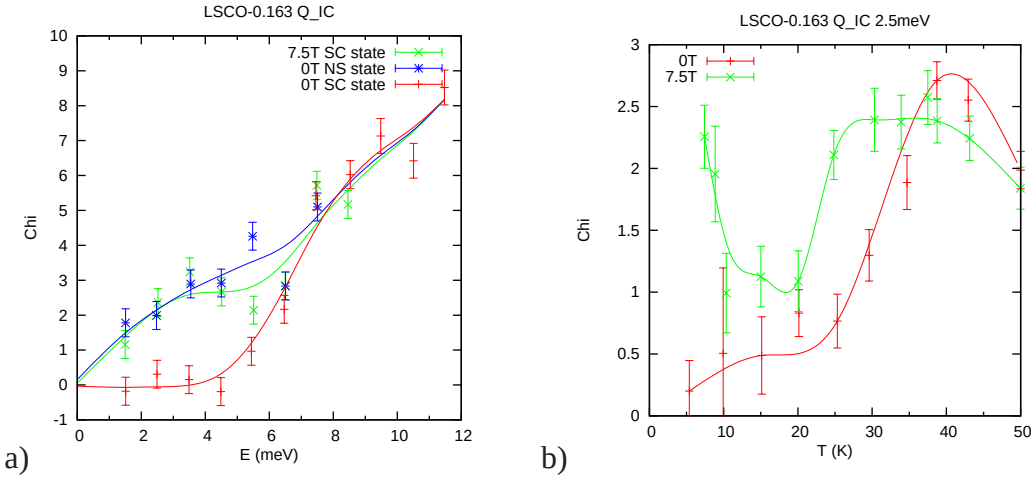

Figure 4.4: Magnetic susceptibility at the incommensurate position in zero field and high magnetic field, both in the superconducting state and normal state in $La_{1.837}Sr_{0.163}CuO_4$ [Lak01]; a) E-scan showing closing of spin gap at 7.5T; b) T-dependence of the spin susceptibility at 2.5 meV showing induced intensity at intermediate temperatures due to released vortex pinning

picture has to be invoked where vortices should be highly anisotropic objects with inter-vortex correlations.

Sharpness due to elastic origin The very sharp Q-width measured at 2.5 meV in the superconducting state indicates that the signal is coherent over at least 20 units cells, whereas in-gap filling excitations in the normal state correspond to a coherence length of 6.3 only [Lak99]. The sub-gap weight of the induced spectrum corresponds to a spin $1/2$ Heisenberg antiferromagnet, so that seemingly the elastic moment becomes a fluctuating sub-gap peak. No other changes above the spin-gap or at other energies where detected in this experiment.

Vortex pinning The temperature dependence of the signal as shown in Fig. 4.4b shows that the peak intensity is reduced below 25K. This was attributed to vortex pinning below this temperature. Whereas at higher temperatures the moving vortices affect a large part of the sample, the pinned vortices influence an area proportional to H/H_{c2}. Therefore, the number of sites contributing to sub-gap excitations become relatively small. The increase of the intensity below 10K was attributed to a change in the inter-vortex spin interactions.

4.3.5 Spin-gap closing in underdoped $La_{1.9}Sr_{0.1}CuO_4$

Closing of the spin gap with magnetic field Neutron scattering experiments with a magnetic field of 10T were performed on underdoped $La_{1.9}Sr_{0.1}CuO_4$ ($T_c = 30$ K,$H_{c2} =$

45T [And99b]) [Cha07a]. The sample shows incommensurate peaks at $Q_{IC} = (0.5, 0.5, 0)\pm(\delta, 0, 0)$ and $Q_{IC} = (0.5, 0.5, 0) \pm (0, \delta, 0)$. The main novel result was that a spin gap was identified below 1.5 meV, which closes upon application of magnetic field (Fig. 4.5a). The spin gap opening however is incomplete down to lowest temperatures. With the magnetic field the gap is filled to reproduce its normal state shape, just as the spin gap is closed upon heating above T_c.

Vortex liquid state Additional SANS and μSR measurements indicate that, unlike the well-ordered vortex lattice in optimally doped $La_{1.84}Sr_{0.16}CuO_4$, here the vortex liquid phase dominates the magnetic phase diagram, while a quasi-long-range ordered vortex lattice is only observed at low temperatures and low fields [Div04]. The induced intensity seen in Fig. 4.5b was attributed to the liquid vortex temperature range and thus induced excitations inside vortex cores. One more observation is that the magnetic field shifts and broadens the cusplike anomaly at T_c.

Sub-linear magnetic field dependence of the elastic signal The intensity of the elastic magnetic signal at Q_{IC} could be fitted with a sub-linear theoretical prediction [Dem01] $I \propto \frac{H}{H_{c2}} \ln \frac{H_{c2}}{H}$. The inelastic response exhibits a similar field dependence.

Two-component model The authors propose a two-components model, where one component is responsible for the gapped response seen around optimal doping. The second quasi-elastic component could be related to the slowing down of the magnetic signal observed by μSR [Nie98] and the central mode in $YBa_2Cu_3O_x$ [Sto06]. An additional idea identifies these contributions as static and fluctuating stripes.

4.3.6 Enhanced static SDW order in underdoped $La_{1.9}Sr_{0.1}CuO_4$

Enhanced static signal Elastic neutron scattering on $La_{1.9}Sr_{0.1}CuO_4$ indicated an enhancement of the elastic signal with magnetic field [Lak02]. The field-induced intensity increases at 2 K at Q_{IC} manifests itself in a strong and very sharp peak Fig. 4.6a.

Inter-vortex correlations The peak is resolution limited and corresponds to a correlation length of $\xi \sim 400$ Å, which is larger than the size of the vortex cores and the inter-vortex spacing $a = 130$ Å. At higher temperatures around T_c there is no effect of the magnetic field. The induced signal originating from a static spin structure corresponds to approximately 50% of the volume fraction of the ordered phase, assuming that the sample if $0.4\mu_B$ as found by μSR.

Temperature and field dependence The temperature dependence is shown in Fig. 4.6b. In field the temperature dependence is clearly different from zero-field and shows

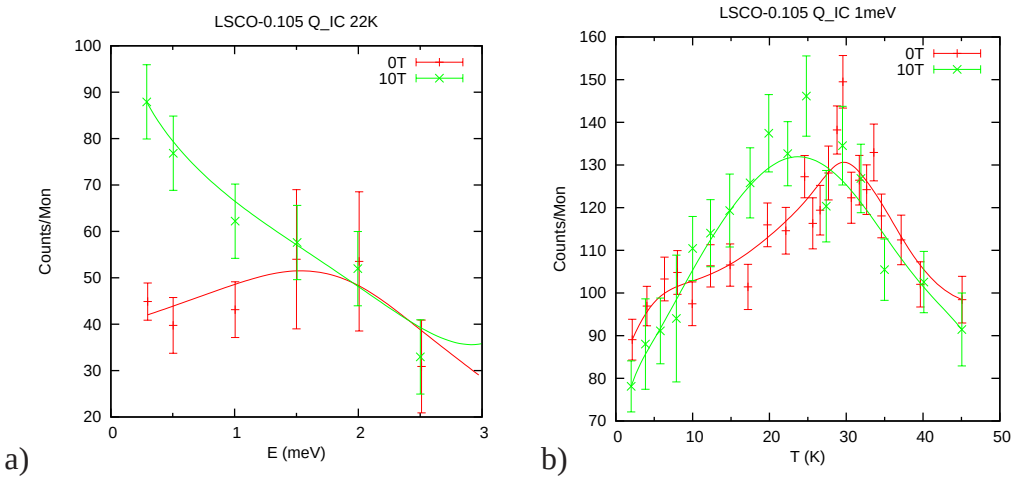

a) b)

Figure 4.5: Magnetic spin excitation intensity in zero field and high magnetic field in $La_{1.9}Sr_{0.1}CuO_4$ ($T_c = 30\,K$) at low energies and low temperature [Cha07a]; a) E-scan showing closing of spin gap at 10T ; b) T-dependence showing induced intensity at intermediate temperatures from a liquid vortex region

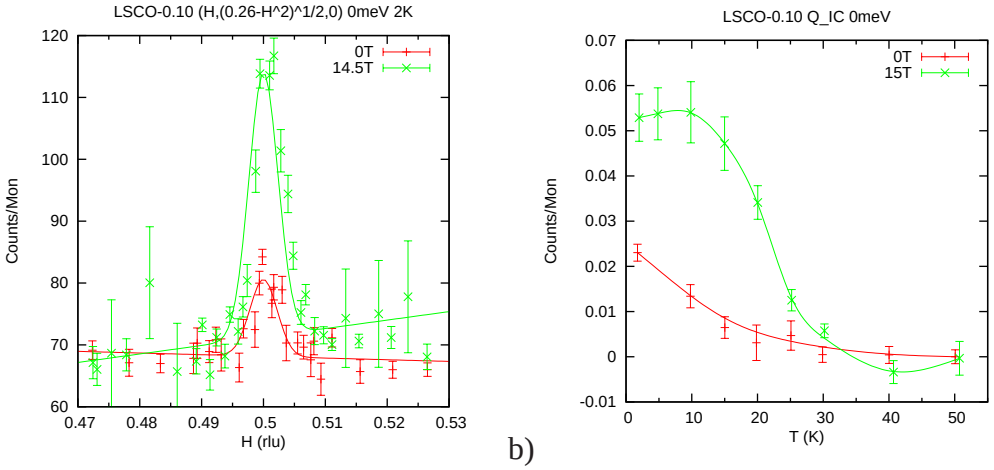

a) b)

Figure 4.6: Elastic neutron scattering intensity in zero field and high magnetic field in $La_{1.9}Sr_{0.1}CuO_4$ ($T_c = 29\,K$) [Lak02]; a) Q-scan showing the incommensurate wing of the field-induced elastic signal; b) T-dependence of the field-induced elastic signal

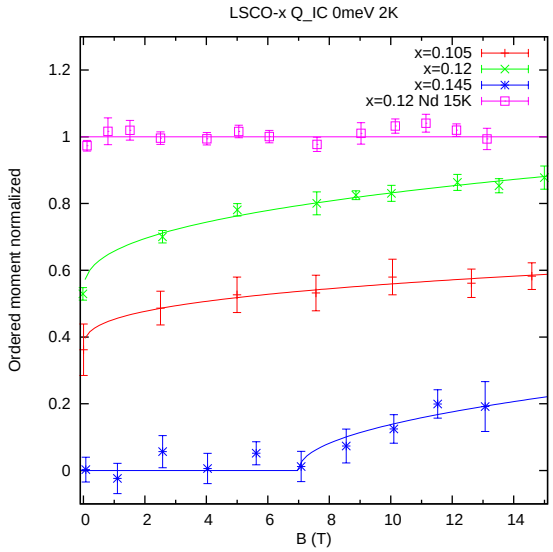

Figure 4.7: Ordered magnetic moment as a function of magnetic field B estimated from μSR normalized to the moment in the stripe-ordered state [Cha07b]

a saturation at $T < 10\,\mathrm{K}$. The field dependence at the lowest temperature shows a sub-linear increase. The temperature dependence of the field-induced signal indicates that the antiferromagnetic contribution disappears as soon as the normal state is entered.

Driving towards 1/8 state It is interesting to note, that in $La_{1.48}Nd_{0.4}Sr_{0.12}CuO_4$ at 1/8 doping where in zero field the strongest in-gap excitations are already observed, a magnetic field of 10 T shows *no further enhancement* [Cha07b]. On the other hand, cuprates away from the 1/8 phase do show field enhanced signals. In a field of 12 T, $La_{1.55}Sr_{0.145}CuO_4$ has induced incommensurate excitations above the critical field of 7 T ($\xi \sim 45$ Å), $La_{1.88}Sr_{0.12}CuO_4$ shows enhanced incommensurate excitations ($\xi \sim 70$ Å) and $La_{1.895}Sr_{0.105}CuO_4$ also shows enhanced incommensurate excitations ($\xi \sim 28$ Å) in magnetic field (Fig. 4.7).

Therefore, it was suggested that both magnetic field and impurities drive the system towards stabilization of the 1/8 phase. The authors suggest that this is consistent with the existence of an incommensurate SDW state [Sav02, Le93].

4.3.7 Magnetic field effect in $YBa_2Cu_3O_{6.6}$

The $YBa_2Cu_3O_{6.6}$ spin spectrum has a resonance mode at (0.5,0.5,1.7) at 34 meV which, due to the correlation with T_c, is thought be connected with superconductivity.

Suppression of resonance by magnetic field It was found that the resonance mode in $YBa_2Cu_3O_{6.6}$ 34 meV is suppressed by even a moderate magnetic field of 6.8T [Dai00].

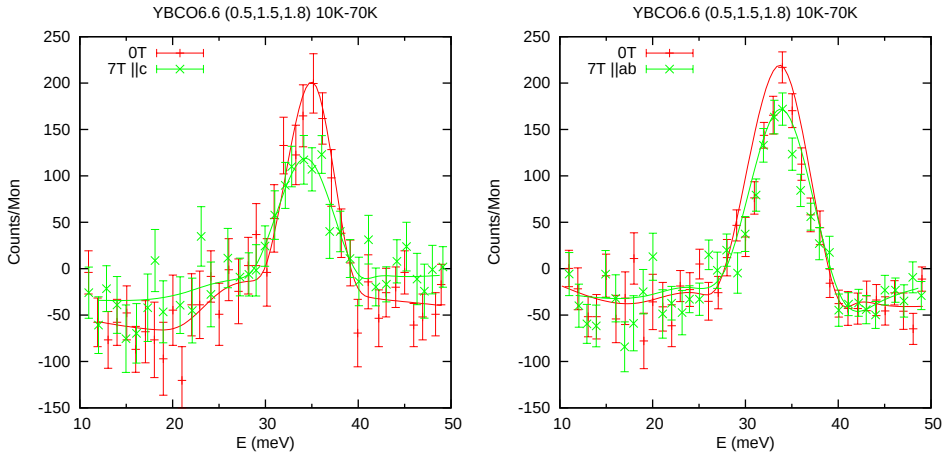

Figure 4.8: Difference of low temperature and high temperature neutron scattering intensity at Q_{AF} as function of energy around E_{res} in zero field and 7 T along c and in the ab-plane in $YBa_2Cu_3O_{6.6}$ [Dai00] showing the field-suppression of the signal

A field applied parallel to the c-axis reduces the peak intensity by 30% at low temperature Fig. 4.8a. This corresponds roughly to the estimation by the classical volume fraction reduction of the superfluid density between the magnetic vortices $1 - B/B_{c2}$. In the normal state at 70 K the effect is very small, which was attributed to preformed pairs above T_c. At the even higher temperature of 150 K there is no magnetic field effect at E_{res}. The Q-width is unchanged by magnetic field at all temperatures. It was found earlier that a field of 11.5T when applied in the ab-plane has no effect on the spectrum of optimally doped $YBa_2Cu_3O_{7.0}$ [Bou97] At 150K the magnetic field did not produce intensity differences between 0T and 6.8T.

Magnetic field effects at lower energies At 24 meV where an incommensurate magnetic signal is observed, the magnetic field suppresses the intensity in both the superconducting and the normal state (Fig. 4.9b).

Apart from the reduction of the resonant contribution, no additional changes in the spectrum at energies above the resonance or below the energy gap were detected.

4.4 Magnetic field effect in $YBa_2Cu_3O_{6.45}$

To determine the field effect in strongly underdoped $YBa_2Cu_3O_{6.45}$, neutron scattering measurements with a magnetic field of 14.9T were performed. Without magnetic field this compound shows an incommensurate signal (0.5±δ,0.5,1.7) at elastic and quasi-elastic energies. Measurements on IN14 with $k_f = 1.5\,\text{Å}^{-1}$ reproduced this signal. No collimators were used and a beryllium filter extinguished higher order contaminations on k_f. The scattering plane in this experiment was (1,0,0)×(0,0.5,1.0) in order to reach

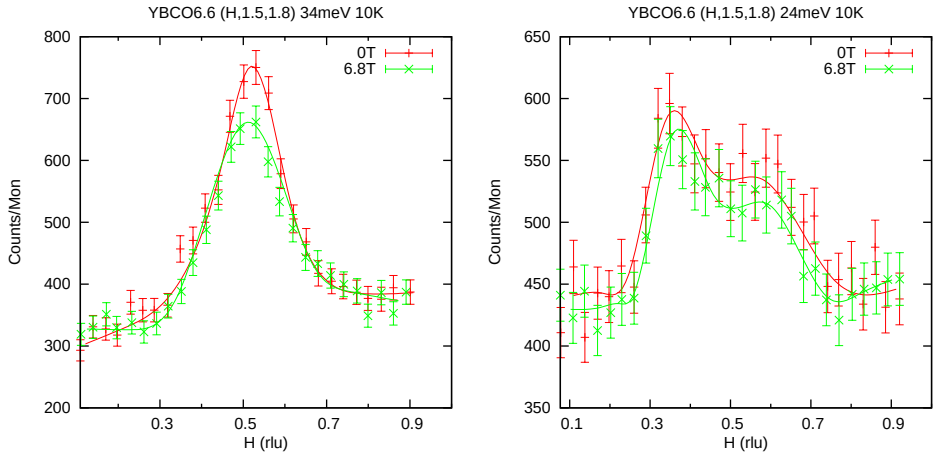

Figure 4.9: Neutron scattering Q-scan in zero field and high magnetic field at 34 meV and 24 meV in $YBa_2Cu_3O_{6.6}$ [Dai00] showing the field-suppression of the signal

(0.5,0.5,1.0). Note that the L value does not correspond to the maximum of the bilayer modulation ($L = 1.7$), however at this L the bilayer modulation does not vanish yet.

This geometry requires the *ab*-plane to be tilted by 33° out of the scattering plane. At the same time that is the angle between the magnetic field and the c-axis. Ideally, the magnetic field would be parallel to the c-axis, as that is where the strongest effect is expected. However, due to experimental constraints this was not possible here. Effectively the field is reduced to 12.6 T along the c-axis. ab-plane components of the magnetic field are not thought to influence the spectrum.

Magnetic field enhanced static signal The effect of the magnetic field is shown in Fig. 4.10. Repeating the same elastic scan with and without field reveals an enhanced incommensurate signal with an incommensurability $\delta \sim 0.06$. In agreement with prior data in $YBa_2Cu_3O_{6.45}$ [Hin08], scans taken at temperatures below 30 K for $H = 0$ T in this configuration show a small incommensurate signal with amplitude $\sim 0.05\mu_B$ per planar Cu site at $T = 2$ K, estimated from μSR measurements on the same sample [Hin08]. In order to obtain a quantitative description of the evolution of the incommensurate spin modulation with H, the data were fitted to Gaussian profiles. Neither the resolution corrected peak width (0.09 r.l.u.) not the incommensurability (0.049 at $H = 0$, 0.055 at $H = 14.9$ T) vary with H outside the experimental error. However, the integrated intensity of the elastic peak extracted from these fits increases continuously with H. At $H = 14.9$ T, it is about a factor two larger than the zero-field intensity. This signal is assumed to be one-dimensional as previously has been shown in zero-field measurements [Hin08]. In the normal state the magnetic field has no effect on the neutron scattering data.

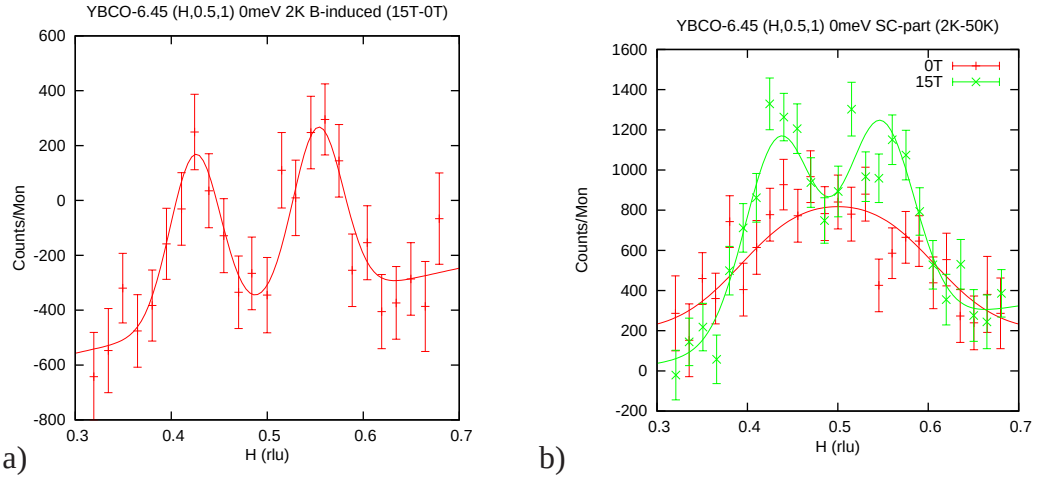

Figure 4.10: Field effect on elastic signal in $YBa_2Cu_3O_{6.45}$; a) Difference between high field and zero field Q-scans; b) Difference between low temperature and high temperature Q-scans in zero field and high magnetic field

Finite size domain origin of the static signal Previous neutron scattering experiments demonstrated that the spin system in the CuO_2-planes is unstable towards the formation of one-dimensional, slowly fluctuating spin structures [Hin08]. Correspondingly, subsequent μSR measurements on this sample in zero field suggest that the field-dependent, quasi-static spin modulation found is the result of spin freezing into finite-size domains, in analogy to the findings in $La_{2-x}Sr_xCuO_4$ [Cha07b]. These measurement estimate the order Cu moment to be $\sim 0.05\mu_B$ which is roughly 10% of the moment in the parent antiferromagnetic compound $YBa_2Cu_3O_{6.0}$.

The $La_{2-x}Sr_xCuO_4$ compound with the same hole doping as our $YBa_2Cu_3O_{6.45}$ sample, has $\sim 0.12\mu_B$. The discrepancy is not surprising, as the pronounced 1/8 anomaly, which is close to the hole doping examined here, is found in $La_{2-x}Sr_xCuO_4$ but is not present in the $YBa_2Cu_3O_x$ compound. At this hole doping $p = 0.125$ the compound $La_{2-x}Sr_xCuO_4$ exhibits the largest ordered moment and correlation length (sharp peaks in the signal).

Field dependence of induced signal A property which can possibly be compared to theoretical predictions is the field dependence of this induced signal. This dependence of the elastic signal in $YBa_2Cu_3O_{6.45}$ is shown in Fig. 4.11. Based on an extrapolation of the intensity of the incommensurate elastic peak of $YBa_2Cu_3O_{6.45}$ to 50 T, we estimate an ordered moment of $\sim 0.13\mu_B$, which is comparable the the value observed in the fully established stripe-ordered state in Nd-substituted $La_{2-x}Sr_xCuO_4$ [Cha08b].

Suppression of inelastic excitations The total moment sum rule for the scattering function stipulates that the spectral weight integrated over all energies and momenta is conserved. This implies that the amplitude of the inelastic response has to decrease in

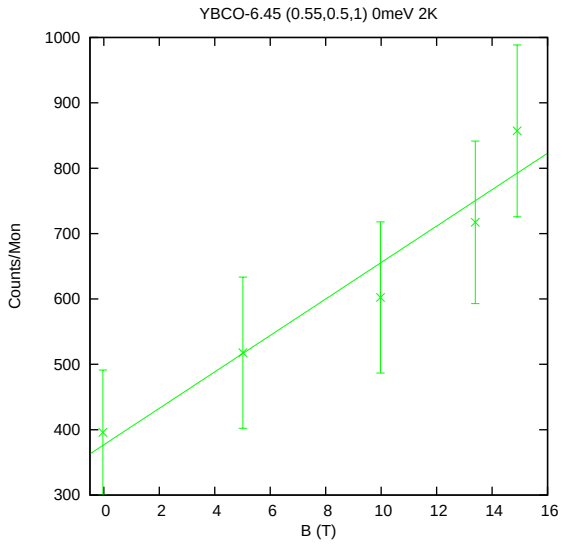

Figure 4.11: Elastic neutron scattering intensity as function of magnetic field B at the incommensurate peak position Q_{IC} in $YBa_2Cu_3O_{6.45}$

order to compensate for the spectral weight accumulated in the elastic peak. We have therefore studied the effect of the external magnetic field on the low-energy spin excitations. The results are summarized in Fig. 4.12. For an excitation energy $E = 3\,\mathrm{meV}$, the spin fluctuation intensity decreases appreciably at $H = 14.9\,\mathrm{T}$, while the shape of the scattering profile remains unaffected. A comparison of integrated intensities indicates that the reduction in the energy range covered by our experiment accounts for roughly half of the gain in elastic intensity with increasing H.

4.5 Summary of magnetic field effects on cuprates

To sum up, the electronic structure of vortices in various cuprates has been examined in the scientific community with the following main observations at low temperatures and field along the c-axis:

- $La_2CuO_{4.11}$: concomitant onset of phase separated SDW and SC at T_c in zero field; in field SDW enhanced and SC suppressed; spatially separated
- underdoped $La_{1.9}Sr_{0.1}CuO_4$: interlayer-correlated SDW enhanced in magnetic field; range beyond inter-vortex distance; gap-closing with magnetic field; two components (gapped + quasi-elastic)
- underdoped $La_{1.56}Sr_{0.144}CuO_4$: SDW order induced above 3 T
- optimally doped $La_{1.837}Sr_{0.163}CuO_4$: in-gap long-range excitations from vortex cores

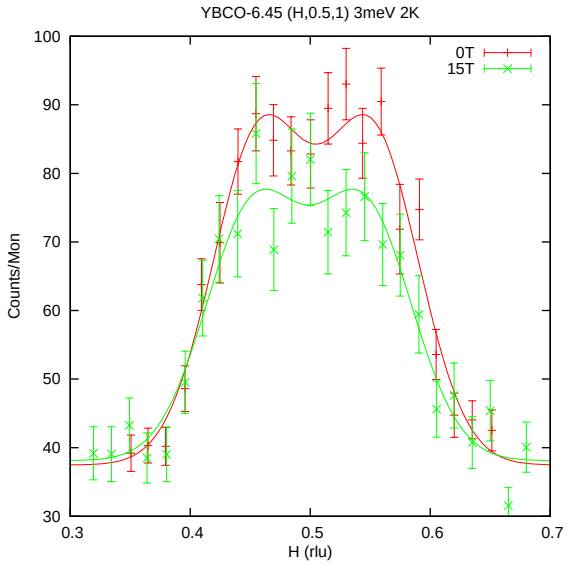

Figure 4.12: Magnetic excitations around Q_{AF} Q-scan at 3 meV in zero field and at 15 T in $YBa_2Cu_3O_{6.45}$

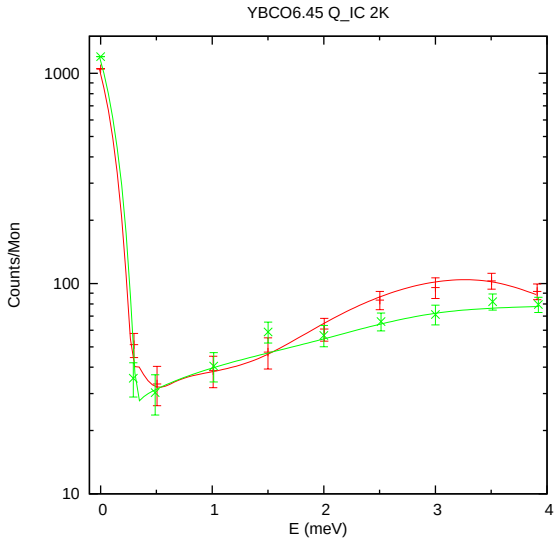

Figure 4.13: Energy dependence of the magnetic peak intensity at the incommensurate position (0.56,0.5,1) in zero field and in $H = 13.5$ T, corrected for the background; Note the logarithmic intensity scale

- 1/8 doping $La_{2-x}Sr_xCuO_4$:Nd: no magnetic field effect
- spin gap in cuprate scales as $\Delta_{sg} \propto T_c$
- underdoped $YBa_2Cu_3O_{6.6}$: suppression of resonance according to superfluid suppression
- underdoped $YBa_2Cu_3O_{6.45}$: enhanced (factor 2), finite-size static SDW; no change in peak width or incommensurability
- underdoped $YBa_2Cu_3O_{6.45}$: suppressed inelastic, incommensurate signal
- optimally doped $YBa_2Cu_3O_{7.0}$: quasi-particle states near cores at 5.5 meV (STM); 4x4 checkerboard modulation beyond vortex
- $Bi_2Sr_2CaCu_2O_x$: quasi-particle states near cores at 7 meV (STM); 4x4 checkerboard modulation beyond vortex; both of same origin

Obviously the static finite-size SDW order measured with neutron scattering can be connected with the observed checkerboard modulation found with STM. Once discrepancy however is the one-dimensional nature observed in neutron scattering which is not easily extracted from the STM results.

It was shown that the low-energy peaks at the vortex cores found with STM are closely connected with this checkerboard modulation. An indication that vortex core state in all cuprates have a common origin is given by a linear scaling relation between the core state energy E_{core} and the superconducting gap amplitude Δ_p (Fig. 4.14) [Fis07].

$$E_{\text{core}} \sim 0.3\Delta_p$$

4.6 Interpretation of magnetic field effect in cuprates

Field-enhanced static order in $YBa_2Cu_3O_{6.45}$ The magnetic field enhanced elastic incommensurate signal is common to both underdoped $YBa_2Cu_3O_x$ and $La_{2-x}Sr_xCuO_4$. This field dependent static order could introduce a superstructure modulation in the magnetic properties. Interestingly, this idea is supported by the discovery of quantum oscillations at 50 T in $YBa_2Cu_3O_x$ $x \sim 0.5$ [DL07, LeB07, Jau08]. The electron and hole pockets deduced from the quantum oscillation experiments could not be detected by (zero-field) ARPES [Hos08, Zab07] or ab-initio band structure calculations [Car07, Kro08], however the superstructure - such as suggested by the incommensurate excitations - at high magnetic field could lead to additional scattering and thus reconstruction of the Fermi surface. Although the incommensurate excitations are already present at zero field below ~150 K, their strength is probably not sufficient for

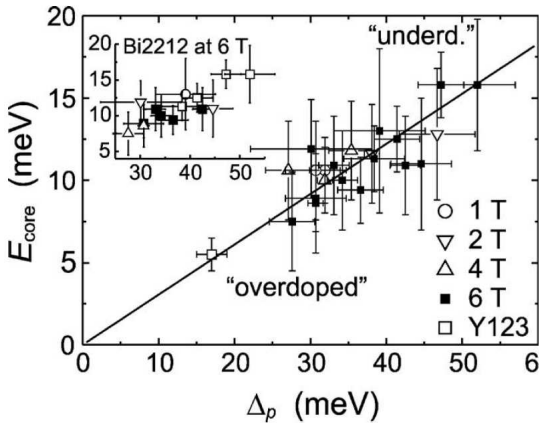

Figure 4.14: Vortex core state energy E_{core} as function of superconducting gap Δ_p [Fis07]; $Bi_2Sr_2CaCu_2O_x$ crystals of various doping and $YBa_2Cu_3O_x$ at optimal doping

the Fermi surface reconstruction and only the field-enhancement establishes their effectiveness. Moreover the μSR data show real static magnetic order only below 2 K. Corresponding field-induced commensurate and incommensurate [Dim08] spin modulations as well as striped [Mil07] and *d*-density-wave [Cha08a] have been suggested as explanations of the small Fermi surface pockets. The field-enhancement of the static signal is in agreement with theoretical work on incommensurate SDW order competing with *d*-wave superconductivity [Dem01].

Whereas in $YBa_2Cu_3O_{6.45}$ the field dependence of the static magnetic intensity shows a steady increase up to the highest fields measured 14.5 T, in $La_{2-x}Sr_xCuO_4$ a saturation of the magnetic moment is observed when the amplitude reaches $\mu \sim 0.2\mu_B$ [Lak02]. However, this discrepancy is not surprising, as the magnetic moment in $YBa_2Cu_3O_{6.45}$ is estimated to be $\sim 0.07\mu_B$ at 14.5 T. The estimation for the ordered moment at 50 T is $\sim 0.13\mu_B$, which is comparable to the value observed in the fully established stripe-ordered state in Nd-doped $La_{2-x}Sr_xCuO_4$ [Cha08b].

Therefore the field-enhancement of static order is common to many cuprates. The magnetic field favours antiferromagnetism and destroys superconductivity.

Field-suppressed inelastic incommensurate excitations in $YBa_2Cu_3O_{6.45}$ The field suppression of the inelastic incommensurate excitations in $YBa_2Cu_3O_{6.45}$ is most pronounced at 4 meV, however due to experimental restrictions a stronger suppression at even higher energies could not be excluded. Although a clear resonance mode behaviour could not be detected in $YBa_2Cu_3O_{6.45}$, it is possible that a resonance mode contribution shifted to low energies is responsible for the field-induced reduction of the magnetic signal - similarly to what has been observed for the resonance mode in $YBa_2Cu_3O_{6.6}$. Despite the fact that the maximum of the resonance mode in $YBa_2Cu_3O_x$ is at the commensurate AF wavevector Q_{AF}, the magnetic field effect on incommensu-

rate excitations is not in contradiction to these interpretations as a weak magnetic field suppression can also be detected in $YBa_2Cu_3O_{6.6}$ at energies below E_R where the signal is incommensurate.

The field suppression effect at inelastic energies is not observed in $La_{2-x}Sr_xCuO_4$, where the inelastic signal is generally enhanced [Cha07a, Tra04a, Lak01], however, neither a clear indication of a resonance mode is found in that compound.

Consequently, there are indications that there remains a resonance contribution in $YBa_2Cu_3O_{6.45}$ at low energies, however, it cannot be identified by the characteristic temperature dependence typical for the resonance feature.

Stripe pinning Similarly to zinc substitutions, it was proposed from thermal conductivity measurements [Kud04, Kaw05] that vortices can create static order by pinning a fluctuating stripe phase,

Disorder-enhanced static order Not only impurities, but also the application of a magnetic field and the resulting vortices can be thought of as a source of disorder in the CuO_2-planes. A corresponding theory for the disorder-induced static order in a *d*-wave superconductor has been presented in [And07]. The authors introduce a disorder potential into the Hubbard model and conclude that a novel magnetic state is induced. In $La_{2-x}Sr_xCuO_4$ large intrinsic disorder is present in zero-field due to the Sr dopant ions being only 2.4 Å away from the CuO_2-plane. This large disorder is possibly the reason why magnetic field induced effects are stronger and more clear in $La_{2-x}Sr_xCuO_4$ as compared to the cleaner compound $YBa_2Cu_3O_x$ where the oxygen dopants can order into chains avoiding disorder. It was proposed that the intrinsic disorder is responsible for stabilizing the static order in zero-field in $La_{2-x}Sr_xCuO_4$ [Lak02].

Consequently, disorder from magnetic field can enhance a static magnetic structure, similarly to the effect of zinc substitutions.

Chapter 5

Conclusions

Several aspects are common between the application of a magnetic field and the substitution by zinc impurities.

Recovery of normal state Both perturbations suppress the superconducting transition temperature. The suppression by magnetic field is well understood theoretically from the conventional phenomenological theory. On the other hand the large magnitude of the suppression by zinc is surprising at first. The resolution lies in the observation that zinc impurities affect a region in the CuO_2-plane considerably larger than the impurity site alone. It was indicated that this region adopt the normal state properties, similar to the interior of a vortex core created by a penetrating magnetic field. These normal state regions seem to share a common characteristic electronic structure. A distinct feature is the linear suppression of T_c with Zn content, which should be reproduced by theoretical approaches.

Electronic structure around perturbation With STM measurement that can resolve the static local structure, quasi particle states at the zinc impurities and at vortex cores were found. This suggests that the destruction of the superconducting state should occur in a similar fashion whatever the perturbation is.

A checkerboard modulation was detected around vortex cores which extends beyond the vortex dimensions. With neutron scattering, the enhancement of static magnetic order has been observed in $La_{2-x}Sr_xCuO_4$ and in this work similarly for $YBa_2Cu_3O_x$. This could possibly be related to the real space modulation observed with STM.

The effect due to zinc impurities is similar. Zinc also modifys the electronic structure beyond it's own impurities site and creates a modulation which can be seen as a staggered magnetization with NMR. In $La_{2-x}Sr_xCu_{1-y}Zn_yO_4$ incommensurate, static order is induced. Also, in optimally doped $La_{1.85}Sr_{0.15}Cu_{1-y}Zn_yO_4$ in-gap excitations appear, which indicate inter-impurity correlations. In this thesis one-dimensional, low-energy excitations induced by Zn impurities were detected. They are incommensurate along the a axis and are not affected by T_c. The extension of the electronic structure

modification beyond the perturbation sites and the one-dimensionality was confirmed by STM measurements on $YBa_2(Cu_{1-y}Zn_y)_3O_x$

Therefore theories for the CuO_2-planes should be able to explain how perturbations induce modulated or staggered effects reaching further than expected by the perturbation dimensions. An important experimental fact found in this work is the one-dimensionality of the Zn-induced low-energy excitation in $YBa_2Cu_3O_{6.6}$. Theoretical approaches should be able to reproduce this strong anisotropy taking into the small orthorhombicity of that compound.

Inter-plane correlations A magnetic field in underdoped $La_{2-x}Sr_xCuO_4$ and likewise Zn impurities in underdoped $YBa_2Cu_3O_x$ both increase the inter-bilayer correlated signal as was found in this thesis for the latter case. An overall successful theory of the CuO_2-planes should be able to explain how superconductivity-weakening perturbations such as Zn and magnetic field can restore the inter-bilayer correlations.

An important observation is that magnetization properties in underdoped $YBa_2(Cu_{1-y}Zn_y)_3O_x$ are alike for compounds with similar T_c irrespectively of their Zn content and oxygen content. Therefore Zn substitution has partly equivalent effects to the reduction of oxygen doping. A similar observation was made in this thesis for a magnetic field applied on $YBa_2Cu_3O_{6.35}$ and for zinc substitution in $YBa_2Cu_3O_{6.45}$ which both resemble the magnetic spectrum of $YBa_2Cu_3O_{6.35}$. The partial equivalence between Zn substitution, applied magnetic field and oxygen content reduction can guide ideas for theoretical approaches.

Suppression of a resonance mode Both magnetic field and Zn impurities suppress the magnetic resonance. This is not unexpected and many theories have been proposed to account for this observation. On the experimental side, the suppression of intensity in $YBa_2Cu_3O_{6.45}$ due to magnetic field detected in this work is similar to the field-suppression of the magnetic resonance in $YBa_2Cu_3O_{6.6}$. This can indicate the existence of a low-energy-shifted resonance in $YBa_2Cu_3O_{6.45}$ which could not be identified by it's temperature dependence in previous experiments.

Relation to 1/8th phase and stripe ordering The connection between a charge doping level around 1/8 and Zn-substition is drawn from μSR measurements that detected a slowing-down of Cu spins in $YBa_2(Cu_{1-y}Zn_y)_3O_x$ and $La_{2-x}Sr_xCu_{1-y}Zn_yO_4$ at a doping level close to $p = 1/8$. The link between an applied magnetic field and the 1/8th phase can be seen in the observation that the field enhances the static order in underdoped $La_{2-x}Sr_xCuO_4$, however, in $La_{2-x}Sr_xCuO_4$:Nd where the 1/8th phase is thought to be developed strongest the magnetic field effect is absent - similar to a saturation effect.

Therefore the field-induced order, the stripe phase that has been suggested to explain the 1/8 doping effect and Zn-impurities could bear a close relation.

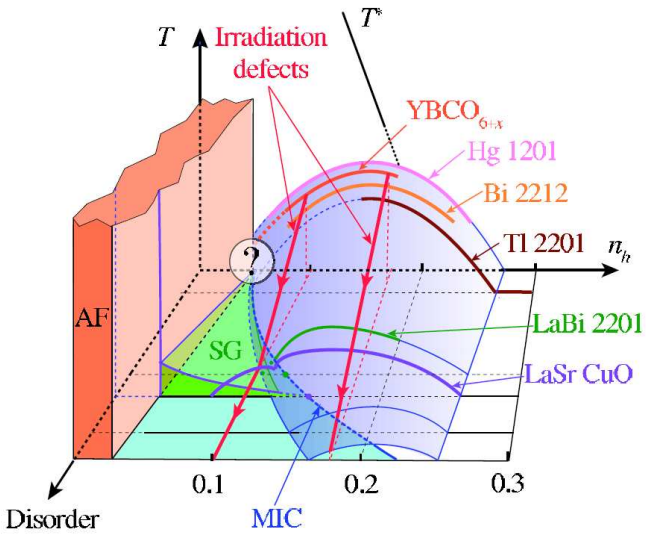

Figure 5.1: Schematic phase diagram for cuprates as function of temperature T, hole doping n_H and disorder; violet is the SC dome; T^* the pseudogap temperature is disorder-independent; green is the spin-glass phase; red lines indicate the effect of increasing disorder [RA08]

Disorder Zinc impurities introduce disorder into the CuO_2-planes and theories have been suggested to theoretically explain the effects of random disorder on the material properties. However, also magnetic field and the resulting vortices can be thought of as a source of disorder and thus has similar effects to zinc impurities substitutions. Normal state in-plane resistivity measurements showed that the doping dependence in $La_{2-x}Sr_xCu_{1-y}Zn_yO_4$ in zero field is similar to that of $La_{2-x}Sr_xCuO_4$ in magnetic field suggesting a common origin for both [Kom04].

Disorder as an additional key parameter for the phase diagram has been proposed in [RA08]. In that work the normal-state resistivity was studied in $YBa_2Cu_3O_x$ with disorder introduced by electron irradiation and superconductivity further suppressed by magnetic field. The authors extract the disorder induced resistivity and show that the magnitude of its low temperature upturn is related to the residual resistivity, that is to the concentration of defects and their nanoscale morphology. Therefore, in various cuprate compounds the disorder-induced resistivity scaled to the extrapolated $T = 0$ resistivity in the pure compound is quantitatively similar. However, quantitative differences arise due to morphology if the impurity sites are driven to form clusters.

The universal effect of disorder in different cuprate compounds suggests disorder as a new universal parameter for the phase diagram (Fig. 5.1) [RA08]. Disorder is introduced as an additional axis and the cuprates are characterized by their intrinsic disorder which is also given by the optimal T_c and the hole content at which a metal-insulator-crossover occurs. Introducing zinc substitutions therefore increases the disorder, which explains why the phase diagram of $YBa_2(Cu_{1-y}Zn_y)_3O_x$ has sim-

ilarities with that of $La_{2-x}Sr_xCuO_4$. Moreover, the zinc induced low-energy excitations in $YBa_2(Cu_{1-y}Zn_y)_3O_{6.6}$ are reminiscent of the low energy incommensurate excitations in $La_{2-x}Sr_xCuO_4$. The lower degree of disorder in pure $YBa_2Cu_3O_x$ than in pure $La_{2-x}Sr_xCuO_4$ may explain why no zinc induced static order has been found $YBa_2Cu_3O_x$.

Disorder could prove to be one of the essential differences between different cuprates compounds and interpretations of experimental data (impurities, magnetic field, ...) can refer to the extended phase diagram when trying to interpret the data.

Outlook Conclusively, the similarity between the effects of the two perturbations suggests that their primary effect is to weaken superconductivity and enhance a state with uniaxial, incommensurate magnetic order that competes with superconductivity. The data reported in this thesis will be helpful in developing a microscopic theoretical description of the competition between these two ordering phenomena and its effects on the macroscopic physical properties of the cuprates.

Appendix A

Units and conversions

eV	thermo (T)	magnetic (B)	light (ν)	light ($\bar{\nu}$)
1 meV	$k_B \cdot$ **11.60** K	$\mu_B \cdot$ **17.28** T	$h \cdot$ **241.8** GHz	$hc \cdot$ **8.066** cm^{-1}
0.08617 meV	$k_B \cdot$ **1** K	$\mu_B \cdot$ **1.489** T	$h \cdot$ **20.84** GHz	$hc \cdot$ **0.6960** cm^{-1}
0.05788 meV	$k_B \cdot$ **0.6717** K	$\mu_B \cdot$ **1** T	$h \cdot$ **14.00** GHz	$hc \cdot$ **0.4669** cm^{-1}
4.136 meV	$k_B \cdot$ **47.99** K	$\mu_B \cdot$ **71.45** T	$h \cdot$ **1000** GHz	$hc \cdot$ **33.36** cm^{-1}
0.1240 meV	$k_B \cdot$ **1.439** K	$\mu_B \cdot$ **2.142** T	$h \cdot$ **29.98** GHz	$hc \cdot$ **1** cm^{-1}
13.6 eV	$k_B \cdot$ **157820** K	$\mu_B \cdot$ **234953** T	$h \cdot$ **3289** THz	$hc \cdot$ **109691** cm^{-1}
23.54 meV	$k_B \cdot$ **273.15** K	$\mu_B \cdot$ **406.6** T	$h \cdot$ **5692** GHz	$hc \cdot$ **189.8** cm^{-1}
25.43 meV	$k_B \cdot$ **295.15** K	$\mu_B \cdot$ **439.4** T	$h \cdot$ **6150** GHz	$hc \cdot$ **205.1** cm^{-1}

Table A.1: Energy conversion

$$1\ \text{meV} = \frac{hc}{\mathbf{0.1240}\text{cm}}$$
$$1\ \text{GHz} = \frac{c}{\mathbf{29.98}\text{cm}}$$

$$1\ \text{kg} = \mathbf{6.242 \cdot 10^{16}}\ \text{eV GHz}^{-2}\text{Å}^{-2} \qquad 1\ \text{eV} = \mathbf{1.602177 \cdot 10^{-19}}\ \text{J}$$
$$1\ \text{m} = \mathbf{10^{10}}\ \text{Å} \qquad 1\ \text{A} = \mathbf{0.624}\ \text{eVT}^{-1}\text{Å}^{-2}$$
$$1\ \text{s} = \mathbf{10^{9}}\ \text{GHz}^{-1} \qquad 1\ \text{V} = \mathbf{10^{11}}\ \text{TÅ}^{2}\text{GHz}$$

$c = \mathbf{29.98}\ \mathrm{cm\,GHz}$

$\hbar = \mathbf{6.582} \cdot \mathbf{10^{-7}}\ \mathrm{eV\,GHz^{-1}}$

$\varepsilon_0 = \mathbf{5.526} \cdot \mathbf{10^{-25}}\ \mathrm{eV\,GHz^{-2}T^{-2}Å^{-5}}$

$\mu_0 = \mathbf{201335}\ \mathrm{T^2Å^3eV^{-1}}$

$e = \mathbf{10^{-11}}\ \mathrm{eV\,GHz^{-1}\,Å^{-2}T^{-1}}$

$k_B = \mathbf{0.08617}\ \mathrm{meVK^{-1}}$

$m_e = \mathbf{5.6856} \cdot \mathbf{10^{-14}}\ \mathrm{eV\,GHz^{-2}Å^{-2}}$

$m_n = \mathbf{1.0454} \cdot \mathbf{10^{-10}}\ \mathrm{eV\,GHz^{-2}Å^{-2}}$

$m_p = \mathbf{1.0440} \cdot \mathbf{10^{-10}}\ \mathrm{eV\,GHz^{-2}Å^{-2}}$

$1\mathrm{u} = \mathbf{1.0364} \cdot \mathbf{10^{-10}}\ \mathrm{eV\,GHz^{-2}Å^{-2}}$

$\frac{\hbar^2}{2m_e} = \mathbf{3.810}\ \mathrm{eVÅ^2}$

$\frac{e^2}{4\pi\varepsilon_0} = \mathbf{14.40}\ \mathrm{eVÅ}$

$\frac{e}{m_e} = \mathbf{175.9}\ \mathrm{GHz\,T^{-1}}$

$\mu_B = \frac{e\hbar}{2m_e} = \mathbf{0.05788}\ \mathrm{meV\,T^{-1}}$

$\frac{2\pi e}{\hbar} = \mathbf{9.546} \cdot \mathbf{10^{-5}}\ \mathrm{T^{-1}Å^{-2}}$

$\Phi_0 = \frac{h}{2e} = \mathbf{206783}\ \mathrm{TÅ^2}$

$\frac{\hbar^2}{2m_n} = \mathbf{2.072}\ \mathrm{meVÅ^2}$

$E_R = \frac{1}{2}\mu(c\alpha)^2 = \mathbf{13.6}\ \mathrm{eV}$

$\mu_N = \frac{e\hbar}{2m_n} = \mathbf{3.1481} \cdot \mathbf{10^{-5}}\ \mathrm{meV\,T^{-1}}$

$a_0 = \frac{\hbar}{\mu(c\alpha)} = \mathbf{0.529}\ \mathrm{Å}$

Appendix B

Glossary

elastic excitation with no energy transfer ($E = 0\,\mathrm{meV}$)

inelastic excitation $E \neq 0\,\mathrm{meV}$

static same as elastic

dynamic same as inelastic

dispersion change of $k_{\max}$ (position of scattering maximum) with energy E

one-dimensional excitations scattering intensity is seen at one particular H only or alternatively no H dependence (or the same statement for K)

1/8th phase special charge doping state (0.125 in LBCO) where superconductivity is suppressed and elastic signals appear

normal state temperature is above the superconducting critical temperature

spin gap energy below which the magnetic signal (at (0.5,0.5)) is suppressed

resolution limited width of signal corresponds to the width a perfect δ signal would give due to instrumental broadening

antiferromagnetic wavevector $Q_{\mathbf{AF}}$ scattering configuration where antiferromagnetic order would give Bragg intensity $\Delta k = (0.5, 0.5, L)$

incommensurate scattering a positions not corresponding to simple fractions of Brillouin zone, i.e. $(0.5 + \delta, 0.5)$

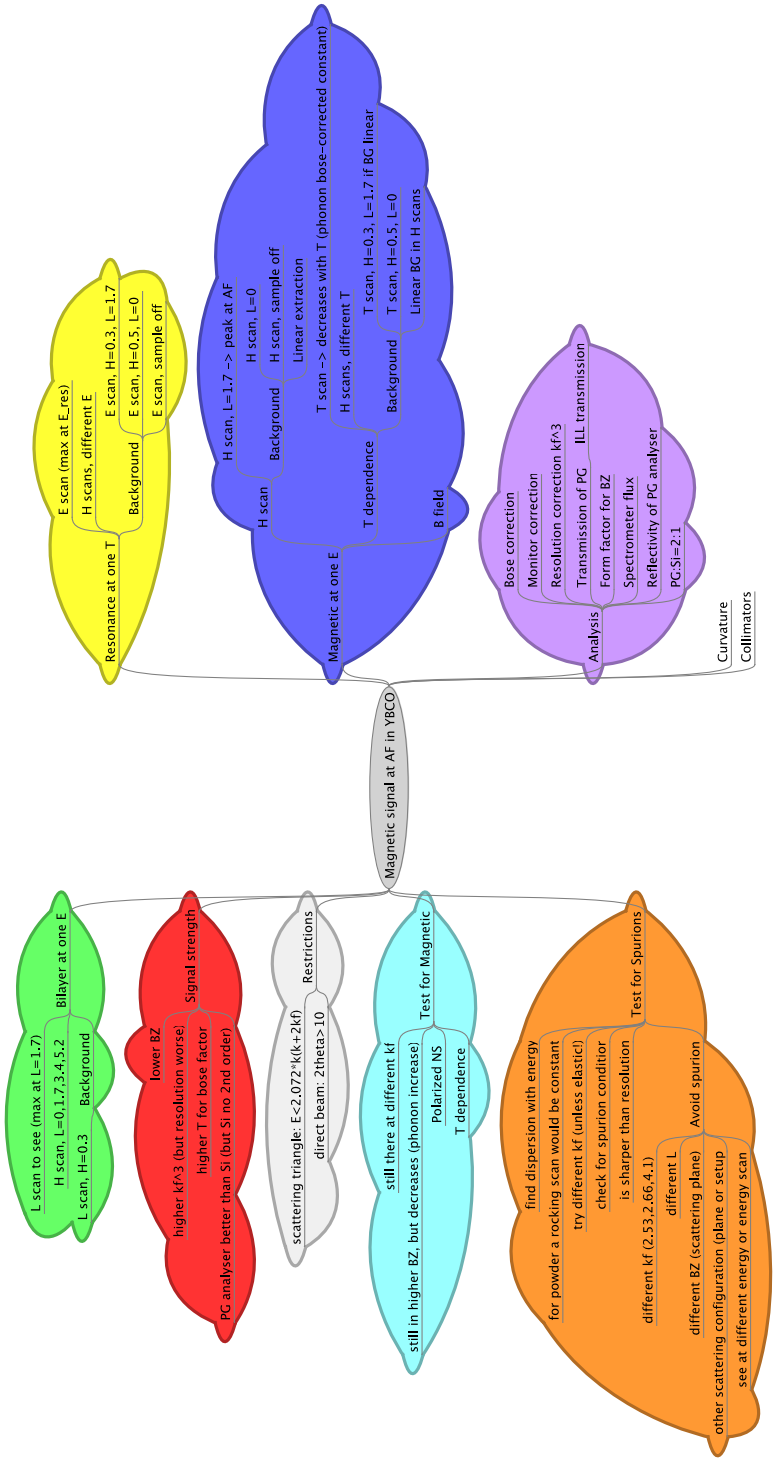

Figure B.1: Experiments to detect a magnetic signal

Index

Bibliography

[Abr98] A. A. Abrikosov: *Phys Rev B* **57**(1998) 8656.

[Ada08] T. Adachi, et al.: *Phys Rev B* **78**(2008) 134515.

[Aga94] S. K. Agarwal, et al.: *Progr Cryst Growth Characterization Mat* **28**(1994) 219.

[Ako98] M. Akoshima, et al.: *Phys Rev B* **57**(1998) 7491.

[Ako00] M. Akoshima, et al.: *Phys Rev B* **62**(2000) 6761.

[All91] H. Alloul, et al.: *Phys Rev Lett* **67**(1991) 3140.

[All07] H. Alloul, et al.: *cond-mat* **0711.0877**(2007).

[And91] H. Andresen, et al.: *Acta Chem Scand* **45**(1991) 698.

[And95] O. K. Andersen, et al.: *J Phys Chem Solids* **56**(1995) 1573.

[And99a] N. Andersen, et al.: *Phys C* **317–318**(1999) 259.

[And99b] Y. Ando, et al.: *Phys Rev B* **60**(1999) 12475.

[And04] P. W. Anderson: *cond-mat* (2004).

[And07] B. M. Andersen, et al.: *Phys Rev Lett* **99**(2007) 147002.

[Ara99] M. Arai, et al.: *Phys Rev Lett* **83**(1999) 608.

[Aro97] D. P. Arovas, et al.: *Phys Rev Lett* **79**(1997) 2871.

[Ass97] F. F. Assaad, et al.: *cond-mat* **9711172**(1997).

[Bal06] A. V. Balatsky, et al.: *Rev Mod Phys* **78**(2006) 373.

[Bar87] R. L. Barns, et al.: *Appl Phys Lett* **51**(1987) 1373.

[Bas96] S. Basu, et al.: *Phys Rev B* **53**(1996) 6406.

[Bat94] B. Batlogg, et al.: *Phys C* **235–240**(1994) 130.

[Bey08] A. D. Beyer, et al.: *cond-mat* **0808.3016**(2008).

[Bir06] R. J. Birgeneau, et al.: *J Phys Soc Jpn* **75**(2006) 111003.

[Bob99] J. Bobroff, et al.: *Phys Rev Lett* **83**(1999) 4381.

[Bob01] J. Bobroff, et al.: *Phys Rev Lett* **86**(2001) 4116.

[Bon94] D. Bonn, et al.: *Phys Rev B* **50**(1994) 4051.

[Bou96] P. Bourges, et al.: *Phys Rev B* **53**(1996) 876.

[Bou97] P. Bourges, et al.: *Physica B* **234-236**(1997) 830.

[Bou98] P. Bourges: *cond-mat* **9901333**(1998).

[Bou00] P. Bourges, et al.: *Science* **288**(2000) 1234.

[Boy07] M. C. Boyer, et al.: *Nature Physics* **3**(2007) 802.

[Bul96] N. Bulut, et al.: *Phys Rev B* **53**(1996) 5149.

[Car64] C. Caroli, et al.: *Physics Letters* **9**(1964) 307.

[Car07] A. Carrington, et al.: *Phys Rev B* **76**(2007) 140508.

[Cav87a] R. Cava, et al.: *Phys Rev B* **36**(1987) 5719.

[Cav87b] R. J. Cava, et al.: *Phys Rev Lett* **58**(1987) 408.

[Cav88] R. J. Cava, et al.: *Nature* **332**(1988) 814.

[Cav00] R. Cava: *J Am Ceram Soc* **83**(2000) 5.

[Cha01] S. Chakravarty, et al.: *Phys Rev B* **63**(2001) 094503.

[Cha07a] J. Chang, et al.: *Phys Rev Lett* **98**(2007) 077004.

[Cha07b] J. Chang, et al.: *cond-mat* **0712.2181**(2007).

[Cha08a] S. Chakravarty, et al.: *Proc Natl Acad Sci USA* **105**(2008) 8835.

[Cha08b] J. Chang, et al.: *Phys Rev B* **78**(2008) 104525.

[Cha08c] K. Chatterjee, et al.: *Nature Physics* **4**(2008) 108.

[Che02] H.-D. Chen, et al.: *Phys Rev Lett* **89**(2002) 137004.

[Che04] H.-D. Chen, et al.: *Phys Rev Lett* **93**(2004) 187002.

[Chi91] T. R. Chien, et al.: *Phys Rev Lett* **67**(1991) 2088.

[Chu93] C. W. Chu, et al.: *Nature* **365**(1993) 323.

[Dai98] P. Dai, et al.: *Phys Rev Lett* **80**(1998) 1738.

[Dai99] P. C. Dai, et al.: *Science* **284**(1999) 1344.

[Dai00] P. Dai, et al.: *Nature* **406**(2000) 965.

[Dam03] A. Damascelli, et al.: *Rev Mod Phys* **75**(2003) 473.

[Dem95] E. Demler, et al.: *Phys Rev Lett* **75**(1995) 4126.

[Dem01] E. Demler, et al.: *Phys Rev Lett* **87**(2001) 067202.

[dH98] B. C. den Hertog, et al.: *Phys Rev B* **58**(1998) 2838.

[Dim08] I. Dimov, et al.: *Phys Rev B* **78**(2008) 134529.

[Div04] U. Divakar, et al.: *Phys Rev Lett* **92**(2004) 237004.

[DL07] N. Doiron-Leyraud, et al.: *Nature* **447**(2007) 565.

[Erb96] A. Erb, et al.: *Phys C* **258**(1996) 9.

[Fis07] O. Fischer, et al.: *Rev Mod Phys* **79**(2007) 353.

[Fon95] H. F. Fong, et al.: *Phys Rev Lett* **75**(1995) 316.

[Fon96] H. Fong, et al.: *Phys Rev B* **54**(1996) 6708.

[Fon99a] H. Fong, et al.: *Phys Rev Lett* **82**(1999) 1939.

[Fon99b] H. Fong, et al.: *Phys Rev B* **61**(1999) 14773.

[Fon99c] H. F. Fong, et al.: *Nature* **398**(1999) 588.

[Fra97] M. Franz, et al.: *Phys Rev B* **56**(1997) 7882.

[Fuk96a] H. Fukuyama, et al.: *J Phys Soc Jpn* **65**(1996) 1182.

[Fuk96b] Y. Fukuzumi, et al.: *Phys Rev Lett* **76**(1996) 684.

[Fur98] A. Furrer: *Neutron scattering in layered copper oxide superconductors* (1998).

[Gou87] C. E. Gough, et al.: *Nature* **326**(1987) 855.

[Gup98] R. Gupta, et al.: *Phys C* **305**(1998) 179.

[Has96] M. Hase, et al.: *J Phys Soc Jpn* **65**(1996) 1392.

[Hay96] S. M. Hayden, et al.: *Phys Rev B* **54**(1996) R6905.

[Hay04] S. M. Hayden, et al.: *Nature* **429**(2004) 531.

[He01] H. He, et al.: *Phys Rev Lett* **86**(2001) 1610.

[He02] H. He, et al.: *Science* **295**(2002) 1045.

[He05] H. He, et al.: *cond-mat* **0002013**(2005).

[Hin08] V. Hinkov, et al.: *Science* **319**(2008) 597.

[Hir97] K. Hirota, et al.: *Physica B* **241-243**(1997) 817.

[Hir02] P. J. Hirschfeld, et al.: *J Low Temp Phys* **126**(2002) 881.

[Hof02] J. E. Hoffman, et al.: *Science* **295**(2002) 466.

[Hon91] D. Hong, et al.: *J Am Ceram Soc* **74**(1991) 1751.

[Hos08] M. A. Hossain, et al.: *Nature Physics* **4**(2008) 527.

[Hus02] N. E. Hussey: *Advances in Phys* **51**(2002) 1685.

[Ish93] K. Ishida, et al.: *J Phys Soc Jpn* **62**(1993) 2803.

[Ish98] K. Ishida, et al.: *Phys Rev B* **58**(1998) R5960.

[Jau08] C. Jaudet, et al.: *Phys Rev Lett* **100**(2008) 187005.

[Jay88] B. Jayaram, et al.: *Phys Rev B* **38**(1988) 2903.

[Jee88] C. Jee, et al.: *J Superc* **1**(1988) 63.

[Joh89] D. C. Johnston: *Phys Rev Lett* **62**(1989) 957.

[Jor89] J. Jorgensen, et al.: *Phys Rev B* **41**(1989) 1863.

[Jul00] M.-H. Julien, et al.: *Phys Rev Lett* **84**(2000) 3422.

[Kai89] D. Kaiser, et al.: *J Mater Res* **4**(1989) 745.

[Kak93] K. Kakurai, et al.: *Phys Rev B* **48**(1993) 3485.

[Kaw05] T. Kawamata, et al.: *Physica C* **426-431**(2005) 469.

[Kha02] B. Khaykovich, et al.: *Phys Rev B* **66**(2002) 014528.

[Kha05] B. Khaykovich, et al.: *Phys Rev B* **71**(2005) 220508.

[Kim03] H. Kimura, et al.: *Phys Rev Lett* **91**(2003) 067002.

[Kis89] K. Kishio, et al.: *J Solid State Chem* **82**(1989) 192.

[Kis01] J.-i. Kishine, et al.: *Phys Rev Lett* **86**(2001) 5365.

[Kiv98] S. A. Kivelson, et al.: *Nature* **393**(1998) 550.

[Kiv01] S. Kivelson: *Proc Natl Acad Sci USA* **98**(2001) 11903.

[Kiv02] S. A. Kivelson, et al.: *Phys Rev B* **66**(2002) 144516.

[Kiv03] S. A. Kivelson, et al.: *Rev Mod Phys* **75**(2003) 1201.

[Koi00a] Y. Koike, et al.: *Phys C* **341-348**(2000) 1751.

[Koi00b] Y. Koike, et al.: *Int J Mod Phys B* **14**(2000) 3520.

[Koi01] Y. Koike, et al.: *Phys C* **357**(2001) 82.

[Koi05] Y. Koike, et al.: *Physica C* **426-431**(2005) 189.

[Kom04] S. Komiya, et al.: *Phys Rev B* **70**(2004) 060503.

[Kon07] T. Kondo, et al.: *Phys Rev Lett* **98**(2007) 267004.

[Kro08] Y. Krockenberger, et al.: *Phys Rev B* **77**(2008) 060505.

[Kru97] C. Kruger, et al.: *J Solid State Chem* **134**(1997) 356.

[Kud04] K. Kudo, et al.: *Phys Rev B* **70**(2004) 014503.

[Lag93] J. R. Lagraff, et al.: *Phys Rev B* **47**(1993) 3380.

[Lak99] B. Lake, et al.: *Nature* **400**(1999) 43.

[Lak01] B. Lake, et al.: *Science* **291**(2001) 1759.

[Lak02] B. Lake, et al.: *Nature* **415**(2002) 299.

[Lak05] B. Lake, et al.: *Nat Mater* **4**(2005) 658.

[Lan94a] A. Lanckbeen, et al.: *Science* **29**(1994) 5441.

[Lan94b] A. Lanckbeen, et al.: *Phys C* **221**(1994) 53.

[Le93] L. P. Le, et al.: *Phys Rev B* **48**(1993) 7284.

[LeB07] D. LeBoeuf, et al.: *Nature* **450**(2007) 533.

[Lee06] P. A. Lee, et al.: *Rev Mod Phys* **78**(2006) 17.

[Lev05] G. Levy, et al.: *Phys Rev Lett* **95**(2005) 257005.

[Li06] J.-X. Li, et al.: *Phys Rev B* **74**(2006) 184515.

[Lia92] R. X. Liang, et al.: *Phys C* **195**(1992) 51.

[Lia98] R. Liang, et al.: *Phys C* **304**(1998) 105.

[Lia02] R. Liang, et al.: *Phys C* **383**(2002) 1.

[Lia06] R. Liang, et al.: *Phys Rev B* **73**(2006) 180505.

[Lib93] S. Libbrecht, et al.: *Phys C* **206**(1993) 51.

[Lin92] C. T. Lin, et al.: *Phys C* **193**(1992) 129.

[Liu95] D. Z. Liu, et al.: *Phys Rev Lett* **75**(1995) 4130.

[Lov86] S. W. Lovesey: *Theory of Neutron Scattering from Condensed Matter* (1986).

[LT06] M. Le Tacon, et al.: *Nature Physics* **2**(2006) 537.

[MA95] I. Maggio-Aprile, et al.: *Phys Rev Lett* **75**(1995) 2754.

[Mae89] H. Maeda, et al.: *Phys C* **157**(1989) 483.

[Mah94] A. V. Mahajan, et al.: *Phys Rev Lett* **72**(1994) 3100.

[Mak03] M. Maki, et al.: *Phys Rev B* **67**(2003) 014534.

[Map98] M. B. Maple: *J Magn magnetic Mat* **177**(1998) 18.

[Mas01] T. Masui, et al.: *Physica C* **357-360**(2001) 39.

[Mat88] L. F. Mattheiss, et al.: *Phys Rev B* **37**(1988) 3745.

[Mat93] M. Matsuda, et al.: *J Phys Soc Jpn* **62**(1993) 443.

[Mei91] C. Meingast, et al.: *Phys Rev Lett* **67**(1991) 1634.

[Men94] P. Mendels, et al.: *Phys Rev B* **49**(1994) 10035.

[Men99] P. Mendels, et al.: *Europhys Lett* **46**(1999) 678.

[Mes00] J. Mesot, et al.: *Phys C* **341**(2000) 2105.

[Mil96] A. J. Millis, et al.: *Phys Rev B* **54**(1996) 16172.

[Mil02] R. I. Miller, et al.: *Phys Rev Lett* **88**(2002) 137002.

[Mil07] A. J. Millis, et al.: *Phys Rev B* **76**(2007) 220503.

[Mit01] V. F. Mitrovic, et al.: *Nature* **413**(2001) 501.

[Moo93] H. A. Mook, et al.: *Phys Rev Lett* **70**(1993) 3490.

[Moo98] H. A. Mook, et al.: *Nature* **395**(1998) 580.

[Moo02] H. A. Mook, et al.: *Phys Rev Lett* **88**(2002) 097004.

[Mor98] D. K. Morr, et al.: *cond-mat* **9805107**(1998).

[Nac96] B. Nachumi, et al.: *Phys Rev Lett* **77**(1996) 5421.

[Nie98] C. Niedermayer, et al.: *Phys Rev Lett* **80**(1998) 3843.

[Nun93] M. Nunezregueiro, et al.: *Science* **262**(1993) 97.

[Obe92] S. Obertelli, et al.: *Phys Rev B* **46**(1992) 14928.

[Oda97] S. Odashima, et al.: *Phys Rev B* **56**(1997) 126.

[Onu94] F. Onufrieva, et al.: *Physica C* **235-240**(1994) 1687.

[Onu95a] F. Onufrieva: *Physica C* **251**(1995) 348.

[Onu95b] F. Onufrieva, et al.: *Phys Rev B* **52**(1995) 7572.

[Oua04] S. Ouazi, et al.: *Phys B* **70**(2004) 104515/1.

[Oua06] S. Ouazi, et al.: *Phys Rev Lett* **96**(2006) 127005.

[Pai06] S. Pailhes, et al.: *Phys Rev Lett* **96**(2006) 257001.

[Pan00a] S. H. Pan, et al.: *Nature* **403**(2000) 746.

[Pan00b] S. H. Pan, et al.: *Phys Rev Lett* **85**(2000) 1536.

[Par03] K. Park: *Phys Rev B* **67**(2003) 094513.

[Pig07] B. Pignon, et al.: *Phys C* **460**(2007) 378.

[Pim05] A. V. Pimenov, et al.: *Phys Rev Lett* **94**(2005) 227003.

[Pod03] D. Podolsky, et al.: *Phys Rev B* **67**(2003) 094514.

[Pod08] D. Podolsky, et al.: *cond-mat* **0806.0005**(2008).

[Poi94a] D. Poilblanc, et al.: *Phys Rev B* **50**(1994) 13020.

[Poi94b] D. Poilblanc, et al.: *Phys Rev Lett* **72**(1994) 884.

[Pre91] M. Presland, et al.: *Phys C* **176**(1991) 95.

[Put93] S. N. Putilin, et al.: *Nature* **362**(1993) 226.

[Pyk93] N. Pyka, et al.: *Phys Rev B* **48**(1993) 7746.

[RA08] F. Rullier-Albenque, et al.: *Europhys Lett* **81**(2008) 37008.

[Rao88] C. V. N. Rao, et al.: *Phys C* **152**(1988) 479.

[Reg94] L. P. Regnault, et al.: *Phys C* **235**(1994) 59.

[Reg95] L. P. Regnault, et al.: *Europhys Lett* **32**(1995) 579.

[Ren98] C. Renner, et al.: *Phys Rev Lett* **80**(1998) 3606.

[Ric91] J. P. Rice, et al.: *J Cryst Growth* **109**(1991) 432.

[Rie96] J. Riera, et al.: *Phys Rev B* **54**(1996) 7441.

[Ris08] Risdiana, et al.: *Phys Rev B* **77**(2008) 054516.

[RM91] J. Rossat-Mignod, et al.: *Phys C* **185-189**(1991) 86.

[Ros91] M. J. Rosseinsky, et al.: *Phys Rev Lett* **66**(1991) 2830.

[Sav02] A. T. Savici, et al.: *Phys Rev B* **66**(2002) 014524.

[Sav05] A. T. Savici, et al.: *Phys Rev Lett* **95**(2005) 157001.

[Sca95] D. J. Scalapino: *Phys Rep* **250**(1995) 330.

[Sch89] H. Schmid, et al.: *Phys C* **157**(1989) 555.

[Sch93] A. Schilling, et al.: *Nature* **363**(1993) 56.

[Sen94] P. Sen, et al.: *Phys Rev B* **50**(1994) 10381.

[Sen96] P. Sen, et al.: *Phys Rev B* **53**(1996) 328.

[Seo07] K. Seo, et al.: *Phys Rev B* **76**(2007) 020511.

[Shi92] H. Shimizu, et al.: *Phys C* **196**(1992) 329.

[Shi03] K. Shibata, et al.: *Physica C* **388-389**(2003) 277.

[Sid96] Y. Sidis, et al.: *Phys Rev B* **53**(1996) 6811.

[Sid00] Y. Sidis, et al.: *Phys Rev Lett* **84**(2000) 5900.

[Sis00] D. L. Sisson, et al.: *Phys Rev B* **61**(2000) 3604.

[Smi01] C. Smith: *Physics in local lattice distortions* **554**(2001) 209.

[Spe88] E. Specht, et al.: *Phys Rev B* **37**(1988) 7426.

[Squ97] G. L. Squires: *Introduction to the Theory of Thermal Neutron Scattering* (1997).

[Sto06] C. Stock, et al.: *Phys Rev B* **73**(2006) 100504.

[Tak87] E. Takayama-Muromachi, et al.: *Jpn J Appl Phys* **26**(1987) L1156.

[Tak88] T. Takabatake, et al.: *Solid State Comm* **66**(1988) 413.

[Tal95a] J. L. Tallon, et al.: *Phys Rev B* **51**(1995) 12911.

[Tal95b] J. L. Tallon, et al.: *Phys Rev Lett* **75**(1995) 4114.

[Tal97] J. L. Tallon, et al.: *Phys C* **282-287**(1997) 236.

[Tan06] K. Tanaka, et al.: *Science* **314**(2006) 1910.

[Tes04] Z. Tesanovich: *Phys Rev Lett* **93**(2004) 217004.

[Tra95] J. M. Tranquada, et al.: *Nature* **375**(1995) 561.

[Tra04a] J. M. Tranquada, et al.: *Phys Rev B* **69**(2004) 174507.

[Tra04b] J. M. Tranquada, et al.: *Nature* **429**(2004) 534.

[Tra05] J. M. Tranquada: *cond-mat* **0512115**(2005).

[Tsu00] C. C. Tsuei, et al.: *Rev Mod Phys* **72**(2000) 969.

[Uim92] G. Uimin, et al.: *Physica C* **199**(1992) 251.

[Vig07] B. Vignolle, et al.: *Nature Physics* **3**(2007) 163.

[Vil96] C. Villard, et al.: *Phys Rev Lett* **77**(1996) 3913.

[Voj99] M. Vojta, et al.: *Phys Rev Lett* **83**(1999) 3916.

[Vor93] V. Voronkova, et al.: *Phys C* **218**(1993) 175.

[VT90] G. Van Tendeloo, et al.: *Phys C* **167**(1990) 627.

[Wak05] S. Wakimoto, et al.: *Phys Rev B* **72**(2005) 064521.

[Wal93] R. E. Walstedt, et al.: *Phys Rev B* **48**(1993) 10646.

[Wan01] Q.-H. Wang, et al.: *Phys Rev Lett* **87**(2001) 167004.

[Wat99] I. Watanabe, et al.: *Phys Rev B* **60**(1999) R9955.

[Wat00] I. Watanabe, et al.: *Phys Rev B* **62**(2000) 14524.

[Wei91] P. Wei, et al.: *Physica C* **183**(1991) 32.

[Wel89] U. Welp, et al.: *Physica C* **161**(1989) 1.

[Wen96] X.-G. Wen, et al.: *Phys Rev Lett* **76**(1996) 503.

[Wes89] K. Westerholt, et al.: *Phys Rev B* **39**(1989) 11680.

[WU87] M. K. WU, et al.: *Phys Rev Lett* **58**(1987) 908.

[Xia88a] G. Xiao, et al.: *Phys Rev Lett* **60**(1988) 1446.

[Xia88b] G. Xiao, et al.: *Nature* **332**(1988) 238.

[Yam95] K. Yamada, et al.: *Phys Rev Lett* **75**(1995) 1626.

[Yin97] L. Yin, et al.: *Phys Rev Lett* **78**(1997) 3559.

[Zaa88] J. Zaanen, et al.: *Phys Rev Lett* **60**(1988) 2685.

[Zaa89] J. Zaanen, et al.: *Phys Rev B* **40**(1989) 7391.

[Zab06] V. B. Zabolotnyy, et al.: **0608295**(2006).

[Zab07] V. B. Zabolotnyy, et al.: *Phys Rev B* **76**(2007) 064519.

[Zag95] S. Zagoulaev, et al.: *Phys Rev B* **52**(1995) 10474.

[Zag96] S. Zagoulaev, et al.: *Physica C* **259**(1996) 271.

[Zen95] D. C. Zeng, et al.: *J Alloys Comp* **228**(1995) 79.

[Zha94] R. P. Zhao, et al.: *Physica C* **230**(1994) 75.

[Zha96] Y. Zha, et al.: *Phys Rev B* **54**(1996) 7561.

[Zha97] S. C. Zhang: *Science* **275**(1997) 1089.

[Zhu95] J. P. Zhuo, et al.: *Appl Phys Lett* **66**(1995) 2900.

[Zhu01] J.-X. Zhu, et al.: *Phys Rev Lett* **87**(2001) 147002.

[Zie96] W. Ziegler, et al.: *Phys Rev B* **53**(1996) 8704.

Acknowledgments

The realization of this work would not have been possible without the support by numerous people.

First of all, I wish to thank my supervisor Prof. Bernhand Keimer for advice on the thesis topic, organization of contact people to keep the progress of the work going and guidance of the work to ensure scientifically interesting analysis of the results. His extraordinarily comprehensive knowledge of condensed matter physics and structured approach to science served as an exemplar to me.

I'm also exceptionally grateful to have had the pleasure to work with Yvan Sidis, whose extensive experimental experience, numerous fascinating ideas, selfless help during many experiments and motivational support I appreciate a lot. Other irreplaceable assistance during experiments came from Philippe Bourges, Niels Christensen, Klaudia Hradil and Alexandre Ivanov.

I also benefitted from the experience of Vladimir Hinkov who introduced me to the necessary experimental skills, supported me with topical advice and help in organizing experiments. Moreover, my colleagues Daniel Haug and Markus Raichle were always helpful during experiments or when samples had to be transferred.

Or course the whole work would not have been possible without the preparation of the sample material. Therefore I wish to thank Chengtian Lin, Sabine Lacher and Julia Tchakhalin for crystal growth and Barbara Baum who spent endless hours cutting and polishing the crystals. Technical support I received from Horst Bender, Manfred Ohl and Christof Busch.

I also thank Claudia Hagemann, Mrs. Schleehauf, Mrs. Süss and Mrs. Sigloch for their continuous support in several administrative procedures. And finally, I wish to thank my colleagues Britta Bohnenbuck, Ioannis Zegkinoglou, Ji Tae Park, Martin Rahlenbeck, Yulia Matiks, Timur Mukhamedzyanov, Philippe Leiniger, Petar Yordanov who ensured a pleasant work day with occasional discussions and mental support.